

Modeling and Experimental Validation of Latent Heat Thermal Energy Storage System

A Dissertation

Presented in Partial Fulfillment of the Requirements for the

Degree of Doctor of Philosophy

with a

Major in Nuclear Engineering

in the

College of Graduate Studies

University of Idaho

by

Amey Shigrekar

Major Professor: Richard Christensen, Ph.D.

Committee Members: Michael McKellar, Ph.D.; Richard Boardman, Ph.D.;

Tao Xing, Ph.D.; David Arcilesi, Ph.D.

Department Administrator: Richard Christensen, Ph. D.

December 2020

## Authorization to Submit Thesis

This dissertation of Amey Shigrekar, submitted for the degree of Doctor of Philosophy with a Major in Nuclear Engineering and titled "Modeling and Experimental Validation of Latent Heat Thermal Energy Storage System," has been reviewed in final form.

Permission, as indicated by the signatures and dates below, is now granted to submit final copies to the College of Graduate Studies for approval.

Major Professor: \_\_\_\_\_ Date \_\_\_\_\_  
Richard Christensen, Ph.D.

Committee  
Members: \_\_\_\_\_ Date \_\_\_\_\_  
Michael McKellar, Ph.D.

\_\_\_\_\_ Date \_\_\_\_\_  
Richard Boardman, Ph.D.

\_\_\_\_\_ Date \_\_\_\_\_  
Tao Xing, Ph.D.

\_\_\_\_\_ Date \_\_\_\_\_  
David Arcilesi, Ph.D.

Department  
Administrator: \_\_\_\_\_ Date \_\_\_\_\_  
Richard Christensen, Ph.D.

## Abstract

In an effort to address the detrimental effects of climate change, a paradigm shift has taken place over the last couple of decades to switch from fossil fuel-based energy sources to clean energy. This change, along with the ever growing need for energy has facilitated the increasing penetration of renewable energy sources such as wind, solar, and hydropower. Although renewable energy can indisputably minimize the threat of global warming, their dependency on weather conditions and diurnal variations leads to inconsistencies in energy supply. To overcome this intermittency, these clean energy sources are quite often backed-up by fossil-fuel generators, thus defeating the purpose of clean energy establishment.

In order for renewable energy sources to become completely reliable as a primary source of energy, it should be stored during hours of excess production and be ready to use during periods of excess demand. This can be achieved by incorporating energy storage systems. Currently, thermal energy storage (TES) is the only technology to be deployed on a gigawatt scale, and specifically the sensible heat TES. This technology is expensive and in some cases, intrinsically consumes energy to prevent the storage medium from freezing. In comparison, latent heat storage designs could theoretically offer higher gravimetric storage capacities, resulting in smaller storage sizes. However, low thermal conductivities of phase change materials hinders the realization of this technology's potential, thereby preventing large scale deployment. To overcome this issue, several modifications to the TES designs have been undertaken. Regardless, the models developed so far are high-fidelity and high-complexity, design specific, and therefore computationally expensive. To evaluate the benefits of coupling latent heat TES systems, integrated systems-level analyses need to be carried out. This requires simpler, yet, accurate models.

In this dissertation, simplified, transient, validated models are developed for a latent heat thermal energy storage system. The modeling effort includes the analysis of three models, comparison of these models to a commercial CFD tool, and verification and validation using results acquired by performing experiments on a bench-scale latent heat thermal battery. To enhance heat transfer and overcome the underlying deficiency of PCMs, finned tube design is used. Preliminary analysis is conducted by assuming pure conduction within the phase change material, however, this is modified to accommodate for natural convection, by deriving an apparent thermal conductivity for the liquid phase. This apparent thermal conductivity is based on a correlation that includes the Rayleigh number, along with coefficients that are acquired empirically by trial and error method. The coefficients  $C$  and  $n$  for the geometry considered in this study are 0.228 and 0.25, respectively. To account for the presence of fins, a novel approach based on the thermal resistance network is applied to derive an effective thermal conductivity. The combination of this effective thermal conductivity and the apparent thermal conductivity, is applied to the liquid domain to model phase change in a finned tube system, that experiences a combined, natural convection- and conduction-based heat transfer.

## Acknowledgements

I must first thank sincerely my parents, my sister and Priyanka, for their unwavering support and affection throughout the years. This would not have been possible without you. Next, I wish to express my deepest gratitude to my advisor Dr. Richard Christensen for his expert guidance, valuable insight and constant help during the course of this study. His patience, motivation and immense knowledge, has helped me in all the time of research and writing of this dissertation.

I would also like to thank my committee members, Dr. Michael McKellar, Dr. Tao Xing, Dr. David Arcilesi, and Dr. Richard Boardman for their passionate participation, invaluable comments, and constructive criticism which have improved my technical skills and understanding of the subject matter, as well as helped shape this dissertation.

## Table of Contents

<b>Authorization to Submit Dissertation .....</b>	<b>ii</b>
<b>Abstract.....</b>	<b>iii</b>
<b>Acknowledgements .....</b>	<b>v</b>
<b>Table of Contents .....</b>	<b>vi</b>
<b>List of Tables .....</b>	<b>x</b>
<b>List of Figures .....</b>	<b>xi</b>
<b>1 Introduction .....</b>	<b>1</b>
1.1 Background .....	1
1.2 Motivation and Goals.....	6
1.3 Approach.....	7
<b>2 Thermal Energy Storage - Technology Overview.....</b>	<b>10</b>
2.1 Introduction .....	10
2.2 Literature Review .....	12
2.2.1 Thermal Energy Storage Media.....	12
2.2.2 Current Applications of TES Systems.....	13
2.2.3 Potential Applications of TES Research.....	18
2.3 Technology Selection: Latent Heat Thermal Energy Storage or Sensible Heat Thermal Energy Storage .....	19
2.4 Phase Change Material (PCM) Selection.....	21
<b>3 Thermal Energy Storage - Design .....</b>	<b>25</b>

3.1	Introduction .....	25
3.2	Design Review.....	27
3.3	Design Methodology.....	28
3.4	Component Design.....	29
3.4.1	Geometrical Analysis.....	34
3.4.2	Effective Thermal Conductivity .....	34
3.4.2.1	Design Simplification . . . . .	40
3.5	Mathematical Modeling .....	41
3.5.1	Analytical Modeling .....	44
3.5.1.1	Model Equations . . . . .	44
3.5.2	Numerical Modeling .....	47
3.5.2.1	Governing Equations . . . . .	47
3.5.2.2	Finite Volume Method Discretization . . . . .	52
3.5.2.3	Numerical Solvers and Convergence Conditions . . . . .	56
3.5.2.4	Numerical Model 1 – MATLAB . . . . .	58
3.5.2.5	Numerical Model 2 – Dymola . . . . .	59
<b>4</b>	<b>Computational Fluid Dynamics (CFD).....</b>	<b>61</b>
4.1	Introduction .....	61
4.2	CFD Simulation Setup.....	63
4.2.1	Two-Dimensional (2D) Geometry and Grid Definition.....	63
4.2.2	Physics and Boundary Conditions.....	64
4.3	Preliminary Modeling Results - Pure Conduction .....	68
4.4	Case Studies.....	68
4.4.1	Case Study 1: Varying PCM Thickness .....	71
4.4.2	Case Study 2: Varying PCM Thermal Conductivity.....	72
4.4.3	Case Study 3: Varying PCM Latent Heat of Fusion .....	73

4.4.4	Case Study 4: Varying Initial Temperature of PCM.....	73
<b>5</b>	<b>Design and Analysis of Experimental Facility .....</b>	<b>76</b>
5.1	Experimental Apparatus.....	76
5.1.1	Thermal Battery Test Section .....	77
5.1.2	Temperature sensors.....	80
5.1.3	Heat Transfer Fluid Loop.....	83
5.1.3.1	Header-Baffle Design . . . . .	84
5.1.4	Data Acquisition.....	87
5.2	Experimental Procedure.....	88
5.2.1	Preparing Test Section .....	88
5.2.2	Preparing HTF Loop.....	89
5.2.3	Charging the LH-TES .....	90
5.2.4	Discharging the LH-TES .....	90
<b>6</b>	<b>Experimental Results, Discussion, and Comparison.....</b>	<b>93</b>
6.1	Thermal Hydraulic Performance of Finned Design .....	93
6.1.1	Data Analysis for Finned Test Section .....	96
6.2	Analysis to Quantify Effects of Natural Convection .....	96
6.3	Verification.....	105
6.3.1	Solution Verification .....	105
6.3.1.1	Generalized Richardson Extrapolation (GRE) . . . . .	106
6.4	Model Validation.....	110
6.5	Preliminary Analysis - Unfinned Test Section .....	117
<b>7</b>	<b>Conclusions and Future Work .....</b>	<b>121</b>
7.1	Conclusions .....	121
7.2	Future Work.....	123

References ..... 124

## List of Tables

1.1	Comparison of energy storage technologies . . . . .	5
2.1	Commonly used energy storage media . . . . .	13
2.2	Thermophysical properties of n-Paraffin, n-Eicosane, and RT27 . . . . .	24
2.3	Thermophysical properties of HTF and SS316 . . . . .	24
3.1	Unit cell dimensions . . . . .	36
3.2	Dimensions of hexagonal and simplified cylindrical unit cells . . . . .	40
3.3	Numerical model boundary conditions . . . . .	52
4.1	Grid resolutions and aspect ratios of domains in the base model . . . . .	64
4.2	Thermophysical properties of materials used in preliminary analysis . . . . .	65
4.3	Boundary conditions for base model used in case studies . . . . .	66
4.4	Point-probe locations in 2D PCM domain . . . . .	67
6.1	Rayleigh correlation coefficient analysis fro apparent thermal conductivity .	100
6.2	Maximum absolute errors between modeling and experimental data for base case . . . . .	102
6.3	Maximum absolute errors between modeling and experimental data for vali- dation test cases . . . . .	102
6.4	Grid and time-step refinement used for grid sensitivity analysis . . . . .	107
6.5	Maximum absolute errors in CFD models for base case validation . . . . .	115
6.6	Maximum absolute errors in numerical models for base case validation . . .	115
7.1	Simulation runtime for models at different mesh refinements (time in seconds)	123

## List of Figures

1.1	Duck Curve displaying projected net load of dispatchable power in California	2
1.2	Classification of energy storage systems . . . . .	4
2.1	Classification of thermal energy storage (TES) systems . . . . .	10
2.2	Two-tank Sensible-Heat Thermal Energy Storage (SH-TES) system coupled to parabolic trough Concentrated Solar Power (CSP) plant . . . . .	15
2.3	Solar seasonal storage and district loop at Drake Landing Solar Community	16
2.4	Schematic of Liquid Air Energy Storage (LAES) technology [23] . . . . .	17
2.5	Schematic of solar power combined steam accumulator technology for direct steam generation . . . . .	18
2.6	Schematic of a potential Nuclear-Renewable Hybrid Energy System . . . . .	20
3.1	Flowchart of a proposed design methodology for LH-TES system development	30
3.2	Schematic of the working principle for a generic LH-TES system . . . . .	31
3.3	Potential quadrilateral tube arrangement in an LH-TES . . . . .	32
3.4	Potential hexagonal tube arrangement in an LH-TES . . . . .	33
3.5	Potential hexagonal tube arrangement in an LH-TES with a modified cell boundary . . . . .	33
3.6	Heat transfer path and thermal resistance in finned tube . . . . .	35
3.7	Simplified thermal resistance network in a finned tube . . . . .	37
3.8	Effective resistance network for a finned tube . . . . .	38
3.9	Geometric simplification for modeling - finned hexagon to simplified cylinder	39
3.10	Unit cell from a shell-and-tube arrangement for mathematical modeling . . .	41
3.11	Simplification of geometry from 3D to 2D-axisymmetric . . . . .	42
3.12	Temperature and enthalpy-based plot for isothermal phase transition . . . .	50
3.13	Computational domain with differential equations and boundary conditions .	52
3.14	Comparison of FVM- and FDM-based grid discretization . . . . .	53

3.15	Schematic of interface between two cells of dissimilar material properties . . .	55
4.1	Dimensions of 2D problem domain . . . . .	63
4.2	Continua used for physics model selection in 2D simulations . . . . .	65
4.3	Boundaries of 2D problem domain . . . . .	66
4.4	Point probes in 2D PCM domain for temperature data acquisition in CFD simulations . . . . .	67
4.5	Liquid fraction profiles during melting and solidification . . . . .	69
4.6	Temperature profile comparison of 2D numerical and CFD models based on pure conduction . . . . .	70
4.7	Effect of varying PCM's thickness on melt time . . . . .	72
4.8	Effect of varying PCM's thermal conductivity on melt time . . . . .	73
4.9	Effect of varying PCM's latent heat of fusion on melt time . . . . .	74
4.10	Effect of varying PCM's initial temperature on melt time . . . . .	75
5.1	Schematic of the experimental apparatus . . . . .	76
5.2	CAD representation exploded view of test section, with the base plate and bottom end cap . . . . .	77
5.3	Top view of finned and unfinned thermal batteries . . . . .	78
5.4	Top view of end cap and O-ring . . . . .	79
5.5	Top view of base-plate . . . . .	80
5.6	Swagelok fittings for wall-based thermocouples . . . . .	81
5.7	Swagelok fittings for internal thermocouples . . . . .	81
5.8	CAD view of thermocouple locations in the test section . . . . .	82
5.9	Thermocouple locations in the unfinned test section . . . . .	82
5.10	Tempco temperature controller used for maintaining hot water bath temperature	83
5.11	Variable area flowmeter for water . . . . .	84
5.12	Header components - top connector, baffle, and bottom connector . . . . .	85

5.13	Evolution of baffle design to diffuse HTF flow . . . . .	86
5.14	Ring gaskets used to create a tight seal around the test section tubes . . . . .	87
5.15	Ring gasket arrangement in the bottom connector of the header . . . . .	87
5.16	National Instruments Data Acquisition equipment . . . . .	88
5.17	Top-view of test sections filled with PCM . . . . .	91
5.18	Experimental setup with insulated test section . . . . .	92
6.1	Experimental temperature data for for finned tube test section . . . . .	94
6.2	CFD and experimental temperature profile comparison for wall probes . . . . .	97
6.3	Numerical, CFD and experimental temperature profile comparison - finned test section . . . . .	98
6.4	Temperature profiles for various coefficients in Rayleigh correlation . . . . .	100
6.5	CFD and experimental temperature profile comparison with enhanced thermal conductivity for base case . . . . .	101
6.6	CFD and experimental temperature profile comparison with enhanced thermal conductivity with HTF at 50°C . . . . .	103
6.7	CFD and experimental temperature profile comparison with enhanced thermal conductivity with HTF at 70°C . . . . .	104
6.8	Representation of structured and unstructured mesh . . . . .	106
6.9	Experimental and CFD temperature profiles for various grids, with pure and enhanced thermal conductivities . . . . .	112
6.10	Error and uncertainty bands for base case pure conduction models in CFD . . . . .	113
6.11	Error and uncertainty bands for base case enhanced conductivity models in CFD . . . . .	114
6.12	Experimental and MATLAB temperature profiles for various grids, with pure and enhanced thermal conductivities . . . . .	116
6.13	Error and uncertainty bands for base case pure conduction models in MATLAB	117

6.14 Error and uncertainty bands for base case enhanced conductivity models in MATLAB . . . . .	118
6.15 Numerical, CFD and experimental temperature profile comparison - unfinned test section . . . . .	119
6.16 Temperature profile comparison for finned and unfinned test sections . . . .	120

# CHAPTER 1

## Introduction

### 1.1 Background

Climate change in its broadest sense, refers to an alteration in the pattern of weather conditions over a long period of time, caused due to a combination of natural and human induced activities. Since 1970, CO<sub>2</sub> emissions have increased by about 90%, with emissions from fossil fuel combustion and industrial processes contributing to about 78% of the total greenhouse gas (GHG) emissions [1]. This extensive release of GHGs has caused the planet's average surface temperature to rise by about 1°C since the late 19<sup>th</sup> century[2]. Further increase in the earth's temperature will cause detrimental changes in precipitation patterns, lead to more droughts and heat waves, and cause the sea levels to rise by 1 - 4 feet worldwide [3]. If these trends continue, the potential implications are so devastating that the Intergovernmental Panel on Climate Change has stated that “unmitigated climate change would, in the long term, be likely to exceed the capacity of natural, managed, and human systems to adapt” [4].

Such concerns about climate change have caused a shift from fossil fuel-based energy sources to low-carbon emitting energy sources. A recent large-scale implementation of solar and wind farms has rejuvenated the interest in renewable energy, driving down the costs of low carbon electricity, and utilizing domestically sourced alternatives to imported fossil fuels [5]. Even when including life cycle emissions of clean energy i.e. the emissions from each stage of a technology's life - manufacturing, installation, operation, decommissioning - the global warming emissions associated with renewable energy are minimal when compared to fossil fuels [6]. In addition, renewable energy sources generate electricity with no associated air pollutants, and therefore do not cause negative health impacts.

However, with the rapid integration of renewable energy into the electrical grid, new technical challenges have also surfaced. Renewable energy sources, such as solar and wind, are highly dependent on weather conditions, and cannot be relied upon for based load requirements. The intermittent nature of renewable energy leads to instabilities in the grid, and price fluctuations in the electricity market. These fluctuations in power outputs can occur on a daily, monthly or even annual basis. One of the illustration is provided by the famous Duck Curve, shown in Fig.1.1, which describes a projected net load of dispatchable power required as a function of annually increasing solar photovoltaic (PV) electricity generation available to the California Independent System Operator [7, 8].

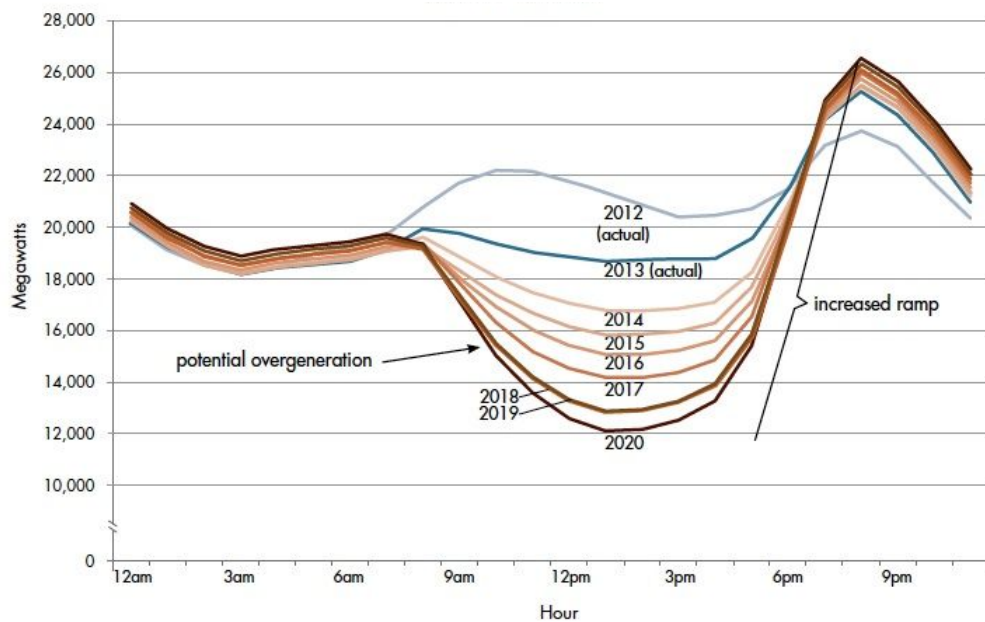


Figure 1.1: Duck Curve displaying projected net load of dispatchable power in California

As PV generation increases, the risk of periodic over-generation during times of abundant solar energy input also increases, leading to curtailment of energy from other sources. Then, during hours of sunset, generation capacity has to be rapidly ramped up to meet the energy demands of early nighttime. Such a demand is currently met by hydroelectric power plants and gas-turbine power plants within each state where available, as well as by importing power from the neighboring states. Although hydroelectric power

is low-cost and dispatchable, it is geographically limited, whereas gas-turbine power plants produce undesirable emissions.

It is evident that renewable energy sources that harness the power of nature have several limiting factors. When compared to renewables or fossil fuels, nuclear power plants (NPPs) are a much stable source of baseload energy. In the United States, nuclear energy is the largest source of clean power, generating more than 55% of the nation's emissions-free electricity. In 2018, NPPs operated at full power, more than 93% of the time, making it the most reliable energy source on the grid. However, low-cost natural gas and subsidized renewable energy sources have created challenging market conditions for the nuclear industry. Strict regulations on maintenance, staffing levels, operator training, and plant inspections have become a financial burden for this industry. Although advancements in nuclear technology have led to reactor designs that are capable of load following, to meet the market demands, from the economic standpoint, it is preferable for NPPs to operate at baseload.

In order to make the most out of renewable energy sources, while allowing NPPs to perform at baseload capacity, it is necessary to store energy when produced in excess using energy storage systems, and then release it to meet peak market demands. By integrating NPPs and renewable energy sources, with energy storage systems, it is possible to respond effectively to the grid dynamics and leverage emissions-free energy, independent of the weather conditions or the geographical location of the site, in a reliable and effective manner. Currently, the need for energy storage is widely accepted, but the best implementation method is still undecided. Energy storage technologies vary based on the mechanism in which the energy is stored. Examples of a few energy storage systems currently in use are shown in Fig. 1.2.

Each of the technologies displayed in Fig. 1.2 have their pros and cons based on their storage capacity, charge and discharge rates, round-trip efficiency, life cycle, and

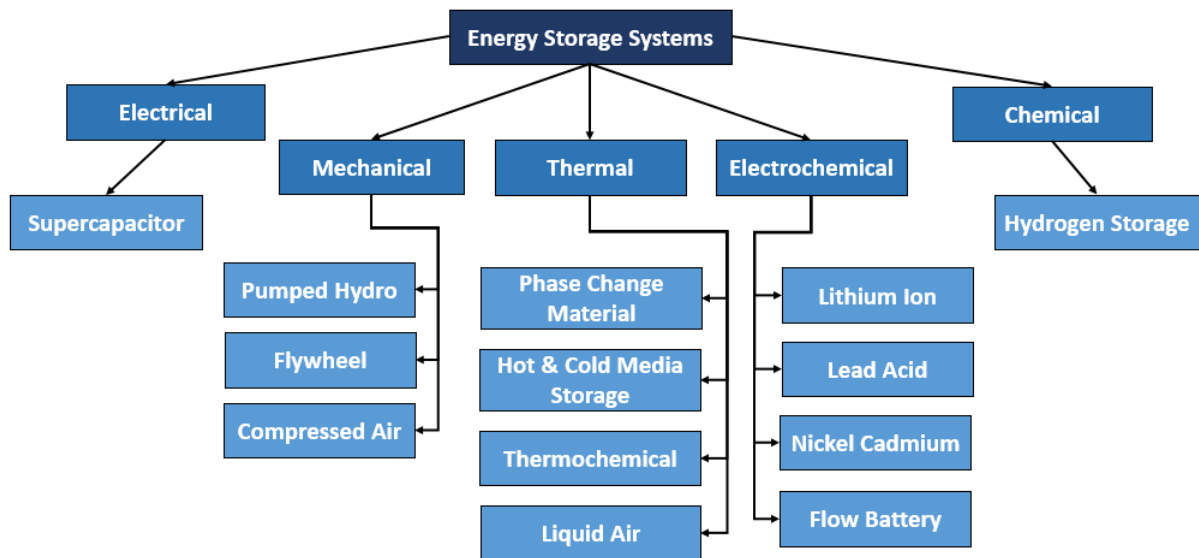


Figure 1.2: Classification of energy storage systems

their respective restrictions due to environmental factors or physical limitations. In order to compare these different types of energy storage technologies to each other, a few key parameters such as technology readiness level (TRL), round trip efficiency, and the levelized cost of electricity (LCOE) can be used. The TRL is a type of measurement system used to assess the maturity level of the technology, the rating ranging from 1 - 9, with 9 being the most mature. The round trip efficiency is the ratio of energy retrieved from a storage to the initial energy input. The higher the efficiency, the lower are the losses during storage. And, the LCOE represents the average revenue per unit of electricity generated that would be required to recover the costs of building and operating a generating plant during an assumed financial life and operating cycle [9]. As the success of most technologies is driven by economics, the LCOE for energy storage systems should be low if they are to be deployed on a large scale. Table 1.1 presents metrics used to compare few of the prominent energy storage technologies.

Out of all the energy storage technologies, thermal energy storage (TES) stands out for the following reasons:

Table 1.1: Comparison of energy storage technologies [10, 11, 12, 13, 14]

Metric	Thermal			Electrical	Mechanical		
	Solid particles	Molten salt	PCM	Batteries	Hydro	CAES	Flywheels
Levelized cost (\$/MWe)	10 - 13	11 - 17	95 - 150	100 - 1000	150 - 220	120 - 210	350 - 400
Round trip efficiency (%)	> 98%	> 98%	75 - 90%	60 - 90%	65 - 80%	40 - 70%	80 - 90%
Life cycles	> 10,000	> 10,000	~1000 - 5000	~1000 - 5000	> 10,000	> 10,000	> 10,000
Environmental Impact	N/A	Corrosion	Corrosion	Heavy metals	N/A	N/A	N/A
Limitations	Particle-fluid heat transfer	Salt decomposition at high temperatures	Low thermal conductivity related heat transfer	Expensive for large scale storage	Geographical limitations	Geographical limitations/Expensive	Low storage capacity
Technology Readiness Level (TRL)	4 - 6	9	5	7 - 9	9	6	7

- Thermal energy is abundantly available in nature at low-to-no cost from the sun and geothermal sources.
- Excess thermal energy is generated by almost all of the industrial processes, which is lost to the environment as waste heat. This energy can be absorbed, stored and recuperated later, without a negative impact on the efficiency of its source.
- Due to the myriad of materials that could be used as storage mediums, thermal storage devices can be coupled to a vast number of applications, operating over a large temperature range.
- From Table 1.1, it is evident that thermal storages have a relatively high TRL, a low LCOE, a high round trip efficiency, and high life cycles, with minimal environmental hazards that could be overcome without significant adverse impacts.

Currently, the only TES technology deployed over a gigawatt scale is that of a sensible heat thermal energy storage (SH-TES) system. This technology stores heat in a storage

medium by taking advantage of its specific heat capacity and increasing its temperature during the charging cycle. During hours of energy demand, thermal energy is recovered from the storage medium, thereby decreasing its temperature. The storage capacity of an SH-TES is determined by the storage medium's specific heat capacity, its mass, as well as the operational temperature gradient between the heat source and the storage medium itself. Due to the simplicity of their design, ease of operation, and the potential increment in efficiency that they would bring about, a significant number of concentrated solar power (CSPs) stations have integrated SH-TES systems with the power blocks. When excess heat is produced by the solar collectors, which cannot be used by the power blocks that convert heat into electricity, this energy is diverted to the storage systems to be used after sundown.

As opposed to relying on the material's specific heat capacity, latent heat thermal energy storage (LH-TES) systems can utilize the heat of fusion of a medium, and store heat via phase change. This, in theory, would provide larger heat gravimetric densities while reducing the storage volumes. The phase change material (PCM) can be selected based on its melting point, appropriately matched to the temperature of the heat source. In operation, phase change is ideally an isothermal process, thereby allowing the LH-TES to act as a constant temperature heat source with little material degradation over time [15]. This is an attractive feature as it could potentially reduce material, operation and maintenance costs.

## 1.2 Motivation and Goals

Despite there being a significant amount of research in design of various TES systems, there is a lack of unified approaches for the testing and analysis used in the improvement of latent heat TES (LH-TES) systems. Currently, very few studies have been conducted to analyze the dynamic performance of LH-TES systems. Although many mathematical

models exist for predicting melting and solidification rates in phase change materials (PCMs), they are not widely used in industry as those models have been developed for specific geometries and are high-fidelity. The complexity of such component-level models tends to bog down the simulation runtime of coupled, systems-level models and therefore limit the possibility of a fair comparison with other TES systems.

To allow dynamic analyses of integrated systems, a generalized, simplified, but accurate model of an LH-TES system is needed. The proposed work is focused on developing a validated, simplified thermal hydraulic model of a LH-TES system, that would facilitate dynamic testing and comparative analysis. The model developed in this study will facilitate preliminary assessments in regards to scaling and designing the LH-TES for specific heat storage capacities and operating conditions. The expected outcome of this project is the development of a transient model for a LH-TES system which could be easily coupled with other existing heat source and heat sink models, to conduct integrated system-level modeling. Such a model would further the research and development of LH-TES systems and promote widespread consideration of TES systems as a part of efficient and stable hybrid energy systems.

### 1.3 Approach

A three pronged approach is followed to tackle the problem at hand and achieve the goals of this study. This is described as follows:

- 1) **Code Development:** A simple, pseudo-steady state, analytical model based on energy balance is developed in MATLAB to estimate the charging and discharging rates of a simplified LH-TES geometry, and to provide a first approximation for the size the storage required to store a certain amount of energy. This model was developed with the intent to get ballpark estimates of the thermal hydraulic performance of a TES and to test the feasibility of designing such a system. Then, a pseudo-transient

numerical model is developed in MATLAB for the same TES system. This model allows the acquisition of data such as state of charge of the LH-TES, temperature profiles over the entire domain, as well as the melt front location within the molten PCM. The model was developed primarily in MATLAB due to familiarity with the software. This modeling effort is followed by an equivalent model developed using Dymola, a commercial modeling and simulation tool, based on the open-source Modelica modeling language, that utilizes object-oriented programming to model dynamic systems. Dymola permits detailed, transient analyses of component-level and system-level models, thereby allowing the possibility of integration of the LH-TES model in other modeling efforts being carried out at the Idaho National Laboratory (INL).

2) **Computational Fluid Dynamics (CFD)**: Simultaneously, numerical simulations using STAR-CCM+, a commercial CFD tool, are also carried out to better understand the thermal hydraulic behavior of the proposed design. CFD simulations provide additional insights into the thermal performance and flow characteristics of the LH-TES system, that a simplified model would not be able to capture efficiently. Results acquired from the CFD simulations also serve as a benchmark, to compare the performance of the developed models, thereby testing their robustness. STAR-CCM+ also allows the possibility for design optimization, which could be used to model and simulate various designs, thereby increasing the engineering understanding of the thermal hydraulics of LH-TES systems, and broadening the knowledge of possible solutions for energy storage.

3) **Experimental Analysis**: In addition to the modeling efforts, a number of experimental studies on bench-scale LH-TES systems are also conducted. Two designs were studied to acquire empirical data, that is used to validate the developed models and the simulations that were set up using the commercial CFD code. Another reason that this approach was followed is to allow for improvements in the accuracy of the developed,

simplified models, thereby increasing the confidence level with which these models could be used to conduct detailed systems-level analyses. This would help solidify the first step in the large-scale development and deployment of LH-TES systems.

This three pronged approach - developing simplified model from scratch, verifying its performance with robust commercial software, and validating it using experimental results - is followed to produce an accurate, simplified model for a LH-TES system. The knowledge acquired from this study will be extrapolated to develop a lab-scale TES with the intent to be coupled with a Thermal Energy Delivery System loop at the INL. This loop is currently being built to complement modeling and simulation efforts of a nuclear-renewable hybrid energy system, whose goal is to enable NPP operation at  $\sim 100\%$  capacity and store excess energy, when available, for later use [16].

## CHAPTER 2

### Thermal Energy Storage - Technology Overview

#### 2.1 Introduction

Thermal Energy Storage (TES) is a technology that accumulates and releases energy by heating, cooling, melting, or solidifying a storage medium so that the stored energy can be used later by reversing the process for various applications, including power generation. There are three main methods of storing thermal energy, as classified in Fig. 2.1, namely, sensible heat, latent heat, and chemical reaction heat.

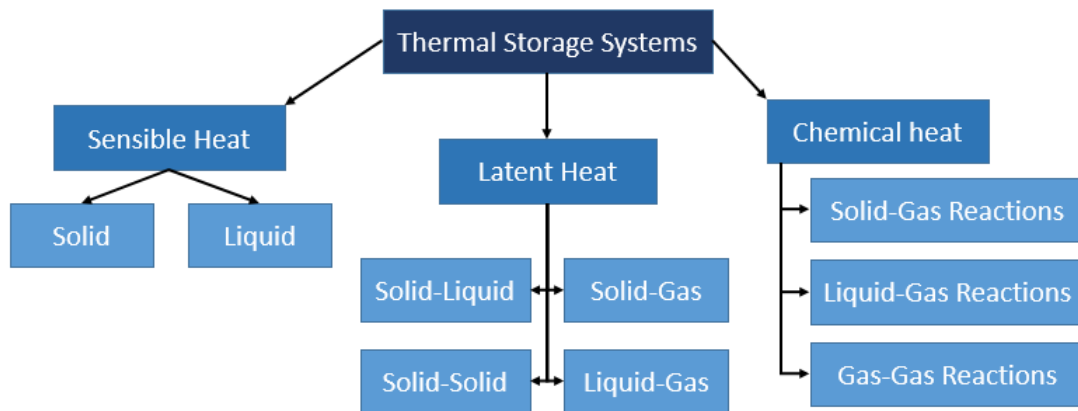


Figure 2.1: Classification of thermal energy storage (TES) systems

Sensible heat is stored due to the phononic contribution of the material wherein the vibrational energy of the molecules manifests itself as an increase or decrease in temperature. Latent heat on the other hand is the energy released or absorbed by a material during a phase transition. The phase change can be from solid-solid, solid-liquid, solid-gas, or liquid-gas. Chemical reaction heat, also known as thermochemical energy, is a result of chemical reactions that release or absorb heat during exothermic or endothermic reactions. If the reaction is reversible, then the chemicals can be used to store or release energy. Equations 2.1, 2.2, and 2.3 express the amount of thermal energy that can be

stored in each of three modes of energy storage.

$$Q_{sensible} = m \int_{T_H}^{T_L} c_p(T) dT \quad (2.1)$$

$$Q_{latent} = m \left[ \int_{T_L}^{T_{melt}} c_p(T) dT + \Delta h_{fusion} |_{T=T_{melt}} + \int_{T_{melt}}^{T_H} c_p(T) dT \right] \quad (2.2)$$

$$Q_{thermochemical} = m \left[ \int_{T_L}^{T_R} c_p(T) dT + \Delta h_{reaction} |_{T=T_R} + \int_{T_R}^{T_H} c_p(T) dT \right] \quad (2.3)$$

Here,  $m$  represents the mass of the storage medium,  $T_L$  and  $T_H$  are the lower and higher temperatures of operation,  $T_{melt}$  and  $T_R$  are the melting point and reaction temperatures,  $\Delta h_{fusion}$  and  $\Delta h_{reaction}$  are enthalpy of fusion and enthalpy of reaction, and  $c_p$  is the specific heat capacity of the material. It is evident from the equations that over a set temperature range, materials with similar specific heat capacities could store more thermal energy by the means of latent heat or thermochemical heat, as compared to sensible heat.

Although thermochemical reactions can theoretically allow higher energy storage capacities when compared to sensible heat and latent heat systems, the technology is still be investigated for its feasibility to be used as large scale TES systems [17]. Most of the research and development for TES applications has been focused primarily on sensible heat and latent heat systems. Within LH-TES systems, the focus is further narrowed down to technologies that employ solid-liquid (and liquid-solid) and liquid-gas (and gas-liquid) phase changes. Although liquid-gas transitions such as evaporation and condensation have higher enthalpies and are used in steam accumulators and cryogenic air energy storage systems, they are impractical for gigawatt-scale deployment, as they would require large storage tanks to be operated at very high pressures. Solid-solid based

PCMs absorb and release heat by reversible phase transitions between a crystalline or semi-crystalline phase, and an amorphous, semi-crystalline, or crystalline phase. However, the amount of energy stored in such a transition is relatively low and thus, is impractical for large scale TES systems.

## **2.2 Literature Review**

### **2.2.1 Thermal Energy Storage Media**

TES systems can be differentiated based on the media they use, as well as the mechanism of to store the energy. In all of the TES technologies, the heat storage media is the most important component of a TES system as it determines the amount of energy that could be stored, the temperature it could be stored at, the duration it could be stored for, as well as the system's thermal performance. Therefore, the selection of a storage medium is thorough process. The most important characteristics of the storage media are its maximum operating temperature range, gravimetric storage density, and cost. Table 2.1 lists some of the commonly used thermal storage media, categorized based on sensible, latent and chemical reaction heat. Cost data are not included in the table as they are closely tied to current market values of storage media, as well as the fact that the storage media's cost is not a reflection of the resultant storage system's cost.

It is evident from the tabulated data that the gravimetric storage capacity, which is an attractive figure of metric for storage systems, is higher for media that could store energy in the form of thermochemical heat. However, thermochemical TES systems that would provide a round trip efficiency comparable to their sensible heat- and latent heat-based counterparts, are yet to be developed and deployed on a practical scale. Therefore, the rest of the chapter focuses on sensible and latent heat storage technologies.

Table 2.1: Commonly used energy storage media

Storage Medium	Specific Heat (kJ/kg-K)	Latent/Reaction Heat (kJ/kg)	Density (kg/m <sup>3</sup> )	Temperature Range (°C)	Gravimetric Storage (kJ/kg)
Concrete	0.9	-	2200	200 - 400	315
Sintered bauxite	1.1	-	2000	400 - 1000	385
NaCl	0.9	-	2160	200 - 500	315
Silica fire bricks	1	-	1820	200 - 800	350
Graphite	1.9	-	1700	500 - 850	665
NaNO <sub>3</sub> -KNO <sub>3</sub>	1.6	-	1815	300 - 600	560
Therminol VP-1 2.5	-	750	300 - 400	875	
Aluminum	1.2	396	2380	0 - 660	397
Nitrate salts	1.5	100	1950	0 - 222	100
Bromide salts	0.53	215	2400	0 - 730	215
Chloride salts	1.1	481	2170	0 - 801	481
Fluoride salts	2.4	1044	2200	0 - 842	1044
SO <sub>3</sub> (g) ↔ SO <sub>2</sub> (s) + 1/2O <sub>2</sub> (g)	-	1225	-	0 - 650	1225
CaCO <sub>3</sub> (s) ↔ CO <sub>2</sub> (s) + CO <sub>2</sub> (s)	-	1757	-	0 - 527	1757
Ca(OH) <sub>2</sub> (s) ↔ CaO(s) + H <sub>2</sub> O(g)	-	1351	-	0 - 521	1351

### 2.2.2 Current Applications of TES Systems

TES systems can be broadly classified as hot or cold storage systems. Hot storage systems raise the temperature of the storage medium above the ambient temperature, to later use the stored energy for heating purposes. Cold TES units lower the temperature of the storage medium below the ambient temperature and then absorb heat from the system to be cooled. As mentioned earlier, the most mature TES technology currently deployed is that of a sensible heat storage system, which is widely used in solar applications, particularly in combination with CSP plants. Herein, radiative heat from the sun is concentrated using mirrors in solar fields to heat the working fluid. This working fluid

then flows to a power block, where heat is extracted from the fluid to produce steam for electricity generation. During hours of low energy demands, the working fluid flows through an intermediary loop and transfers heat to a storage medium. This thermal energy can be stored during the day and used for electricity production even when sunlight is not available.

The Andasol 1, 2 and 3 CSP plants in Spain, are parabolic trough-based power plants that utilize Dowtherm A as their working fluid, which circulates in a closed loop and gets heated by solar radiation from 293°C to 393°C [18]. The heated Dowtherm is pumped back to a power block which uses heat exchangers to produce steam for power generation. A portion of the absorbed heat is transferred to thermal storage tanks, each containing about 28,500 tons of molten salt as the heat storage material. The salt composition is 60% sodium nitrate – 40% potassium nitrate, and is more commonly known as solar salt. Figure 2.2 shows a schematic of one of the Andasol Parabolic Trough Power Plant with its solar collector field, the two-tank sensible heat storage system, and the power generation block. Each of the Andasol units stores about 1,010 megawatts thermal (MWth) power, enough to be able to run the turbines at 50 MW, and produce electricity for about 7.5 hours at full load after sundown, thereby allowing for almost round the clock operations during summer. Similar capacity CSP plants have also been operating in Morocco and in the United States of America [19].

On a residential scale, the Drake Landing Solar Community in Alberta, Canada, uses solar collectors on 52 individual house garage roofs to capture heat and store it in the community's short-term thermal storage system for space heating purposes [20]. About 800 flat-plate roof-top solar collectors with a total of 2293 m<sup>2</sup> area, heat up a water-glycol solution, which is then pumped backed to the community's Energy Center via an underground insulated piping system. There are two short-term heat storage tanks filled with water that absorb the energy from the glycol solution, returning the

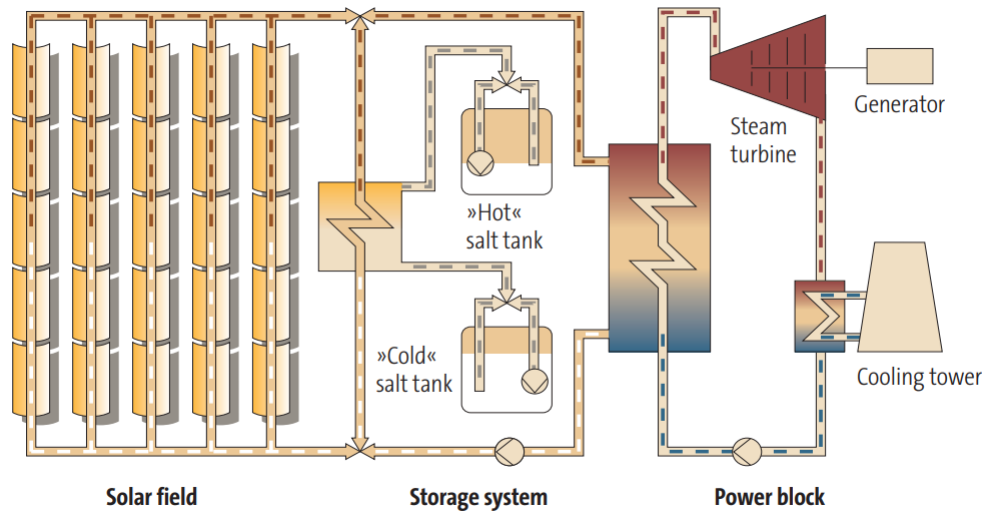


Figure 2.2: Two-tank Sensible-Heat Thermal Energy Storage (SH-TES) system coupled to parabolic trough Concentrated Solar Power (CSP) plant

cold fluid back to the collectors. During nightfall, the short-term storage tanks pump hot water through a secondary district heating loop, connected to each individual house and meets its space heating requirements. During warmer months, the additional heat is transferred from the Energy Center into a nearby borehole TES (BTES) system for long-term storage (see Fig. 2.3). This BTES consists of 144 bore holes that stretch 35m underground, and stores heat during the summer to be used later during winter. This system meets over 90% of the space heating requirements for all the homes in the community which is also about 60% of their energy requirements.

Liquid air energy storage (LAES) is a technology that has gained traction as an efficient and cost effective energy storage method due to their large scale and long duration as well as their compatibility with existing infrastructure. This technology stores energy by liquefying air, thereby reducing the storage volume required when compared to its counterpart, compressed air energy storage system. Due to ease of storage, versatility with which it could be used, and a limitless supply of storage medium, LAES is an attractive energy storage option. The first generation LAES systems were combined with gas turbine-based peaking plants, however, the advanced adiabatic and isothermal

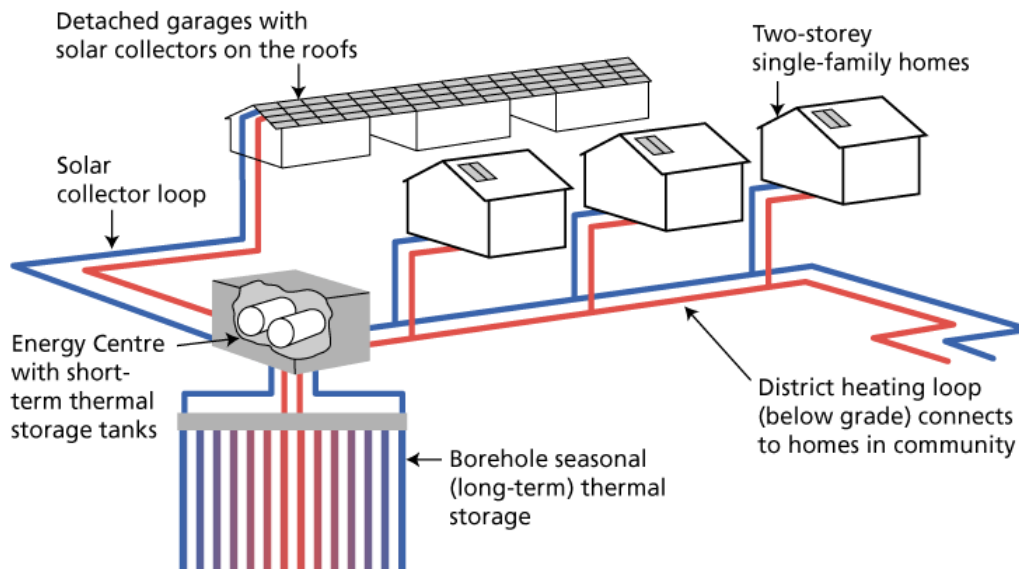


Figure 2.3: Solar seasonal storage and district loop at Drake Landing Solar Community

compression methods that are being developed for compressed air energy storage systems are now being applied to LAES systems, allowing the recovery of clean, stored energy with a round-trip efficiency between 55-80% [21]. Furthermore, utilizing waste heat or cold from other processes, such as LNG terminals or landfill gas engines could further improve the efficiency of this technology and eliminate the need for an external energy source [22]. A schematic of an LAES cycle's working principle is shown in Fig. 2.4.

Steam accumulators are also an attractive option for energy storage that work on the principle of liquid-gas transitions, wherein steam produced by power plants is stored directly in tanks as pressurized saturated liquid. During the discharging cycle of these energy storage systems, steam is produced by opening a valve and lowering the pressure of the saturated liquid, thereby producing steam that can be used for power generation. The feasibility of steam accumulators has been demonstrated by coupling them to direct steam generators (DSGs) that use parabolic trough collectors. Figure 2.5 shows a schematic of a such an integrated system. If the steam production of the collector field exceeds the demand of the turbine, the surplus steam is condensed in the steam accumulator.

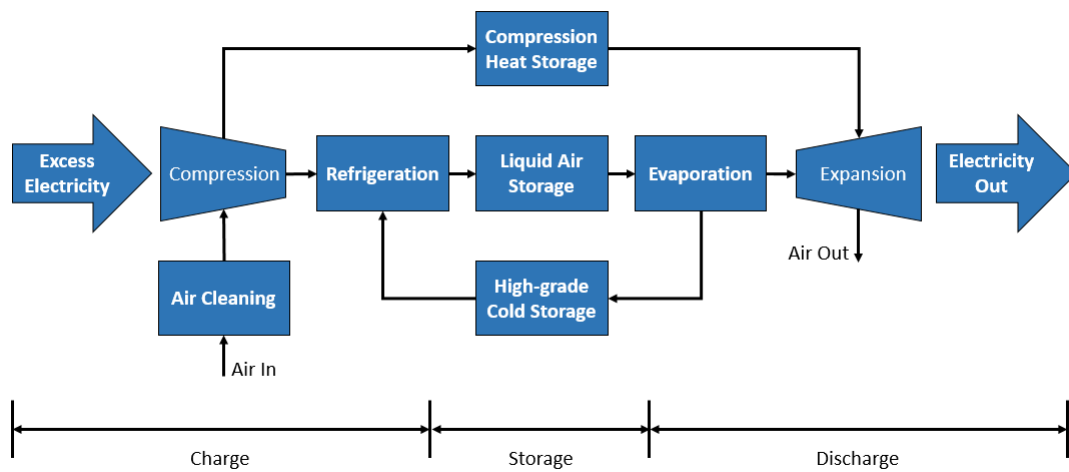


Figure 2.4: Schematic of Liquid Air Energy Storage (LAES) technology [23]

Conversely, during periods of cloud cover, steam is recovered from the accumulator to make up for the shortage of steam from the DSGs [24].

The Planta Solar 10 (PS10) in Seville, Spain is the world's first commercial CSP, which uses movable mirrors, called heliostats, to heat pressurized water at 40 bar to a temperature of 250°C, which is then expanded to run a saturated steam turbine for power generation. To overcome the issues of insolation, PS10 has integrated 4 steam accumulators with a total storage capacity of 20 MWh, capable of running the plant's turbine at 50% workload for 50 minutes [25].

It is well understood that insulation is necessary to minimize the heat loss and gains in buildings. Currently, different types of foams are used as filler materials in walls, which although good insulators, are not capable of regulating temperatures. In order to improve the temperature stability of a building, increasing its thermal mass is crucial. However, this needs to be carried out without additional expenses or increasing the mass of the building itself. PCM embedded concrete walls and wallboards have shown to significantly improve the thermal comfort and reduce the energy consumption of buildings without substantial increase in the weight of the construction materials with the inclusion of PCM [26].

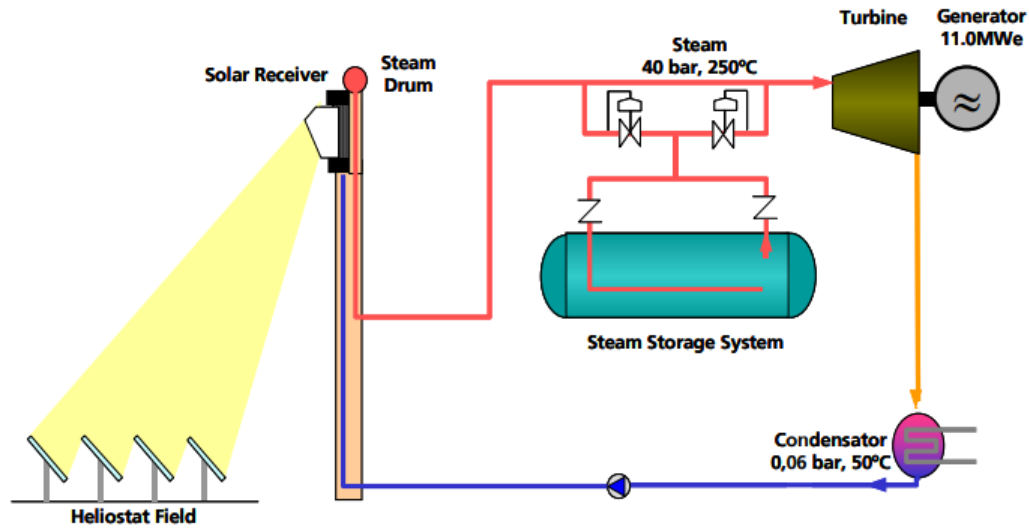


Figure 2.5: Schematic of solar power combined steam accumulator technology for direct steam generation

LH-TES systems are also used in neonatal care such as Miracradle<sup>®</sup> wherein PCMs are used to therapeutic hypothermia among newborns suffering from asphyxia [27]. The light weight, portable device provides precise temperature control of 33-34°C for over 72 hours without the need for constant electric supply. Similarly, the Greenbox packaging system developed by Entropy Solutions uses PCMs to limit heat transfer into or out of the box, ensuring safe transportation of temperature-sensitive products [28]. Such temperature control containers will not only prove to be beneficial to the medical industry, but also to non-profit organizations that provide food at low or no cost to school children and members of under-served communities.

### 2.2.3 Potential Applications of TES Research

With adequate insulation, transportable TES systems could meet the energy demands of a variety of industries. For example, TES systems could be charged at offsite locations with CSPs or other industrial power plants that generate waste heat, and then transported to other locations for heat recovery. Using this technique, several thermal energy sources

can be transferred to a central facility and used to feed a single group of recovery systems in order to mitigate the risk if one of the sources stops producing thermal energy. If excess energy is produced during certain periods of the year, it can be used to reduce energy input to other systems such as space heating, hot water systems and deicing roads/sidewalks.

TES systems can also be modified to accommodate for a variety of charging methods. This would allow the storing of energy from any source that is producing it in excess. For example, wind and solar farms can transfer excess electricity into TES systems via electric heaters. Similarly, off-peak electricity could also be stored in TES systems to be used during peak hours. Not only would this reduce the cost of electricity based on time-of-day pricing, it would also allow for the replacement of fossil fuel-based peaker plants that are required during hour of high electricity demand.

As mentioned earlier, NPPs can be coupled with renewable energy sources such as solar and wind as well as energy storage systems to form a Nuclear-Renewable Hybrid Energy System (N-RHES). Figure 2.6 shows a schematic of such a proposed system which includes the integration of nuclear energy and renewable energy, coupling with thermal and electrical energy storage systems, and the use of this energy in industrial heat processes, as well as power generation. Such a system would be able to respond to the net load by diverting thermal and electrical energy to an alternative user in accordance with the grid dynamics, hence, avoiding over-supply and the associated price suppression. In this manner, NRHES will support levelizing of energy costs daily, weekly, and seasonally.

### **2.3 Technology Selection: Latent Heat Thermal Energy Storage or Sensible Heat Thermal Energy Storage**

Currently, the two-tank SH-TES design is the only system to have been deployed on a gigawatt scale. This system has two tanks to store the hot and the cold storage medium,

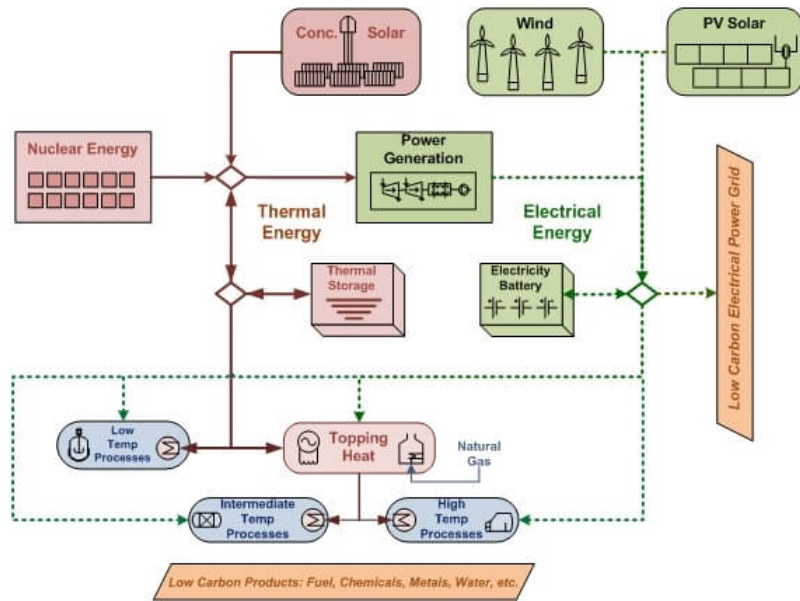


Figure 2.6: Schematic of a potential Nuclear-Renewable Hybrid Energy System

and an intermediary heat exchanger to transfer heat from the storage medium to the HTF (see Fig. 2.2). During the charging cycle, the storage medium is pumped from the cold tank, heated primarily using solar energy and then transferred into the hot tank for storage. During hours of additional demand in electricity, the hot fluid is run through a heat exchanger where it transfers its heat to the HTF and cools down.

Most of two-tank TES systems use molten salt as their storage medium. This is primarily because the salts are cheaper than oils and they have higher thermal conductivities thereby requiring smaller heat exchangers [29]. However, such systems have to constantly maintain the temperature of their heat exchangers and other flow components above the freezing point of the salt to avoid detrimental effects. The entire system has to be kept at a hot standby during periods of no energy demand. Additional inspection is also required for systems with molten salt as their working fluid, which can add to the operational costs of such systems. An LH-TES system can potentially overcome these issues.

The heat storage medium in LH-TES systems is held within a single container

throughout its life cycle and the HTF ideally flows through a heat exchanger embedded within this system, transferring heat to and from the storage medium. This eliminates the need for an external heat exchanger, thereby reducing capital costs. Due to the nature of PCMs being used as storage materials, LH-TES systems have higher energy storage densities, thereby requiring smaller storage sizes as compared to their SH-TES counterparts for the same storage capacity. This is supported by the analysis carried out by [30]. Therein, authors have drawn a comparison between a molten salt-based two-tank SH-TES system and a single-tank LH-TES system. The study considers solar salt ( $\text{NaNO}_3 - \text{KNO}_3$ ) as the PCM, and steam from a nuclear power plant as the HTF. Using appropriate thermophysical properties of the salt and its \$/kg value, a simple sizing and costing analysis was carried out to show that LH-TES systems are a promising candidate for large scale energy storage. This is one of the reasons why LH-TES technology is being investigated in this study.

However, LH-TES systems also have their own drawbacks. The thermal conductivities of the PCMs is the limiting factor which determines how quickly a LH-TES can be charged or discharged. During the discharging cycle, which dominated by conduction, the heat transfer faces an incremental resistance due to the solidification of the PCM around the tubes carrying the HTF. Therefore, in most small-scale latent heat systems, an emphasis is given to enhance the heat transfer mechanism. Some of these mechanisms are discussed later on.

## 2.4 Phase Change Material (PCM) Selection

There are several criteria that need to be taken into consideration while selecting a PCM for an application, however, the most important one of those is its melting temperature. Most PCMs have a melting temperature range bounded by the solidus temperature and the liquidus temperature. The solidus temperature is a limit below which the PCM is

completely solid, and similarly, the liquidus temperature represents the temperature limit above which the PCM is completely liquid. Between these temperatures is a transitional zone, often referred to as a “mushy” zone, which is a semi-solid region existing as an interface between the melted and un-melted regions of the PCM. As temperature difference is the driving force behind heat transfer, the melting point of the PCM needs to be sufficiently lower than the temperature of the heat source during the charging cycle. This temperature difference is also crucial during the discharging cycle, as that would determine how fast the PCM would transfer heat to the heat recovery sink. The heat transfer area also determines the rate at which heat is being transferred to and from the PCM. Increasing the area of heat transfer also increases the amount of material required, thereby increasing the cost of the storage system. LH-TES systems that employ tube-based heat exchangers can lengthen the tubes to increase the heat transfer surface area, however, that would increase the pressure drops in the system.

The chemical stability of the PCM as well as the useful life of the PCM container need to be taken into consideration. Most small scale, low temperature LH-TES systems have been analyzed for paraffins which have confirmed that neither the number of thermal cycles, nor the contact with metals have degraded the thermal behavior of the PCMs. However, such is not the case with more corrosive inorganic PCMs [31]. Some desirable properties of PCM materials are outline below. These are recommendations and not constraints, therefore a balance between them would achieve an optimized system [32].

- PCM should possess high heat of fusion per unit weight and volume, so that small amount of material can hold large magnitudes of thermal energy.
- High specific heat enables the PCM to store more sensible heat.
- PCM should have high thermal conductivity in both the phases which enables storing and extraction of thermal energy from the storage with less temperature gradient.

- PCM should have high density, so that the container required for storage would be small and of low cost.
- PCM should possess low vapor pressure; this gives mechanical stability to PCM containers.
- Volume change during phase transition should be low, so that simple container and heat exchanger can be used.
- PCM should completely melt, i.e., congruent melting, so that segregation can be avoided and homogeneous solid and liquid phases can be obtained.
- PCM should show little or no super-cooling with high rate of crystal growth; this enables melting and solidification to occur at same temperature.
- PCM operation should be reliable without any degradation for long time.
- PCM should possess completely reversible melting and solidification cycle.
- PCM should be chemically stable and non-poisonous.
- PCM should not corrode the container and heat exchanger materials.
- PCM should be non-hazardous and inflammable.
- PCM should be inexpensive, easily available and long lasting.

As no single PCM satisfies the all criterion stated above, so a PCM with more suitable properties needs to be selected. For this study, three commercially available PCMs considered were Paraffin wax, n-Eicosane and Rubitherm GmbH RT27. The thermophysical properties of these three PCMs are provided in Table 2.2 below.

Out of these PCMs, n-Eicosane and RT27 have been well characterized and studied extensively for phase change analyses. These two PCMs are also attractive due to the

Table 2.2: Thermophysical properties of n-Paraffin, n-Eicosane, and RT27

Parameter	n-Paraffin	n-Eicosane	RT27
Melting point (°C)	53 - 57	36.4	28-30
Latent heat of fusion (kJ/kg)	184.5	248	189
Density (kg/m <sup>3</sup> )	829 (s), 0.775 (l)	910 (s), 769 (l)	880 (s), 760 (l)
Specific heat capacity (J/kgK)	2384 (s)	1926 (s), 2400 (l)	2000 (s), 2000 (l)
Thermal conductivity (W/mK)	0.15 (s)	0.426 (s), 0.146 (l)	0.24 (s), 0.15 (l)
Viscosity (Pa-s)	0.0031	Polynomial <sup>1</sup>	0.0032
Thermal expansion coefficient $\beta$ (1/K)	1E-03	8.141E-04	2.59E-03

$$^1 \log_{10} \mu = -9.2095 + 1822.1/T + 1.6798 \times 10^{-2}T - 1.2861 \times 10^{-5}T^2, \quad \text{for } 310 \leq T \text{ (K)} \leq 767$$

proximity of their melting points to the ambient temperature, which results in reduced heat losses to the environment during phase change analysis. Between n-Eicosane and RT27, n-Eicosane was selected because of the consistency with which its thermophysical properties are reported in literature [33, 34, 35, 36]. In comparison, RT27 although equally used for analysis has varying thermophysical properties [37, 38, 39, 40]. Another reason that n-Eicosane is desirable for is that it has a low, singular, melting point making it convenient for experimental and modeling work.

For modeling as well as the experimental work, the HTF is water, and the tube material as well as the body of the bench-scale LH-TES setup is made out of stainless steel 316 (SS316). The thermophysical properties of these materials at standard temperature and pressure is provided in Table 2.3.

Table 2.3: Thermophysical properties of HTF and SS316

Parameter	HTF	SS316
Density (kg/m <sup>3</sup> )	998.2	8030
Specific heat capacity (J/kgK)	4182	502.8
Thermal conductivity (W/mK)	0.613	16.3

## CHAPTER 3

### Thermal Energy Storage - Design

#### 3.1 Introduction

In order to model a LH-TES system, its underlying working principle of melting and solidification needs to be well understood. The first known work for heat diffusion accompanied with phase change was considered by Gabriel Lamé and Benoît Paul Émile Clapeyron in 1831, wherein the authors mathematically modeled the formation of a solid crust on a liquid's surface that was subjected to cooling [41]. Later, Joseph Stefan readdressed the phase transition problems by considering a number of real physical systems, in which the phase boundary moves with time. These are now known as Stefan problems. One of the prominent mathematical formulations derived by Stefan has an exact solution by assuming a Neumann boundary condition, which is called the Stefan-Neumann solution, and is outlined in [42]. Although initially developed as a 1-dimensional problem, many derivations, by assuming a number of boundary conditions, and their corresponding solutions for 2-dimensional Stefan problems have been acquired over the years [43, 44, 45].

Analytical solutions to moving boundary problems have existed for well over a century, however, the assumptions that have to be made to acquire a closed form solution to these problems are seldom applicable to real systems. For instance, the Stefan-Neumann solution to the moving boundary problem assumes pure conduction in the liquid phase and no sensible heating – this is rarely true. The densities of most fluids are temperature dependent, and decrease with an increase in temperature. Uneven heating of a fluid due to sensible heat addition leads to density differences, which results in fluid motion, where the cooler, high density fluid is pulled down by gravity to replace the hotter, lighter fluid. Such a density driven flow is called natural convection, as the fluid motion is not

caused by an external source like a pump, or a fan, or other flow inducing device. This is not captured by the existing analytical solutions. The second assumption to derive the Stefan-Neumann solution is that of a constant boundary temperature. This may also not be the case for most conjugate heat transfer-based systems, where the surface interacting with the PCM is itself being heated or cooled by another fluid. Using these assumptions to model phase change systems will under-predict the time to melt. They will also result in incorrect temperature profiles within the fluid domain as sensible heating of the fluid is neglected. The available solutions are also limited to abstract geometries such as infinite and semi-infinite cylinders, spheres and plane walls. Therefore, any structural modifications that are included within the geometry to enhance heat transfer cannot be accounted for.

It is evident that analytical solutions have their limitations when it comes to modeling complex models that include phase change phenomenon. Although analytical models simplify the problem at hand by making a number of assumptions, this often comes at a cost of accuracy. A more elegant method to acquire accurate solutions is to decompose the problem domain into smaller chunks, solve the governing equations locally over the smaller domains, taking into account the effects of neighboring domains, collate the results and then derive a solution representative of the entire domain, and improve the accuracy by carrying out the calculations in an iterative process. This is possible with numerical methods, two of which are the Finite Difference Method (FDM) and the Finite Volume Method (FVM).

With the advent of computational capabilities and the use of Euler's FDM, which was among the first approaches to acquire numerical solution of differential equations [46], a more discretized solution to the moving boundary problem could be acquired. This method, in contrast to a closed form solution, is based on numerical analysis, and provides state values at discrete locations over the entire solution domain. If modeled

accurately, this numerical method can also account for natural convection-based heat transfer. The FDM was further modified by a number of researchers to develop the FVM, which is now widely used in CFD [47, 48]. This is modeling approach that was selected to develop the numerical models used in this study, and the details of its implementation are provided in section 3.5.2.

## 3.2 Design Review

Modeling of LH-TES systems has attracted a great deal of attention due to their potential of storing large amounts of energy in smaller volumes when compared to their SH-TES counterparts, as well as the capability to operate isothermally. By varying the PCM used as a storage medium, the range of applications that LH-TES systems can be coupled with is plentiful as briefly described in Chapter 2. Recent efforts have mainly been directed towards overcoming the limiting factor of LH-TES systems – the thermal conductivity of the storage medium. Most PCMs that have been widely considered as potential candidates have thermal conductivities of less than 0.7 W/mK which impairs the thermal performance of LH-TES systems [31]. Hence heat transfer enhancement techniques are required to increase the charging and discharging rate. A significant amount of research has been conducted on enhancing the thermal conductivity of PCMs and a variety of heat transfer enhancement methods have been employed on small scale set LH-TES systems. This includes the usage of finned tubes of different configurations [49, 50, 51, 52, 53, 54, 55, 56, 57], insertion of metal matrix or metallic foam into PCMs [58, 59, 33], using PCMs dispersed with high conductivity particles [60], as well as micro-encapsulation of PCMs to increase their heat transfer area [61, 62]. Among these methods, the use of finned tubes is considered to be especially effective and reliable [63]. Not only do fins increase the surface area for heat transfer, they also provide structural integrity to the TES container. Therefore, a decision was made to design the bench-scale

LH-TES studied herein, with axially interconnecting finned tubes.

### 3.3 Design Methodology

Most of the studies analyzing phase change emphasize on predicting the convective heat transfer and the movement of the boundary layer separating the solid and liquid phases. However, due to the complexity of this phenomenon, the solutions that have been developed are applicable only to a specific number of geometries, subjected to a specific set of boundary conditions. Upon reviewing the available mathematical solutions to moving boundary problems, the following conclusions were derived.

- Closed form, analytical solutions can predict the phase boundary in PCMs for a limited number of geometries. However, the boundary conditions are held to be constant.
- Most of the numerical solutions based on FDM or FVM, either assuming the Neumann boundary condition or Dirichlet boundary condition, neglect natural convection within the fluid domain during melting and solidification.
- If natural convection is considered, it is modeled for specific geometries and is therefore not universally applicable.
- The thermophysical properties of all of the materials involved are assumed to be independent of temperature.

As the goal of this project is to generate a dynamic model of a LH-TES for integrated studies, it is vital to maintain the complexity of the model towards the lower end of the prototyping spectrum for early concept validations. Not only are simplified models easier to create, they allow more freedom with respect to alternative designs, thereby allowing easy improvements. An additional benefit of the low-complexity model is its

computational cost. By making several assumptions to simplify the modeling, while being able to capture the underlying physics, simplified models result in faster simulation runtimes. Due to these reasons, the current work is focused on developing a simple, but accurate, dynamic LH-TES model, that is validated experimentally. The design is also made generic so as to allow different fin shaped enhancements to improve the heat transfer performance of the LH-TES system.

A design methodology is followed to develop a generalized model, capable of providing adequate information for preliminary thermal hydraulic analysis of a LH-TES system. The goal is to first develop a math- and physics-based model, test its accuracy, check its acceptability, then increase the accuracy using validation processes. A flow chart for the design methodology followed is shown in Fig. 3.1. Although, this methodology captures the LH-TES design process from conception to industrial deployment, for this study, only a few of the steps shown in the flowchart were followed.

### 3.4 Component Design

A schematic of a generic LH-TES provided below in Fig. 3.2 describes its basic working principle. Excess thermal energy diverted from a high temperature source can be used to deposit heat into the LH-TES via an HTF, thereby melting the storage medium and charging the TES. Similarly, during periods of energy demand, a heat recovery fluid can be run through the TES to absorb the stored heat, thus discharging the system to produce energy for industrial heat purposes or power generation.

For this study, a modified multi-tube shell and tube arrangement is chosen to design the LH-TES battery. As mentioned previously, the main focus of this study is to analyze the performance of a finned tube LH-TES system, however, to understand and quantify the enhancement to heat transfer that the addition of fins would bring about, an unfinned design is also studied. Axially finned tube design was chosen as the fins are simple

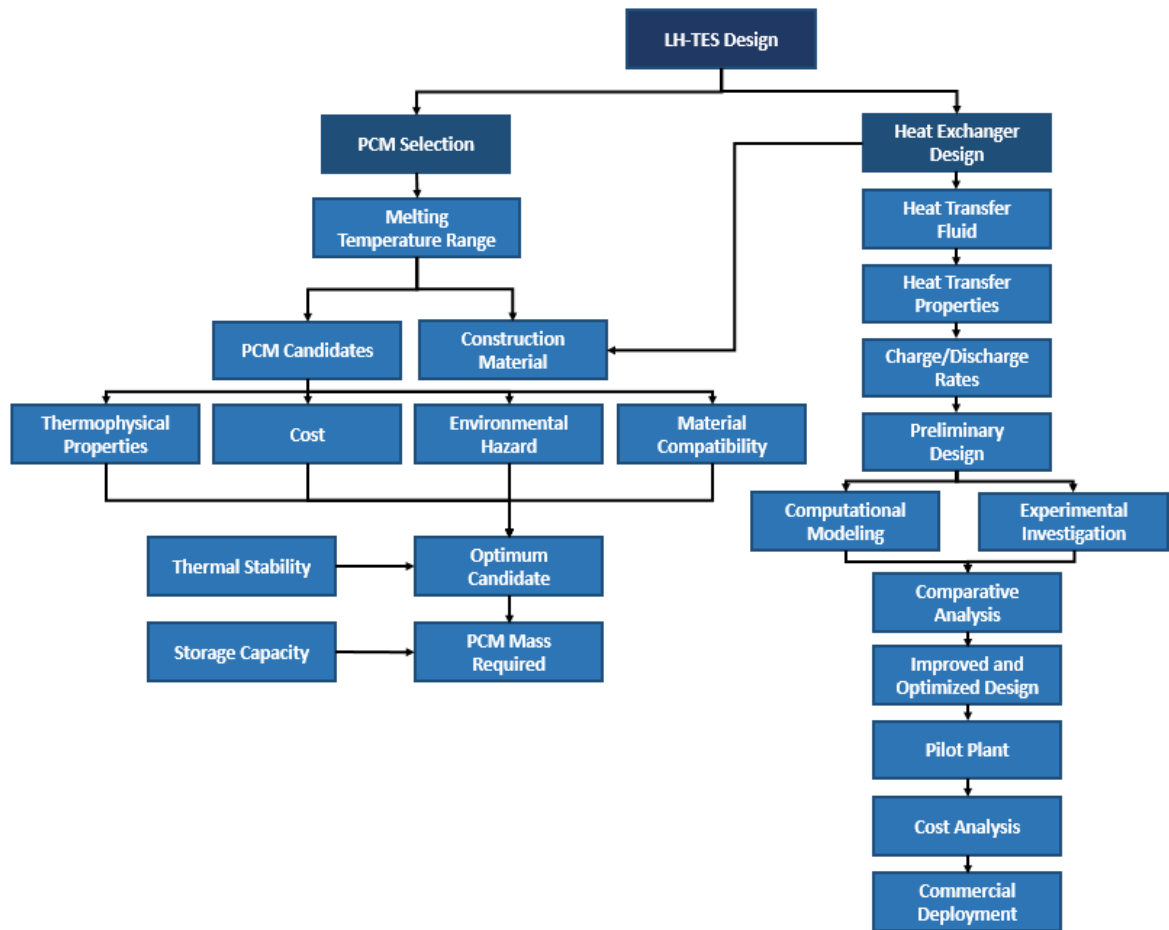


Figure 3.1: Flowchart of a proposed design methodology for LH-TES system development to manufacture and the provide large heat transfer surface area, which is crucial for conductive heat transfer. Moreover, techniques such as impregnation of PCMs with conductive materials, or using suspended conductive additives are still in the preliminary research phase, whereas finned tube designs are a well established technology.

To maintain similarity between both the designs, they are manufactured to have the same dimensions and the same material. The unfinned design was fabricated by welding individual parts that were milled on a CNC machine and pre-cut SS316 tubes, whereas the finned TES design was fabricated using 3D metal printing. Chapter 4 provides more information on the design and geometry specifications of the TES systems. The tubes

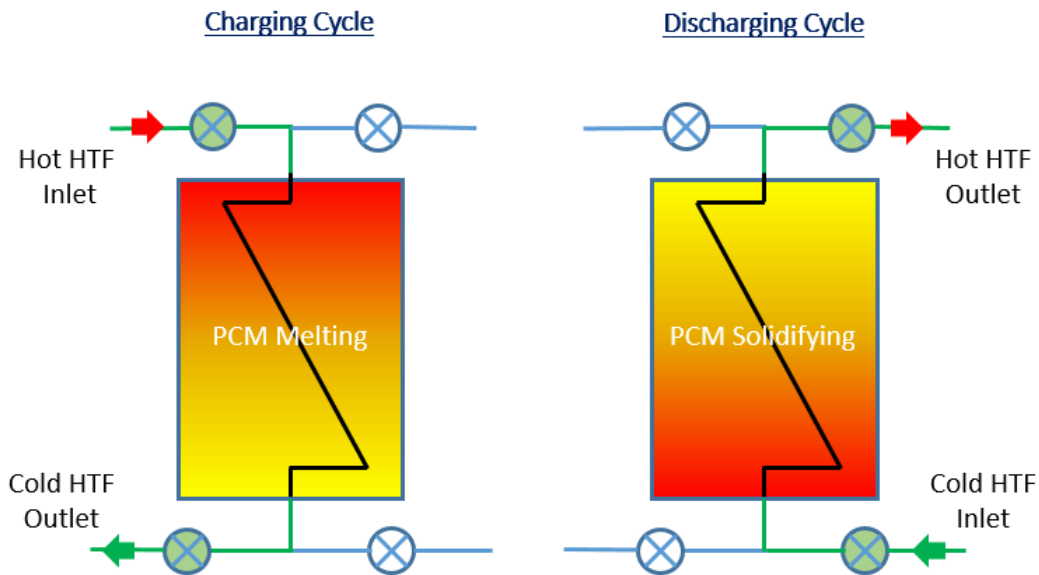


Figure 3.2: Schematic of the working principle for a generic LH-TES system

carry the HTF and are embedded within the shell which contains the PCM. For the finned tube design, these embedded tubes form an interconnected web, within which the PCM is stored. As all the tubes have the same dimensions and are spaced equally apart, each individual tube, along with its neighboring PCM can then be considered as a unit cell. Figure 3.3 shows a top-view schematic of a potential tube arrangement for finned and unfinned tubes. The quadrilateral arrangement can be subdivided into smaller unit cells, each containing a single tube and a portion of its surrounding PCM. The dashed lines represent the boundaries of these unit cells. Assuming that no unit cell affects its neighbor, a single unit cell can be chosen for analysis as a representative of the entire storage system. This assumption reduces the computational cost of modeling the LH-TES system.

The positioning of the tubes in relation to each other dictates the number of fins each tube would have, and the amount of PCM it would directly interact with. For an array of tubes in the quadrilateral arrangement as displayed in Fig. 3.3, the influence zone of each tube – representing the boundary of its unit cell – has a varying radius,

with the ratio of the largest to the smallest radii being  $\sqrt{2}$ . Such a design is difficult to model in the analytical as well as numerical form. Also, it also limits the number of fins connecting a tube to its immediate neighbors to 4 (see Fig. 3.3b).

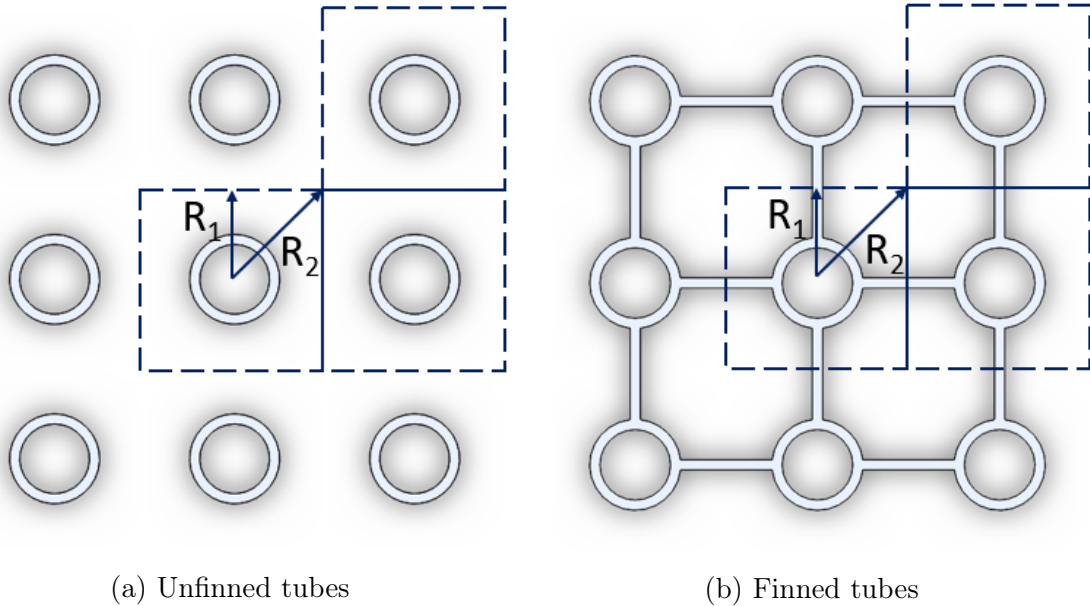


Figure 3.3: Potential quadrilateral tube arrangement in an LH-TES

In comparison, a hexagonal pattern of stacking the tubes as shown in Fig. 3.4 increases the symmetry of the influence zone, with the ratio of the largest to the smallest radii being  $2/\sqrt{3}$ . The finned version of this arrangement also increases the number of interconnecting fins to 6 (see Fig. 3.4b).

To further simplify the mathematical modeling, the influence zone is assumed to be circular (see Fig. 3.5) with an adjusted diameter, which maintains the same PCM volume that a single hexagonal unit cell would contain. This additional simplification creates unit cells that are cylindrical, resulting in a close equivalence to a shell and tube heat exchanger.

It should be noted that only a small sub-section of the tube arrays are shown in Figs. 3.3, 3.4, and 3.5. This geometric pattern can be expanded radially to increase the number of tubes as well as the LH-TES capacity. In order to convert the geometry from

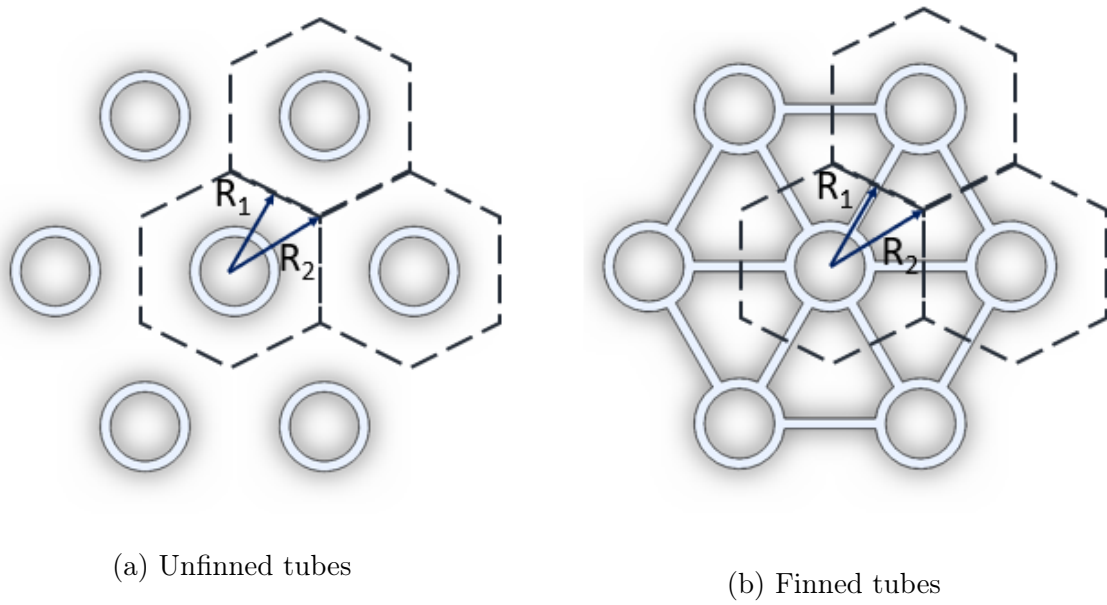


Figure 3.4: Potential hexagonal tube arrangement in an LH-TES

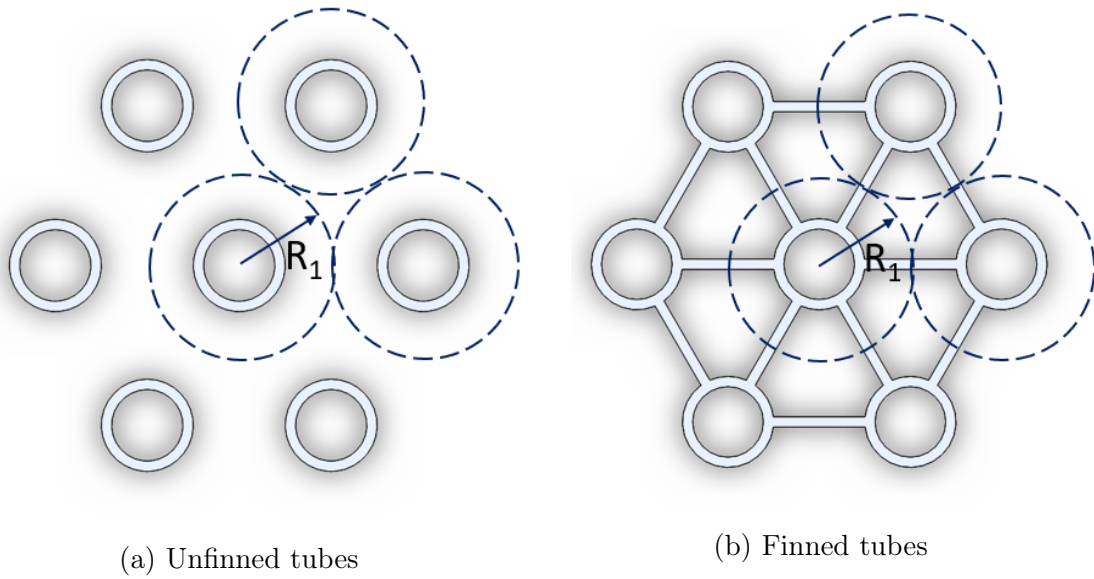


Figure 3.5: Potential hexagonal tube arrangement in an LH-TES with a modified cell boundary

a hexagonal design to a circular for the purposes of modeling simplification, the following methodology was followed.

### 3.4.1 Geometrical Analysis

The fill level of PCM was maintained to less than 95% of the total height of the test section in order to account for thermal expansion of the PCM during melting. Therefore, for an 20.32 cm (8 inch) tall test section, the PCM fill level for the finned design is maintained at 19.05 cm (7.5 inches). Based on this height, the total volume of the PCM in the finned tube design about 1311 cm<sup>3</sup> (80 in<sup>3</sup>). Using this volume, the average thermophysical properties of n-Eicosane from Table 2.2, and an operating temperature range of 21°C to 60°C, the amount of heat stored in the test section is calculated, with the help of equation 2.2, to be 366 kJ. This is a little over 0.1 kWh of storage capacity. Although this is a very small amount, the goal of this study is to provide a validated models based on a proof of concept. The modeling efforts from this work will be extrapolated to build a larger, lab-scale LH-TES system.

### 3.4.2 Effective Thermal Conductivity

In order to develop a generalized model for a finned tube system, there is a need to accurately account for the enhancement in heat transfer that the fins bring about, without limiting the model to this specific geometry. In order to do so, an *effective thermal conductivity* is derived.

Several correlations can be found in literature where authors have used volume fractions or mass fractions, to calculate the effective thermal conductivity,  $k_{eff}$ , of a finned tube surrounded by PCM. The most commonly used formula is as follows

$$k_{eff} = v_{pcm}k_{pcm} + v_{fin}k_{fin} \quad (3.1)$$

where  $v_{pcm}$  and  $v_{fin}$  are volume fractions, and  $k_{pcm}$  and  $k_{fin}$  are the thermal conductivities of the pcm and the fin material, respectively. However, this formulation assumes

that the fin material is homogeneously mixed with the PCM material. This would only be true if a matrix of fine metal filings or a metallic mesh were uniformly suspended in the PCM. As that is not the case with the model considered for this study, this derivation was rejected, and instead a resistance network-based effective thermal conductivity was derived, which accounts for the increased surface area due to the addition of fins.

Figure 3.6 shows the heat transfer path for the modified unit cell presented in Fig. 3.5b, and its corresponding thermal resistance network. During the charging cycle, heat flows from the HTF to the tube, and then into the PCM from the tube wall and the fins. The path is reversed during the discharging cycle. For simplicity, only  $1/6^{th}$  of the domain is considered for the derivations that follow. This includes two-halves of a fin, and a  $60^\circ$  circular sector of the HTF, the tube wall and the PCM.

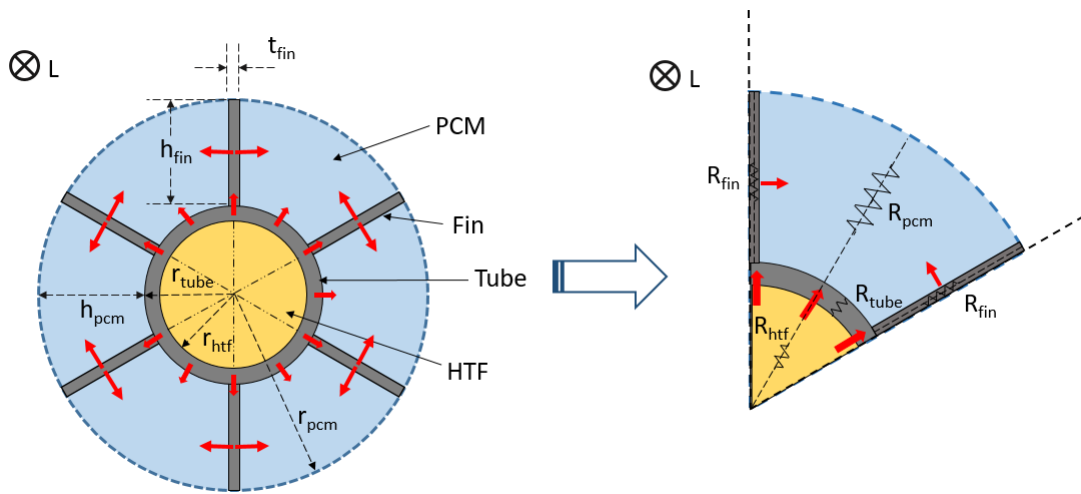


Figure 3.6: Heat transfer path and thermal resistance in finned tube

From Fig. 3.6, it can be seen that the dimensions of the fin are  $h_{fin} \times t_{fin} \times L$  where  $h_{fin}$  is the height of the fin,  $t_{fin}$  is its thickness and  $L$  is the length of the unit cell. Similarly, the dimensions of the PCM domain are  $h_{pcm} \times arc_{pcm} \times L$ , where  $h_{pcm}$  is the height of the PCM section calculated by subtracting the tube's outer radius from the PCM radius, and  $arc_{pcm}$  is the arc length that represents the effective thickness of

the PCM, calculated at  $(r_{pcm} + r_{tube})/2$ . The dimensions used for the study herein are presented in Table 3.1.

Table 3.1: Unit cell dimensions

Parameter	Value
$h_{fin}$ (in)	0.25
$t_{fin}$ (in)	0.028
$r_{fin}$ (in)	0.375
L (in)	7.5
$h_{pcm}$ (in)	0.25
$r_{pcm}$ (in)	0.375
$r_{tube}$ (in)	0.125
$r_{htf}$ (in)	0.097
$arc_{pcm}$ (in)	0.238
$arc_{tube,o}$ (in)	0.131

The thermal resistance network within the  $1/6^{th}$  conical section can further be simplified using a set of thermal resistances in series and parallel as shown in Fig. 3.7. This figure shows an ideal representation of the thermal resistance network between the different component centroids (highlighted in green), which transfers the heat to and from the HTF. The centroids represent points of average temperature in the specific domain.

In order to derive an effective thermal resistance, the following assumptions are made:

- Heat is transferred normal to the surfaces
- The temperature at the centroids is representative of the entire domain
- There is no contact resistance between the individual domains

Using the dimensions of the individual sections and Fourier's Law of heat conduction, the thermal resistances as shown in Fig. 3.7 are written as follows.

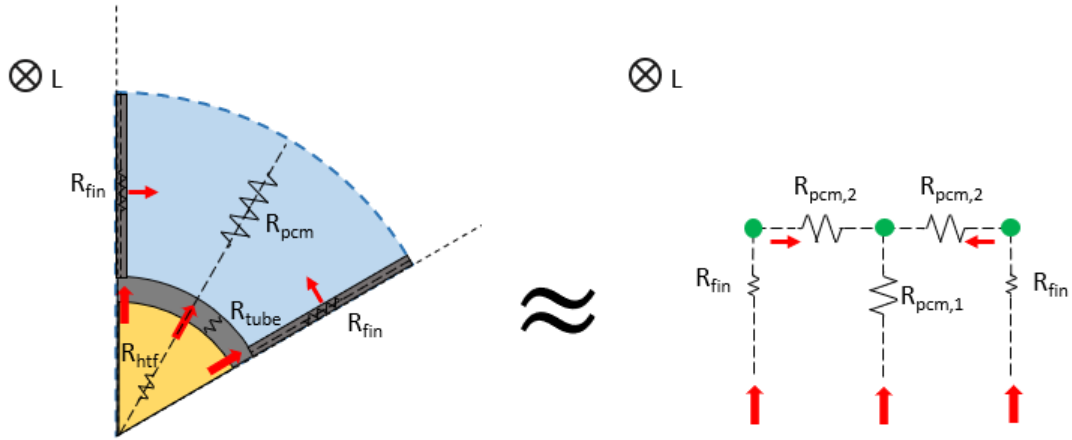


Figure 3.7: Simplified thermal resistance network in a finned tube

The resistance within the tube wall is

$$R_{tube} = \frac{\ln\left(\frac{r_{out}}{r_{in}}\right)}{2\pi k_{tube} L} \quad (3.2)$$

the resistance within the a single fin is

$$R_{fin} = \frac{h_{fin}/2}{k_{fin} A_{fin}} \quad (3.3)$$

the resistance between the tube wall and PCM is written as

$$R_{pcm,1} = \frac{h_{pcm}/2}{k_{pcm} A_{pcm,1}} \quad (3.4)$$

and the resistance between the tube fin and PCM is written as

$$R_{pcm,2} = \frac{arc_{pcm}/2}{k_{pcm} A_{pcm,2}} \quad (3.5)$$

Here,  $A_{fin}$ ,  $A_{pcm,1}$  and  $A_{pcm,2}$  are given by

$$A_{fin} = t_{fin}/2 \times L_{fin} \quad (3.6)$$

$$A_{pcm,1} = arc_{tube} \times L_{pcm} \quad (3.7)$$

$$A_{pcm,2} = h_{fin} \times L_{pcm} \quad (3.8)$$

As there are three resistance networks in parallel comprised of resistances in series, as shown in Fig. 3.6, namely,  $R_{fin} + R_{pcm,2}$ ,  $R_{tube} + R_{pcm,1}$ , and  $R_{fin} + R_{pcm,2}$  - the overall effective resistance is written as

$$\frac{1}{R_{eff}} = N \left( \frac{1}{R_{fin} + R_{pcm,2}} + \frac{1}{R_{pcm,1}} + \frac{1}{R_{fin} + R_{pcm,2}} \right) \quad (3.9)$$

Where N is the number of fins and its adjacent PCM zone, which for this study is 6. The modified resistance network with an effective resistance in the PCM domain is shown in Fig. 3.8.

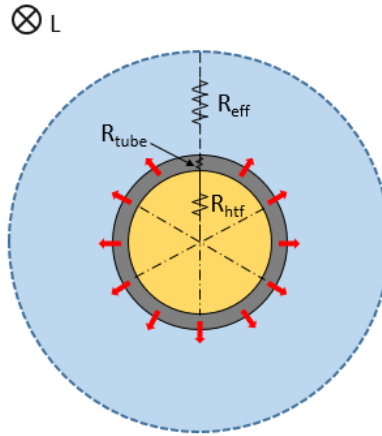


Figure 3.8: Effective resistance network for a finned tube

This calculated effective resistance is then used to calculate the effective thermal conductivity in a cylindrical geometry as shown in equation 3.10.

$$k_{eff} = \frac{\ln \left( \frac{r_{pcm}}{r_{tube,o}} \right)}{2\pi R_{eff} L} \quad (3.10)$$

Using average thermophysical properties of n-Eicosane provided in Table 2.2, the thermophysical properties of the tube material from Table 2.3, the unit cell dimensions from Table 3.1, and equations 3.2 - 3.10, the effective thermal conductivity is calculated to be 1.27 W/mK. The use of this effective thermal conductivity allows the simplification of the design of a finned tube LH-TES to an unfinned setup.

Taking the height of the PCM into account and the number of individual cells in a test section, the volumes occupied by the HTF, the finned tube and the PCM, in a single hexagonal finned tube unit cell, as shown in Fig. 3.4b, are calculated. While maintaining the volumes for the PCM, the unfinned tube and the height, the dimensions of an equivalent cylinder are calculated. This conversion is shown in Fig. 3.9 below. The diameter acquired from this simplification is used in the analytical and numerical models presented hereafter. The volumes of each of designs used in the geometrical analysis are provided in Table 3.2.

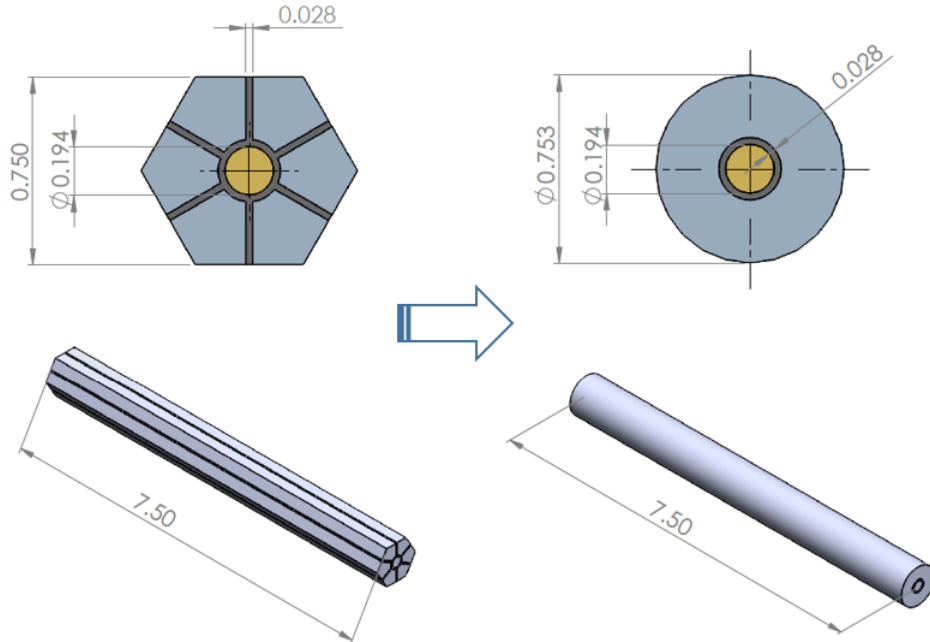


Figure 3.9: Geometric simplification for modeling - finned hexagon to simplified cylinder

The individual tubes can now be represented in an arrangement similar to the tubes

Table 3.2: Dimensions of hexagonal and simplified cylindrical unit cells

Design Parameter	Finned Hex	Unfinned Circle
PCM Volume (in <sup>3</sup> )	2.97	2.97
HTF Volume (in <sup>3</sup> )	0.22	0.22
Tube Volume (in <sup>3</sup> )	0.146	0.146
Fin Volume (in <sup>3</sup> )	0.315	N/A
Fin Fraction (%)	9.6	N/A
Length (in)	7.5	7.5
Domain Thickness (in)	7.5 (flat-to-flat)	0.7528 (O.D.)

within a shell-and-tube heat exchanger. With their surrounding PCM, these individual tubes constitute a unit cell which is the geometry that all of the models developed in the study are based on. The design simplification and derivation of the models is described in the following sections.

### 3.4.2.1 Design Simplification

All of the finned tubes are represented as simple bare tubes in a shell-and-tube heat exchanger configuration, surrounded by PCM with an enhanced thermal conductivity (see Fig.3.10).

The cylindrical unit cell is assumed to be axisymmetric i.e. azimuthal symmetry in all aspects, and therefore a 2D slice of the geometry, as shown in Fig. 3.11, is used as the domain over which the model is solved. This allows the analysis of a 3D model that has no circumferential gradient, using a simplified 2D region, thus reducing computational cost.

The thermophysical properties for the HTF are based on its inlet condition, and the mass flow rate for a single tube is acquired by dividing the total mass flow rate by the number of tubes within the system. All the heat lost by the HTF is transferred into the PCM during the charging cycle and the opposite is true during the discharging

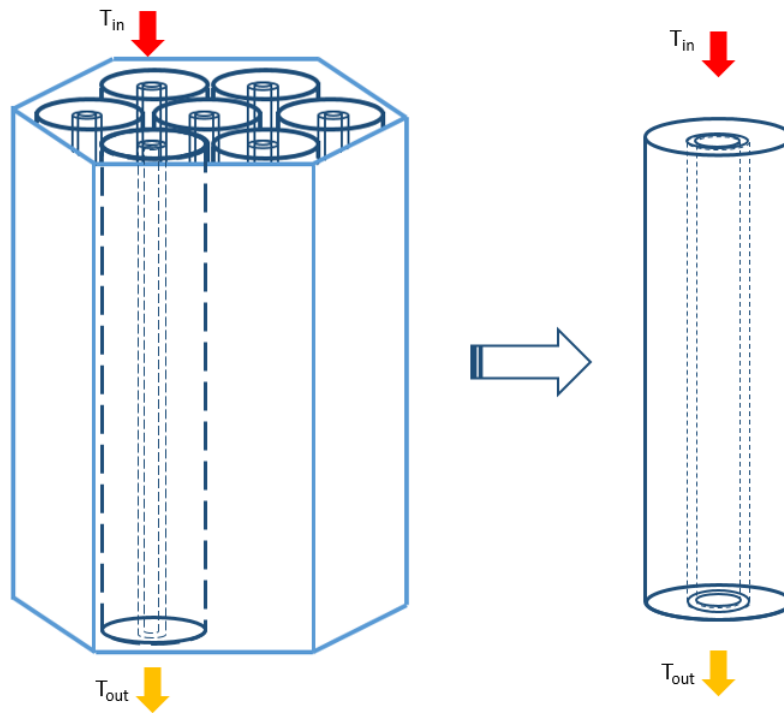


Figure 3.10: Unit cell from a shell-and-tube arrangement for mathematical modeling

cycle. The boundary of the imaginary cylinder is assumed to be adiabatic, based on the assumption that adjacent cells have no effect on each other. The 2D region shown in Fig. 3.11 defines the domain over which the governing equations are solved.

### 3.5 Mathematical Modeling

As mentioned previously, three math- and physics-based models have been developed for the work considered herein, namely, one analytical model and two numerical models. Each of these models have their own variants based on whether the model assumes constant or temperature-dependent thermophysical properties. These models are then compared with each other, and with results acquired CFD simulations as well as those measured from bench-scale experimental setups. The reason to conduct such an analysis is to acquire a simplified, but accurate and robust model of a LH-TES, which would

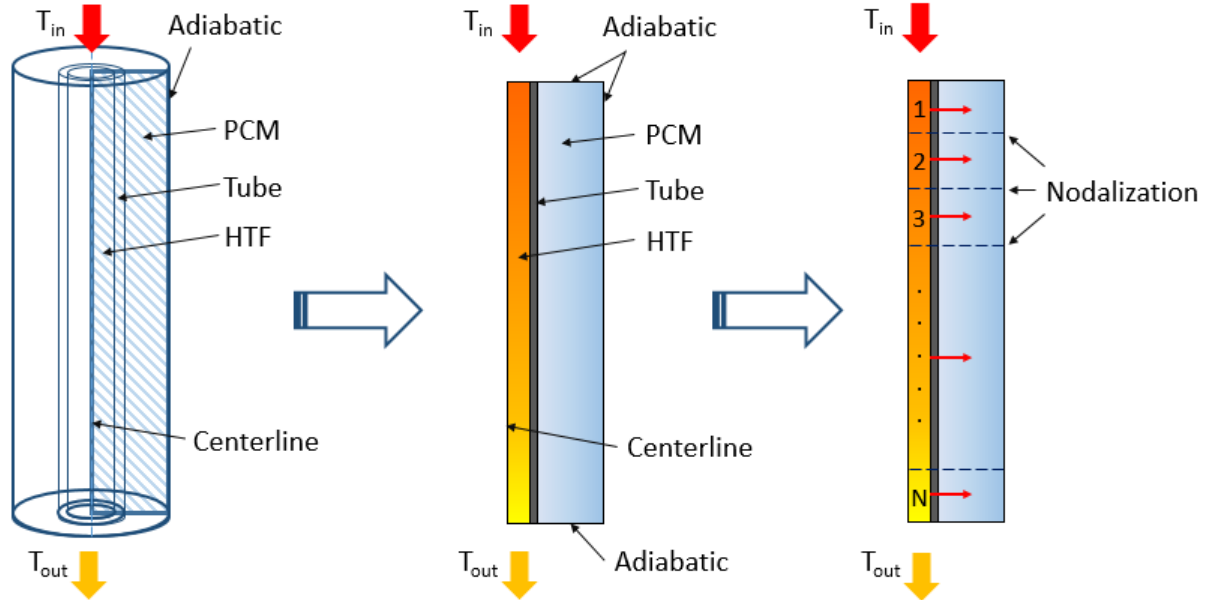


Figure 3.11: Simplification of geometry from 3D to 2D-axisymmetric

allow dynamic integrated system studies.

The simplifying assumptions that all of the models are based on are as follows:

- The HTF is incompressible, fully developed and inviscid
- The PCM is homogeneous and isotropic
- The PCM volume remains constant
- Inlet velocity and temperature of the HTF are constant
- Initial temperature of the entire system is uniform
- The problem domain is axisymmetric
- The outer boundary of the domain is adiabatic

It has been well established that natural convection plays an important role in heat transfer, particularly during melting, as the convection currents determine the shape of

the melt front. For this study, the effect of natural convection in the melt is considered in the numerical models by employing an *apparent thermal conductivity* for the liquid phase using the following correlation:

$$k_{app} = k_{liq} C Ra_w^n \quad (3.11)$$

Here,  $k_{liq}$  is the liquid phase's thermal conductivity,  $Ra_w$  is the Rayleigh number based on an appropriate characteristic length,  $C$  and  $n$  are empirically acquired constants, and  $k_{app}$  is the resulting apparent thermal conductivity in the liquid phase. This correlation was adopted from literature wherein the authors studied the effects of melting and solidification PCMs in rectangular cavities that were heated and cooled from the bottom surface [64, 65, 66]. The values of the constants reported in those studies were 0.5 for the coefficient  $C$ , and 0.28 for the exponent  $n$ .

While applying the apparent thermal conductivity to account for natural convection in the liquid phase, the selection of the characteristic length for Rayleigh number is crucial. It is known that below a certain critical value for this dimensionless Rayleigh number, heat transfer is predominantly conduction based. Therefore, depending on whether the length/height or width of the geometry being analyzed is chosen as the characteristic length, the Rayleigh numbers can differ by several orders of magnitude, thereby resulting in apparent thermal conductivities of different orders of magnitude. The characteristic length is often described as the length scale over which the temperature gradient is established. For the design analyzed in this study, the temperature gradient lies along with thickness of the PCM as it is heated and cooled by the vertical tube wall. Therefore, the length scale chosen for this analysis is the PCM thickness.

In the numerical models developed herein, this apparent thermal conductivity is applied only to the part of the PCM domain in which the liquid fraction is 1, indicating complete melt. The rest of the solidified domain has the effective thermal conductivity

that was calculated in section 3.4.2.

### 3.5.1 Analytical Modeling

The first model developed is a pseudo-steady state model that is based on heat balance between the HTF and the PCM. The model uses the dimensions of the 2D-axisymmetric geometry, the thermophysical properties of the PCM, tube, and HTF, as well as the time-step size as input parameters, and calculates the number of time-steps required for the PCM to melt or solidify, depending on whether it is a charging or discharging cycle. Knowing the time step size and the calculated number of time-steps, the total time for melting and solidification is calculated. To improve the accuracy of the model, it is nodalized axially as shown in Fig 3.11.

During the charging cycle, the model assumes that all of the heat from the HTF is transferred directly to the PCM, at its melt front, and that no heat is absorbed by the tube or the molten PCM to increase its temperature. The same is true during the discharging cycle, with the heat now being transferred from the PCM to the HTF. At every time-step, this model calculates the amount of mass that has molten, which allows the acquisition of melt front radius. The time marching of the solution continues until the radius of the melt front is equal to the radius of the PCM. The equations used for the analytical model as described in the following section.

#### 3.5.1.1 Model Equations

Currently, the model is only developed to simulate charging from a fully discharged state, and discharging from a fully charged state, although, a maximum time limit condition could be applied to acquire the melt front profile. The PCM properties used are averaged between the solid and liquid phase values, whereas the HTF properties are calculated using curve-fitted data from the IAPWS IF97 steam tables [67]. Although

using constant thermophysical properties for the PCM is bound to result in modeling errors, the assumption allows significantly faster convergence of the model as repetitive calls to the functions are avoided.

The first part of the model calculates the mass of the PCM required to store a specified amount of energy. If only latent heat addition is assumed, then the relationship between the mass of the PCM, its latent heat of fusion, and the energy stored can be given by equation 3.12.

$$m_{pcm} = \frac{E_{stored}}{\Delta h_{fus}} \quad (3.12)$$

Here,  $m_{pcm}$ ,  $\Delta h_{fus}$ ,  $E_{stored}$  are the mass of the PCM, enthalpy of fusion of the PCM, and energy stored in the PCM, respectively. The second part of the model deals mainly with the thermal hydraulic aspect of the LH-TES and the logic used to set up the rest of the model and the equations used are described as follows.

The initial temperature of the system, which is an input parameter, determines the states of the LH-TES system. Thereafter, knowing the inlet temperature of the HTF, and using a guess for the outlet temperature at the outlet of the first node, an approximation of the heat lost by the HTF,  $Q_{htf}$ , is made using equation 3.13.

$$\dot{Q}_{htf} = \dot{m}c_{p,htf} (T_{f,in} - T_{f,out}) \quad (3.13)$$

Here,  $\dot{m}$  is the mass flow rate of the HTF,  $c_{p,htf}$  is average specific heat capacity of the HTF, and  $T_{in}$  and  $T_{out}$  are the inlet and outlet temperatures of the HTF. If the HTF flow is laminar, a constant Nusselt number of 3.66 is used. This is primarily because the temperature between the inlet and outlet is relatively small, allowing for the assumption of a constant surface temperature. For turbulent flow cases, the mass flow rate and thermophysical properties of the HTF allow the calculation of the Reynolds

and the Prandtl number, which are then used to calculate a Nusselt number using the Dittus-Boelter correlation. This is followed by a calculation of a convective heat transfer coefficient,  $h_{htf}$ , in the HTF. This convective heat transfer coefficient, along with the conductive resistance through the wall and through the liquefied PCM can be related to the product of the overall heat transfer coefficient and the heat transfer area,  $UA$ , as follows

$$UA = \left[ \frac{1}{h_{htf} A_{htf}} + \frac{\ln\left(\frac{r_{tube,o}}{r_{tube,i}}\right)}{2\pi L k_{tube}} + \frac{\ln\left(\frac{r_{melt}}{r_{tube,o}}\right)}{2\pi L k_{pcm}} \right]^{-1} \quad (3.14)$$

Here,  $r_{tube,i}$  and  $r_{tube,o}$  are the inner and outer radii of the tube,  $r_{melt}$  is the melt front distance from the center of the tube,  $k_{tube}$  and  $k_{pcm}$  are the thermal conductivities of the tube material and the PCM, and  $L$  is the length of the domain. The area of heat transfer  $A_{htf}$  is the surface area of the tube, based on its inner diameter. It should be noted that  $UA$  is a function of the melt front radius, and therefore it varies as and when the PCM melts and solidified during the charge and discharge cycles. The product  $UA$  is used to calculate the heat deposited into the PCM,  $\dot{Q}_{pcm}$ , as shown in equation 3.15.

$$\dot{Q}_{pcm} = UA (T_{f,bulk} - T_{melt}) \quad (3.15)$$

Here  $T_{f,bulk}$  is the average temperature of the HTF based on inlet and outlet temperatures of each node, and  $T_{melt}$  is the melting point temperature of the PCM. The difference between the two heat rates is calculated as an error value, and the outlet temperature's assumption is adjusted appropriately using the bisection method until the error is below a certain tolerance.

The advantages of this analytical model are as follows:

- Good first approximation model to allow for sizing calculations
- Easy adjustment of dimensions, thermophysical properties, and state conditions

- Runs faster than the numerical models that have been developed and the commercial software that is used for CFD

whereas, the disadvantages are as follows:

- Does not account for sensible heat addition or removal
- Does not provide information regarding local scalar quantities such as temperature and liquid fraction
- Does not account for natural convection

The analytical model presented so far is only good for a preliminary sizing and pseudo-steady state analysis of the TES under consideration and is not capable of capturing the physics of conjugate heat transfer phenomenon accurately. In order to understand the dynamics of the system, transient models are developed using numerical analyses. The description of these models is provided in the following sections.

### **3.5.2 Numerical Modeling**

Numerical modeling usually involves solving equations for which closed form, exact solutions are not available. It is often referred to as the process of approximating the solution, by iteratively solving a set of equations at a finite number of points or over a finite number of volumes, until a certain tolerance in errors is met. The numerical models developed as a part of this study solve the underlying governing equations, which are PDEs, that describe time-dependent thermodynamic behaviour of the HTF, tube and PCM domains.

#### **3.5.2.1 Governing Equations**

To model any system that carries out heat and mass transfer, three governing equations are required – the continuity equation, the momentum equation, and the energy equation.

If the HTF flow is assumed to be inviscid, incompressible, and fully developed, it is possible to decouple the equations of motion from the equation of energy and ignore the continuity and momentum equations altogether. This being the case for the current analysis, only the energy equation is considered. The differential form of the energy conservation equation in terms of temperature can be written as

$$\rho c_p \frac{DT}{Dt} = -\vec{\nabla} \cdot \vec{q}'' + \dot{q}''' + \frac{Dp}{Dt} + \Phi \quad (3.16)$$

Where  $DT/Dt$  is the material derivative of temperature,  $\vec{q}''$  is the conductive and radiative flux,  $\dot{q}'''$  is the heat generation,  $Dp/Dt$  is the work done due to external compressive/expansion forces, and  $\phi$  is the viscous dissipation. For the temperature ranges that the system is expected to perform within, radiative heat transfer can be neglected. Additional assumptions made to simplify the analysis are as follows:

- There is no internal heat generation
- The external compressive and expansion work is negligible
- Viscous dissipation forces are negligible
- Negligible radiative heat transfer

Based on the assumptions made above, the simplified governing equation can be written as

$$\rho c_p \frac{DT_f}{Dt} = -\vec{\nabla} \cdot \vec{q}''_{cond} \quad (3.17)$$

Splitting the substantial derivative into its components, equation 3.17 can be rewritten as follows

$$\frac{\partial T_f}{\partial t} = \alpha_f \nabla^2 T_f - \vec{v} \cdot \nabla T_f \quad (3.18)$$

Here  $T_f$  is the HTF temperature,  $\alpha_f$  is its thermal diffusivity, and  $v$  is its velocity vector. In cylindrical coordinates, equation 3.18 can be written as

$$\frac{\partial T_f}{\partial t} = \alpha_f \left[ \frac{1}{r} \frac{\partial}{\partial r} \left( r \frac{\partial T_f}{\partial r} \right) + \frac{\partial}{\partial z} \left( \frac{\partial T_f}{\partial z} \right) \right] - \left[ u \frac{\partial T_f}{\partial z} \right] \quad (3.19)$$

It should be noted that the azimuthal terms have been neglected due to the axisymmetric assumption and the radial velocity term is dropped as the flow is assumed to be fully developed. Equation 3.19 now represents the energy equation for the HTF in cylindrical coordinates. Similarly, the energy equation for the tube wall is derived by dropping the advective term, as there is no bulk motion in the tube wall itself. This is represented in 3.20, where  $T_t$  is the tube wall temperature and  $\alpha_t$  is the tube material's thermal diffusivity.

$$\frac{\partial T_t}{\partial t} = \alpha_t \left[ \frac{1}{r} \frac{\partial}{\partial r} \left( r \frac{\partial T_t}{\partial r} \right) + \frac{\partial}{\partial z} \left( \frac{\partial T_t}{\partial z} \right) \right] \quad (3.20)$$

It is more appropriate to derive the energy equation for the PCM in terms of enthalpy and not temperature as phase change is “ideally” isothermal. Therefore, the amount of energy stored within the PCM can be determined more accurately based on the enthalpy of the PCM. The energy equation for the PCM in terms of enthalpy is written as

$$\frac{\partial H}{\partial t} = \alpha \left[ \frac{1}{r} \frac{\partial}{\partial r} \left( r \frac{\partial H}{\partial r} \right) + \frac{\partial}{\partial z} \left( \frac{\partial H}{\partial z} \right) \right] \quad (3.21)$$

Isothermal phase change occurs only for a few pure substances, whereas for the rest, there usually exists a temperature range. Nevertheless, an isothermal assumption during phase change can be made if the the ratio of the sensible heat absorbed during melting to the latent heat is small, which is true for the PCM considered herein.

As there is phase change within the storage medium, it is of vital importance to know what state the PCM is in – completely solid, completely liquid or undergoing phase

change. This can be determined by knowing the liquid fraction of the PCM which is defined as

$$\chi = \frac{m_{liq}}{m_{tot}} \quad (3.22)$$

Where  $\chi$  is the liquid fraction,  $m_{liq}$  is the mass of the liquid PCM and  $m_{tot}$  is the total mass of the PCM. The liquid fraction can also be defined in terms of enthalpy as follows

$$\chi = \frac{H - c_{p,solid}T_{melt}}{\Delta h_{fus}} \quad (3.23)$$

The relationship of temperature and enthalpy is shown using Fig. 3.12. Here, the phase transition is depicted as an isothermal process.

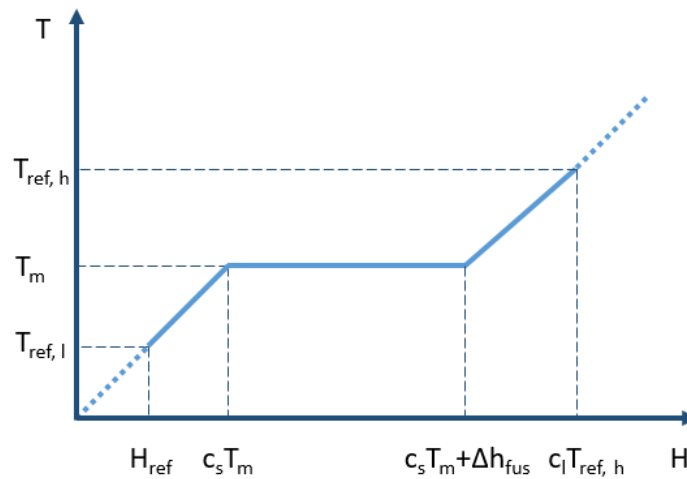


Figure 3.12: Temperature and enthalpy-based plot for isothermal phase transition

The liquid fraction's relation to temperature and enthalpy is equated as follows:

$$\left\{ \begin{array}{ll} \chi \leq 0 & \text{for } H_{ref} \leq H \leq c_{p,solid} T_{melt} \\ 0 < \chi \leq 1 & \text{for } c_{p,solid} T_{melt} \leq H \leq c_{p,solid} T_{melt} + \Delta h_{fus} \\ \chi \geq 1 & \text{for } c_{p,solid} T_{melt} + \Delta h_{fus} \leq H \leq c_{p,liquid} T_{ref,h} \end{array} \right.$$

Here, the lower temperature bound in this case  $T_{ref,l}$  is chosen to be  $0^\circ\text{C}$  at which the enthalpy  $H_{ref}$  is also 0. The lower temperature was chosen appropriately as it is a reference point which can be easily measured. The upper temperature limit  $T_{ref,h}$  is set to be the HTF inlet temperature as that is the maximum temperature the PCM can achieve. Due to the way the liquid fraction relates to the enthalpy, sub-cooled PCM will result in a negative liquid fraction, whereas the value will be greater than unity for sensible heat addition after complete melt. Although this is not the norm in which liquid fraction is described, the model uses a set of conditions to convert the negative values to 0 and those above unity, to 1. When the PCM is melting, that is when the liquid fraction lies between 0 and 1.

As mentioned earlier, the outer wall of the unit cell is assumed to have a zero flux boundary condition, an assumption that can be made at the top and bottom boundaries as well, as the LH-TES is insulated on both ends. Similarly, at the centerline, the flux is zero due to axisymmetric assumption. Having derived the governing equations for the HTF, the tube wall, and the PCM, the 2D computational domain for the single unit cell with its governing equations and appropriate boundary conditions is shown below in Fig 3.13. The boundary conditions are also provided in Table 3.3.

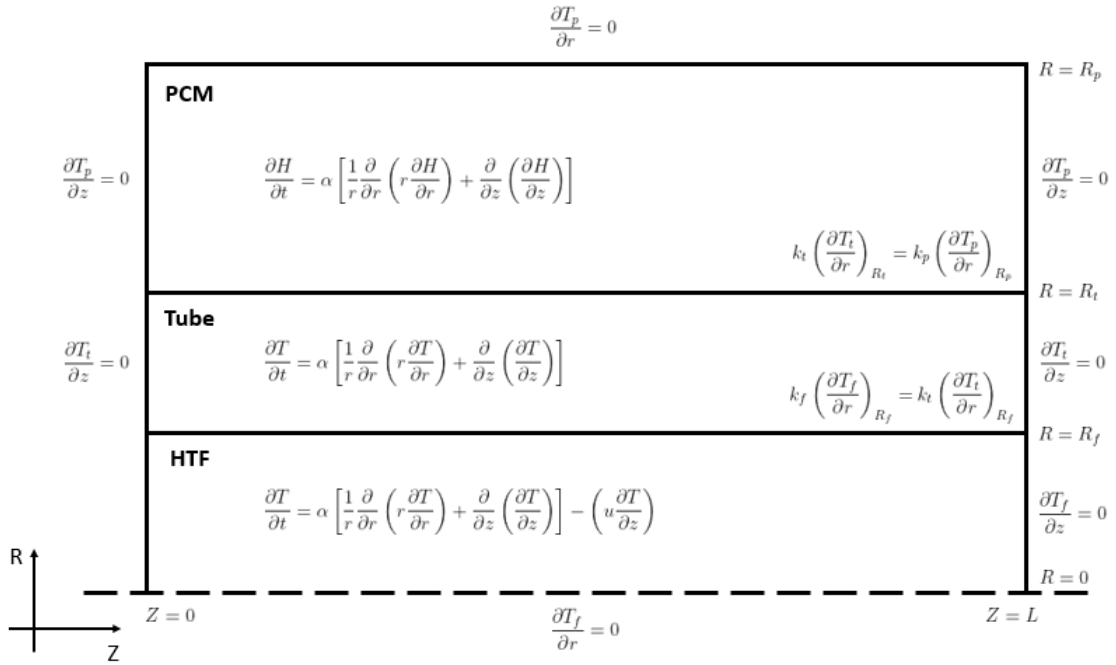


Figure 3.13: Computational domain with differential equations and boundary conditions

Table 3.3: Numerical model boundary conditions

Radial Coordinate	Axial Coordinate	Boundary Condition
$0 < R < R_f$	$Z = 0$	$T_{htf} = T_{in}$
$R_f < R < R_t$	$Z = 0$	$\delta T_t / \delta z = 0$
$R_t < R < R_p$	$Z = 0$	$\delta T_p / \delta z = 0$
$0 < R < R_f$	$Z = L$	$\delta T_f / \delta z = 0$
$R_f < R < R_t$	$Z = L$	$\delta T_t / \delta z = 0$
$R_t < R < R_p$	$Z = L$	$\delta T_p / \delta z = 0$
$R = 0$	$0 < Z < L$	$\delta T_f / \delta r = 0$
$R = R_f$	$0 < Z < L$	$k_f (\delta T_f / \delta r) = k_t (\delta T_t / \delta r)$
$R = R_t$	$0 < Z < L$	$k_t (\delta T_t / \delta r) = k_p (\delta T_p / \delta r)$
$R = R_p$	$0 < Z < L$	$\delta T_p / \delta r = 0$

### 3.5.2.2 Finite Volume Method Discretization

The FVM derives its name from the fact that this method emphasizes the satisfaction of the underlying the governing PDEs on finite-sized control volumes, as opposed to

satisfying them on discrete, individual nodes, which is the principle followed in the FDM method. Figure 3.14 shows a comparison of the spatial discretization followed in the two methods.

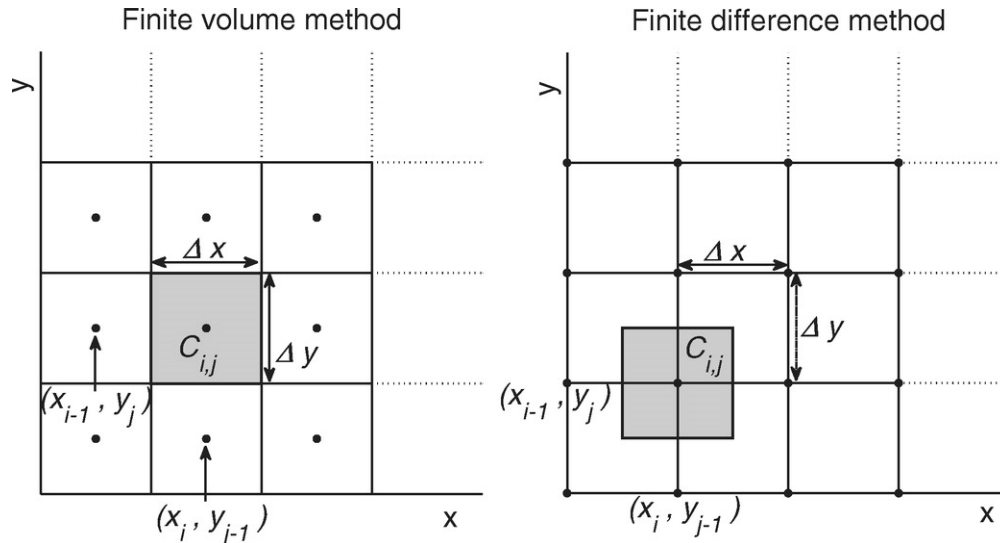


Figure 3.14: Comparison of FVM- and FDM-based grid discretization

In FVM method, the computational domain is discretized into a set of small control volumes called cells. Each cell has a boundary called faces and vertices called nodes. The governing equation PDEs are integrated over the control volumes, allowing the conversion of the divergence terms to surface integrals. Because neighboring cells share a face, the flux entering a given volume is exactly equal to that leaving the adjacent volume. This means that such a method due to its discretization is inherently conservative. This is the reason why the FVM has traditionally been the go-to method to solve CFD problems, and therefore is also applied here.

The transient energy equations shown in equations 3.19, 3.20, and 3.21 have a temporal term on the left-hand-side (LHS) and spatial terms on the right-hand-side (RHS). The first step to solve these PDEs using the FVM is integrating the terms of the governing equations over the volume of the cell. Then by applying the principle of the Divergence theorem [68], these volume integrals are converted to surface integrals. These surface

integrals are then approximated by using various finite difference equations generated using Taylor series, thereby translating the PDEs to algebraic equations.

To approximate the derivatives of the terms on the RHS, a second order accurate Central Differencing Scheme is used for the diffusion terms, whereas a first order accurate Upwind Differencing Scheme is used for the advective term. The difference in methods chosen for approximating the diffusion and advection term derivatives is due to the fact that in advection dominated flows, the node downstream has no effect on its upstream neighbor due to the direction of the flux, as compared to diffusive fluxes that follow the gradient of the dependent variable. Although higher order methods do exist, both of the chosen methods are simple to code and are computationally cheap when compared to the higher order methods. The second order accuracy of the Central Differencing Scheme is attractive because doubling the number of cells reduces the error by a factor of 4.

For the temporal term, both the numerical models had different approaches. Dymola, unlike MATLAB, has an in-built time-derivative analyzing function. Therefore only the partial derivatives for the spatial terms are translated into algebraic equations during the discretization process for the Dymola model. In comparison, the MATLAB model uses the Backward Euler Method to solve for its temporal derivatives. This method although being only first order accurate, is unconditionally stable and can therefore be used with large time-steps, thereby reducing the simulation runtime. It should be noted however, that large time-steps would lead to a large temporal truncation error and therefore an inaccurate solutions. Therefore, the time-step size needs to be chosen appropriately.

While modeling multiple domains, it is important to accurately model interfaces between the control volumes of those two domains which could possibly have dissimilar thermophysical properties. For example, Fig. 3.15 displays a boundary between two cells belonging to different domains having different thermal conductivities  $k_1$  and  $k_2$ . The cell centers of those two cells are at distances  $\Delta x_1$  and  $\Delta x_2$  from the interface.

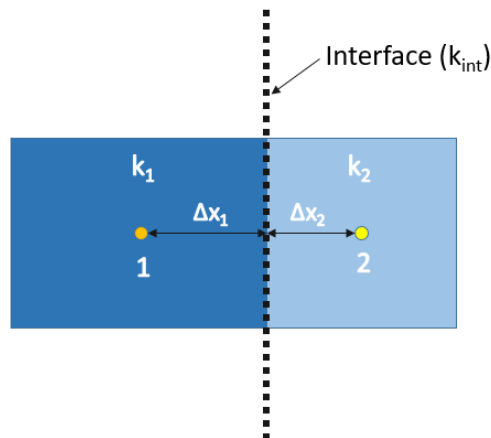


Figure 3.15: Schematic of interface between two cells of dissimilar material properties

A discontinuity in a scalar property such as thermal conductivity could lead to unrealistic results or cause numerical instabilities while resolving the governing equations at the interface. This might be even more critical when the grid sizes used to resolve certain physical phenomenon differ by orders of magnitude. If a fine mesh is modeled next to a relatively coarse mesh, the cell center distances for the boundary cell on each domains might be significantly different. In such a situation, using a simple distance weighted interpolation scheme would lead to incorrect results and in some cases would violate the physical laws. Therefore, an alternative is adopted as presented by [69], wherein an inverse distance-weighted harmonic mean, rather than a distance-weighted arithmetic mean, as shown in equation 3.24, is used.

$$k_{int} = \frac{k_1 k_2}{\frac{k_1 \Delta x_1 + k_2 \Delta x_2}{\Delta x_1 + \Delta x_2}} \quad (3.24)$$

Here,  $k_{int}$  is the interface thermal conductivity, calculated using the thermal conductivities of the two neighboring cells,  $k_1$  and  $k_2$ , and their respective cell-center distances from the interface. This derivation is acquired by setting the flux from one cell to the interface, equal the flux from the interface to the adjacent cell. This interface thermal

conductivity was used at both interfaces appropriately – between the HTF and the inner tube wall, and the outer tube wall and the PCM. Applying the appropriate boundary conditions, as shown in Fig. 3.13, the governing equations were discretized over the three domains using the numerical schemes mentioned earlier.

The advantages of the developed numerical models are as follows:

- Transient analysis of the phase change phenomenon can be observed
- Detailed information regarding melt front location, temperature profiles and state of charge can be acquired
- Fluxes from governing equations are inherently conserved
- Accounts for sensible heat addition in solid and liquid phases
- Can account for natural convection and temperature-based thermophysical properties

whereas, the disadvantages of this model are as follows:

- Slower when compared to the analytical modeled
- Adjustment of parameters such as thermophysical properties of material and dimensions of different domains is slightly difficult
- Changes to variable in one place needs to be adjusted for throughout the code

Once the governing equations to be solved over each domain are simplified to linear, algebraic form, they are solved using a combination of iterative and direct solvers.

### 3.5.2.3 Numerical Solvers and Convergence Conditions

Although direct solutions to a system of linear equations produces no error, it its computational expense compounds when the number of equations is increased. This can

be overcome by using iterative solvers, and the equations can be solved until a certain level of tolerance, commonly known as *residual*, is met. The iterative solver used in this study is the Line-By-Line method. This method takes advantage of the structured geometry, and solves the equations over all nodes lying along the same line in a single sweep, as compared to the Jacobi and Gauss-Seidel methods which solve for values at individual nodes one after the other. It should be noted that the Line-By-Line method is valid only when the nodes that do not belong to the line are treated explicitly. By performing sweeps along a predetermined direction, the coefficients of all the nodes are tabulated in a coefficient matrix, which is then solved using the Tridiagonal Matrix Algorithm solver to get the solution matrix. The values in the solution matrix represent the scalar values of interest at the nodes.

In CFD, the residual measures the local imbalance of a conserved variable in each control volume. Therefore, every cell or node has its own residual value for each of the equations being solved in the domain. It is vital to know this imbalance as it is an indication of whether the solution has converged. However, measuring the residual at each individual node would increase the computational time significantly, and therefore, an accumulated residual is calculated. The approach followed for this study is that of calculating the L2 norm. Details of the application of this method can be found in [69].

A variety of conditions are also applied to prevent the loop from running infinitely. The two main conditions were the total simulation run-time, which is a stopping condition, and a limit to the PCM's volume-averaged liquid fraction, which is a convergence condition. The total run-time is used in analysis of temperature profiles, wherein the maximum limit can be set by the user, and the code will continue to run until the final time-step. No additional calculations are performed for time, as it is an input parameter. In the case of the liquid fraction, the governing equations over all the domains until the average liquid fraction of the PCM is less than 99%. The volume-averaged liquid fraction was

calculated using the following expression

$$\chi_{avg} = \frac{\sum_i^N \chi_i V_i}{\sum_i^N V_i} \quad (3.25)$$

Here,  $V_i$  is the volume of each cell and  $\chi_i$  is its liquid fraction. The volume of each cell is based only on the discretized lengths in the radial and axial directions, as the azimuthal dimensions can be assumed to be unity for a 2D model. The code also contains a break condition on the maximum number of overall iterations, to prevent it from entering into an infinite loop.

### 3.5.2.4 Numerical Model 1 – MATLAB

MATLAB is a multi-paradigm numerical computing environment that allows matrix manipulations, plotting of data and functions, implementation of algorithms, as well as interfacing with other languages. The reason why MATLAB was selected for developing the code is the author's familiarity with the program, thereby easing the code debugging process. The numerical model uses the discretized equations, applies appropriate boundary conditions, and solves them using conditional loops. Section 4.4 presents the robustness of this model for pure conduction-based modeling, and Chapter 6 presents the results generated by accounting for the effects of natural convection. This code is also used as a benchmark for the Modelica-based code developed in Dymola, as both the models are being used to solve the same problem.

As MATLAB does not have an internal time-dependent derivative solver, a set of instructions in the form of a loop are coded for the time marching of the solution. A while-loop was used to set the terminating condition for time advancements whereas multiple for-loops were used to solve the algebraic equations acquired from the discretization process. These for-loops calculate the temperatures in the HTF and tube-wall domain, and the enthalpy in the PCM domain. Each domain calculates its own an L2 norm for

the parameter of interest, upon the satisfaction of which, the specific loop is exited and the next loop begins. Once all of the loops are solved within a time-step, the old values are updated as initial guesses for the next iteration, and the whole set of equations is solved again until the while condition is met.

### 3.5.2.5 Numerical Model 2 – Dymola

Dymola is a commercial modeling and simulation tool based on the open-source Modelica language and is used to develop and analyze integrated, complex systems. The Modelica Language is a non-proprietary, object-oriented, equation-based language to conveniently model complex physical systems containing, e.g., mechanical, electrical, electronic, hydraulic, thermal, control, electric power, or process-oriented subcomponents [70]. The main difference between Modelica and other programming languages is that it is equation-based, therefore allowing the user to provide inputs as physical equations as they are, instead of having to manipulate them to solve for the variable of interest. Dymola is one of many simulation environments for Modelica, wherein users can build models based off existing kernels from various libraries, or generate their own models using fundamental, underlying governing equations.

Currently, a LH-TES system model does not exist in any of the open-source libraries, therefore the development of such a model is crucial. The governing equations used in the MATLAB model and the Dymola model are the same, however, the time variable is a built-in, global variable in the Modelica programming language. Although users are allowed to modify the duration a simulation can run and choose which solver solves the differential equations, no control is allowed over the time-step size. The temporal derivative is a function called *der*, which handles the time-dependent terms and solves for them based on the solver chosen.

Therefore, while coding the governing equations for the Dymola model, only the

spatial terms were discretized, and were equated to the time dependent terms. The default differential equation solver, Differential/Algebraic System Solver (DASSL), was used to solve all of the equations. This solver provides solution for a differential-algebraic equation, by solving the problem semi-implicitly [71]. Although the Dymola model provides the same information that the MATLAB model does, data manipulations is relatively difficult. Therefore, the data acquired from the Dymola model was exported to MATLAB for data visualization.

To test the robustness of the MATLAB-based analytical, and MATLAB- and Dymola-based numerical models, case studies were carried out by varying different parameters of the problem, and the solutions were compared to those acquired from a robust commercial CFD code, STAR-CCM+. The results of these studies are presented in the next chapter.

## CHAPTER 4

### Computational Fluid Dynamics (CFD)

#### 4.1 Introduction

CFD is a branch of fluid mechanics that uses numerical analysis and data structures to analyze and solve problems that involve fluid flows. Computers are used to perform the calculations required to simulate the free-stream flow of the fluid, and the interaction of the fluid (liquids and gases) with surfaces defined by boundary conditions [72]. Numerical modeling using CFD is most useful when experimental or analytical means cannot be pursued. It can also reduce costs that would have otherwise be incurred to construct and perform experiments for every single geometry that can be envisioned. In this study, CFD is used to test the robustness of the developed analytical codes as well as to analyze the thermal performance of the LH-TES system.

Setting up a CFD simulation requires a few key steps – geometry and grid definition, physics model selection, solving the simulation, acquiring the results and post-processing the acquired results. Out of the variety of commercial CFD tools available in the market, STAR-CCM+ version 2019.3 and ANSYS 2019 R2 were considered for this study. However, STAR-CCM+ was chosen over ANSYS for the following reasons:

- STAR-CCM+ offers a very clean, modern interface where one can access all pre-processing, simulation, and post-processing tasks within this single interface.
- Geometries imported into STAR-CCM+ are categorized as *parts* and *parts-based operation* are encouraged by this tool. This ensures that future operations are performed in reference to the original part and not the continuum volume regions/meshes. This allows easy replacement of the part within a simulation if any updates to the geometry are required [73].

- Field functions also known as user-defined functions can be easily coded and applied in STAR-CCM+.
- STAR-CCM+ has a strong mesh generation algorithm. Its novel *polyhedral mesh* is claimed to provide a balance solution for complex mesh generation problems, while having higher accuracy than the traditional tetrahedral meshes [74, 75, 76].
- Last but not least, to run simulations that require a significant amount of computational power, multiple cores are needed. Some of the 3D simulations that were run as a part of this study had over 2 million cells. To run these successfully, and within a reasonable amount of time, the Idaho National Laboratory's High Performance Computer (HPC) was used, and that uses STAR-CCM+. Without the HPC, some of the simulations on an 8-core computer would have taken over 8 months to resolve.

STAR-CCM+ allowed the development of the 2D axisymmetric geometry, mesh generation of the problem domain, selection of the various physics-based models, application of appropriate boundary conditions, and the acquisition of utilizable results through simulation runs. Although the methodology presented in this chapter focuses primarily on the 2D model, the procedure to set up the 3D models is very similar, with the distinctions being mentioned where necessary. This chapter describes the methodology followed in order to set up the 2D simulation and its use to conduct solution verification. A number of case studies are presented, which were carried out to test the robustness of the developed models. It also presents the design specification of the 3D model, which is a more realistic representation of the experimental apparatus.

## 4.2 CFD Simulation Setup

### 4.2.1 Two-Dimensional (2D) Geometry and Grid Definition

A 2D model is set up in STAR-CCM+ based on the axisymmetric assumption presented in Section 3.4. The dimensions this 2D model are shown in Fig. 4.1.

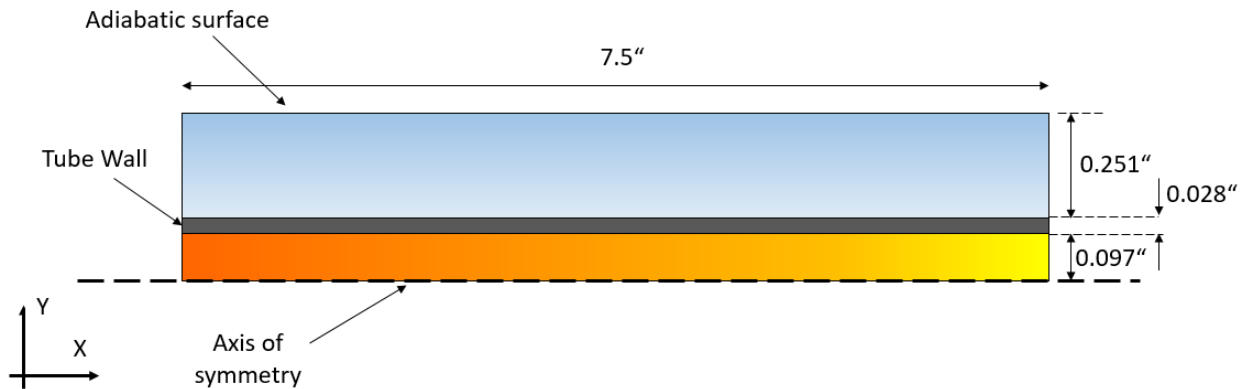


Figure 4.1: Dimensions of 2D problem domain

There are two ways to set up the geometry for the part to be simulated in STAR-CCM+. Either the geometry can be modeled using software's in-built CAD modeler, or it be imported from an external Computer Aided Design (CAD) modeling tool. The latter option is more suitable for complex models and was used in the of 3D simulations. As the 2D geometry is relatively simple, it was modeled without the help of an external CAD tool.

In STAR-CCM+, every model first has to be modeled in 3D and then converted to 2D before meshing. Therefore, the domains of the HTF, the tube wall, and the PCM were sketched as individual, adjacent rectangles, extruded out to a thickness of 1 mm each, and then converted to 2D by using the *Badge for 2D Meshing* operation. This step, ensures that the meshing occurs on the back wall of the extruded 3D cuboid. It should be noted that the norm while simulating axisymmetric models is that the centerline of

the model should lie along the positive X-axis. Then, by selecting the radial direction along the Y-axis, the Z dimension for a 2D model becomes 0. The XY plane is face on which the 2D mesh is generated.

Taking advantage of the 2D geometry, a structured mesh is generated for all the domains with a maximum aspect ratio of about 8. The aspect ratio is a measure of the stretching of a cell, computed as the ratio of its maximum and minimum lengths. It is advisable to maintain an aspect ratio lower than 35 to avoid instabilities in flows that resolve the energy equation [77]. The mesh resolution for each domain used in the preliminary analysis, along with its resulting aspect ratio is provided in Table 4.1.

Table 4.1: Grid resolutions and aspect ratios of domains in the base model

Domain	HTF	Tube	PCM
Grid Points (Axial x Radial)	245 x 10	245 x 5	245 x 24
Aspect Ratio	$\sim 3$	$\sim 6$	$\sim 3$

## 4.2.2 Physics and Boundary Conditions

Once the grid is defined, the next step is to define the continua, which are a set of physics and meshing models that are applied to one or more regions within the simulation. The physics models selected for the pure conduction based analysis are shown in Fig 4.2. Here, each domain has its own continua as they are made of different materials and therefore have different thermophysical properties. For preliminary analysis, averaged thermophysical properties as provided in Table 4.2 were used. The HTF properties are calculated at its inlet temperature, whereas the PCM properties are averaged based on the values provided in Table 2.2. Although this would inevitably lead to errors, this approach has been followed while conducting preliminary analyses in most of the literature that focuses of phase change studies. The effects of this assumption and the discrepancies it brings about have been discussed in later sections.

Table 4.2: Thermophysical properties of materials used in preliminary analysis

Property	HTF (Water)	Tube (SS316)	PCM (n-Eicosane)
Density (kg/m <sup>3</sup> )	998.2	8030	839.5
Specific heat (J/kgK)	4182	502.5	2163
Thermal conductivity (W/mK)	0.6	16.3	0.285
Latent heat (kJ/kg)	-	-	248
Viscosity (kg/ms)	1.003 E-03	-	3.552 E-03
Melting temperature (°C)	-	-	36.4

The physics models selected for each of the domains have to be chosen carefully to avoid incompatibility issues. In order to activate the Volume-of-fluid model and the Eulerian Multiphase model to simulate melting and solidification, the segregated solver had to be selected. The Eulerian model is appropriate for this case as individual particle tracking within the PCM domain is not required.

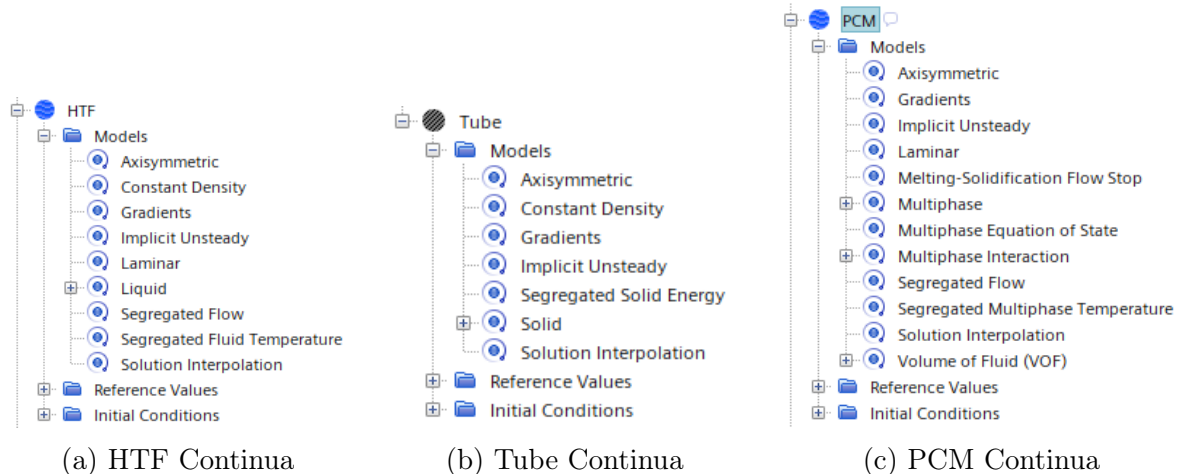


Figure 4.2: Continua used for physics model selection in 2D simulations

Once the appropriate physics models are selected, the boundary conditions are applied. The flow rate in each of the tubes was calculated by dividing the total flow rate by the number of tubes. An inlet temperature of 60°C was selected with a total volumetric flow rate for the LH-TES design of 6 lit/min. Based on these numbers, the flow conditions in a single unit cell are calculated, and are presented in Table 4.3.

Table 4.3: Boundary conditions for base model used in case studies

Parameter	Value
Total volumetric flow (lit/min)	6
Volumetric flow in single tube (lit/min)	0.162
HTF Inlet temperature (°C)	60 (charging)/ 19 (discharging)
HTF density at inlet conditions (kg/m <sup>3</sup> )	983.2
Mass flow rate in single tube (kg/s)	2.655E-3
Cross sectional area of single tube (m <sup>2</sup> )	1.907E5
Velocity inlet for single tube (m/s)	0.142

Four main boundary condition types are set to the boundaries on the 2D domain - the centerline is set as the *axis*, the inlet boundary is set as *velocity inlet*, the outlet boundary as *pressure outlet* and all the external boundaries of the PCM as well as the tube wall are set to *adiabatic*. The interfaces between the domain are of type *contact interface* with a conformal match. The domain boundaries are highlighted in Fig. 4.3 below.

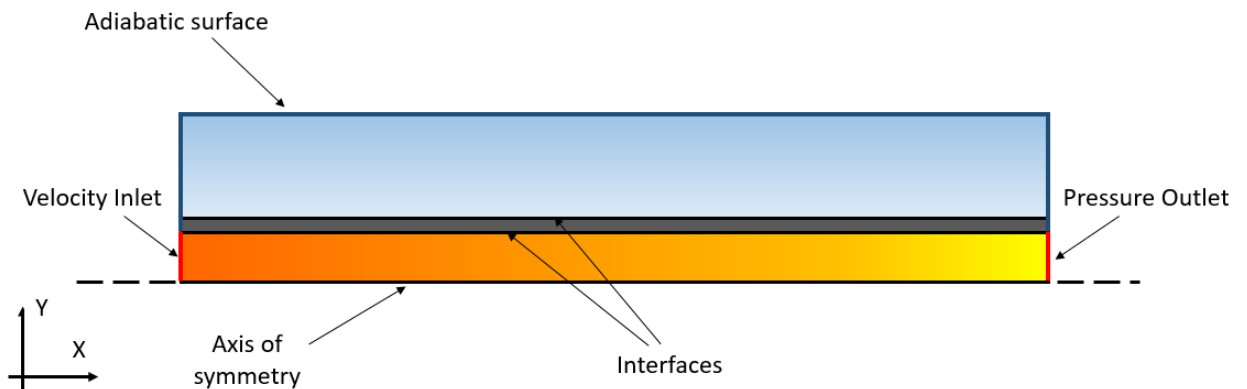


Figure 4.3: Boundaries of 2D problem domain

The initial temperature for all of the domains is set to be 21°C, which was the average temperature of the lab during the experimental runs. This is crucial as this is the starting temperature based on which the developed models, as well as the CFD simulation calculates the temperature for the next time-step.

While solving transient simulations, the user has control over the following parameters - time-step size, the temporal discretization scheme, number of inner iterations, maximum physical time and maximum time-steps. During preliminary analysis of the CFD simulation, the time-step size was chosen to be 0.1s, with 5 iterations per time-step. The stopping criteria during the charging cycle simulations was to stop the simulations once the melt fraction of the PCM had reached 99.9%. Having set up the model with the appropriate boundary conditions, scalar scenes are then set up to acquire temperature and liquid fraction contours. For an equivalent comparison between the CFD and developed numerical models, point probes were placed in the problem domain to record temperature data. Fig. 4.4 shows a scaled schematic of the 2D domain with the point probes, the location of which is provided in Table 4.4. The equivalent representatives to these probes are cells within the data arrays that the developed models generate over their runs.

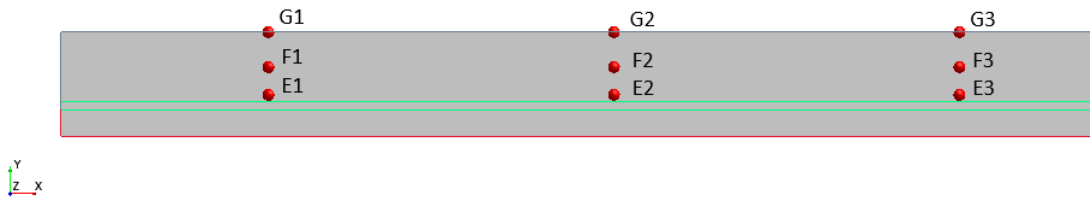


Figure 4.4: Point probes in 2D PCM domain for temperature data acquisition in CFD simulations

Table 4.4: Point-probe locations in 2D PCM domain

Direction	E1	E2	E3	F1	F2	F3	G1	G2	G3
$z$ (in)	1.5	4	6.5	1.5	4	6.5	1.5	4	6.5
$r$ (in)	0.15	0.15	0.15	0.25	0.25	0.25	0.376	0.376	0.376

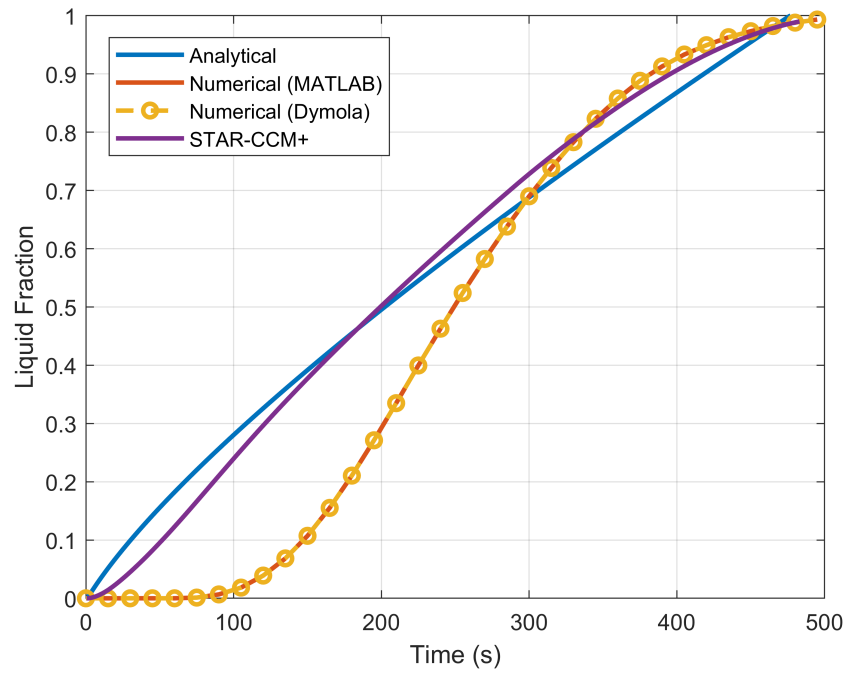
### 4.3 Preliminary Modeling Results - Pure Conduction

A comparison is drawn between the analytical model, the two numerical models, and the CFD model, to gauge the behavior of heat transfer and phase change phenomenon. Thermal behaviour during a complete melt and complete solidification cycles is analyzed, and liquid fraction and temperature profiles are plotted against the cycle times. The melting cycle starts from ambient conditions, with the HTF boundary conditions being adopted from table 4.3. For the solidification cycle, initially, all of the three domains were assumed to be at 60°C. This is based on the maximum achievable temperature in an ideal situation. The HTF temperature during the solidification cycle is 19°C, as this is the average temperature of the water available for experimental studies. As the analytical model cannot provide local temperature data, it is only used to describe the liquid fraction profiles. Figure 4.5 presents data of the liquid fraction behavior for the four aforementioned models.

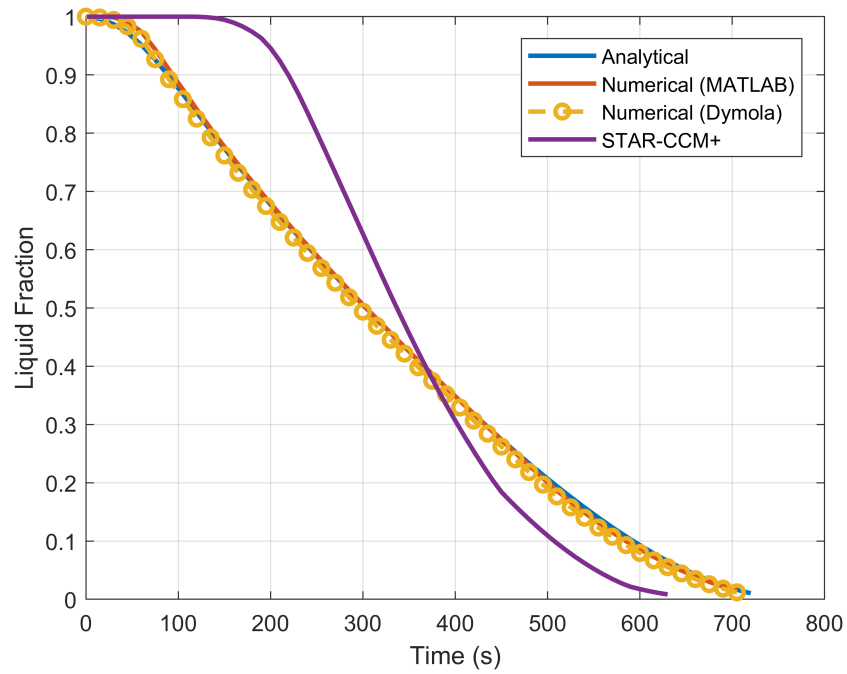
The difference between the rates of melting and solidification for pure conduction models depends on the temperature difference between the HTF and the PCM's melting point. During the charging cycle, this difference is 23.6°C, whereas for the solidification cycle, it is 17.4°C. The effect of this disparity is evident in the liquid fraction profiles as well as the temperature profiles, wherein the melting full melt is achieved faster than full solidification in a pure conduction model. Ignoring the analytical model, temperature profiles taken at probe F2, for the numerical models and the CFD simulation are presented in Fig. 4.6.

### 4.4 Case Studies

As a preliminary assessment of the developed models, various case studies are conducted by changing a few critical parameters of the 2D models, which include the PCM's

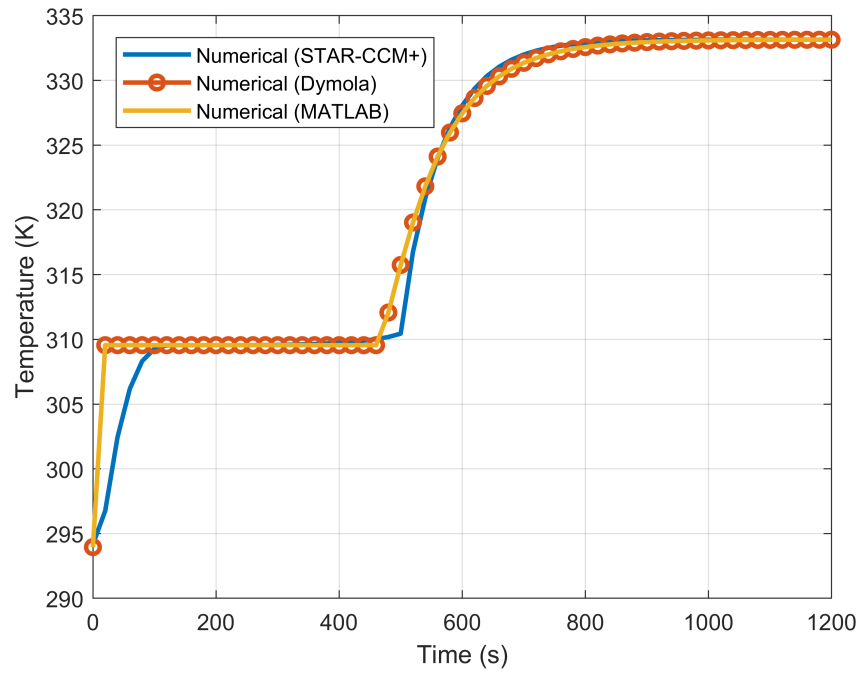


(a)

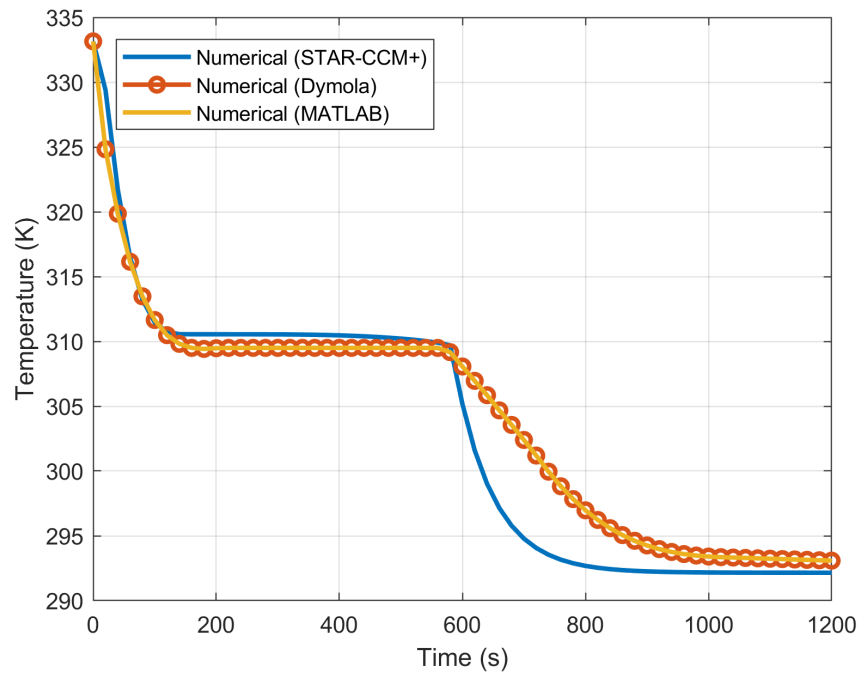


(b)

Figure 4.5: Liquid fraction profiles during melting and solidification



(a) Temperature profiles during melting



(b) Temperature profiles during solidification

Figure 4.6: Temperature profile comparison of 2D numerical and CFD models based on pure conduction

thickness, PCM's thermal conductivity, PCM's latent heat of fusion, tube material's thermal conductivity, and HTF's flow rate. The time to melt 99.9% of PCM was chosen as the parameter that was used to compare the results from all the developed models and the CFD simulation. As the finned tube design was of prime interest to this study, the case studies were only run for that design. The effective thermal conductivity of the PCM enhanced by the presence of the fins is accounted for all the case studies except one. The case studies that were conducted are described as follows.

As mentioned earlier, the models were primarily developed by assuming pure conduction in the solid as well as the liquid phase. The convective heat transfer coefficient is account for by acquiring a secondary effective thermal conductivity that is applied only in the liquid phase. However, as the acquisition of those coefficients was not possible before running the experiments, these first set of case studies focus only on pure conduction. In later chapters, the effect of natural convection is also studies.

#### **4.4.1 Case Study 1: Varying PCM Thickness**

The PCM thickness corresponds to the mass of the PCM and is therefore a measure of the storage capacity of a TES. In this study, the PCM thickness is varied from 0.125" to 1". Using the HTF flow conditions provided in Table 4.3, and the initial temperature of the entire domain at 21°C, the time to melt the PCM to a liquid fraction of 99% is calculated. As expected, the time to full melt increases with an increase in PCM thickness. This is shown in Fig. 4.7 provided below. There is good agreement between the developed analytical and numerical models, as well as the CFD code. This provides the confidence that developed codes can model pure conduction heat transfer with adequate accuracy.

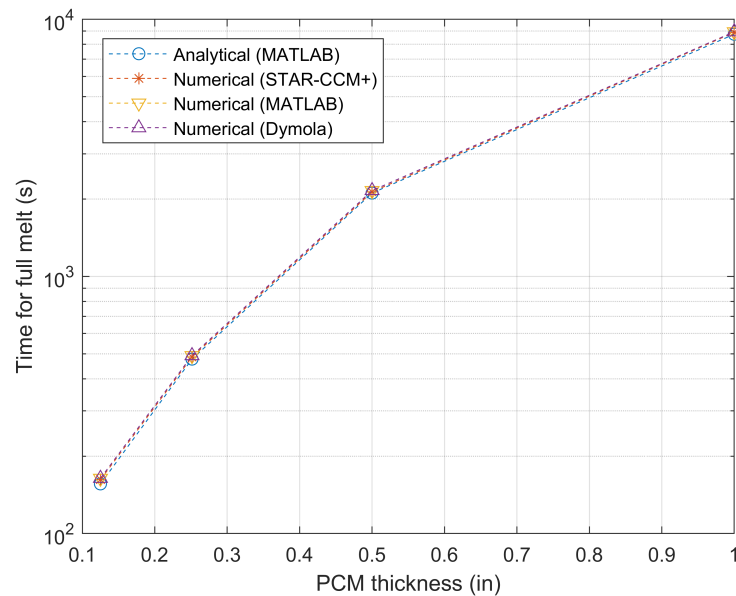


Figure 4.7: Effect of varying PCM's thickness on melt time

#### 4.4.2 Case Study 2: Varying PCM Thermal Conductivity

The PCM thermal conductivity is the limiting parameter that determines the charge and discharge rate of the LH-TES. Higher thermal conductivity, higher the heat transfer rate, thereby reducing the overall time to melt. The effects of increasing the thermal conductivity of the PCM is presented below in Fig. 4.8. It is evident that an initial increment in thermal conductivity definitely reduces the time to melt, however, it begins to plateau after about 10 W/m-K. This is because the heat that can be absorbed into the PCM is independent of the PCM's negligible thermal resistance, and is limited by the HTF's convective heat transfer coefficient, the tube's thermal conductivity and the driving temperature difference between the HTF and the PCM's melting point. Therefore, enhancements to the thermal conductivities of PCM should be made carefully by taking into consideration the temperature HTF that deposits or removes heat from the PCM, and the corresponding temperature difference between its temperature and the melting point of the PCM.

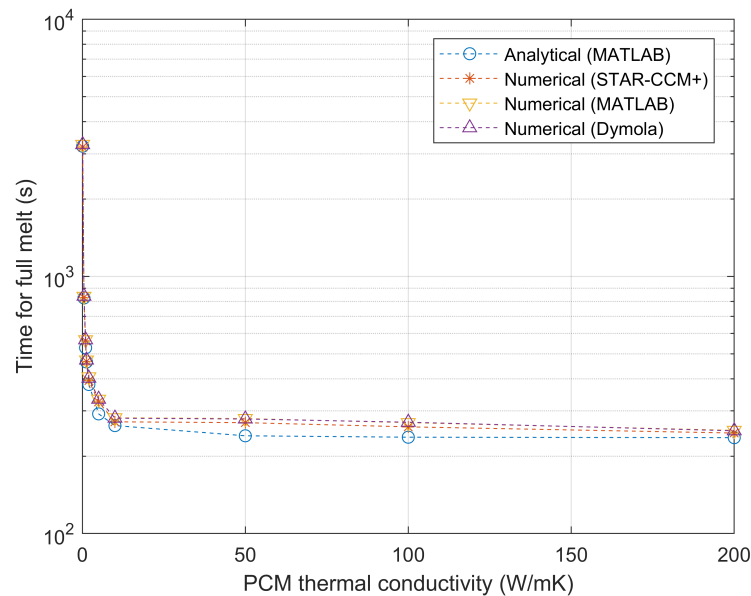


Figure 4.8: Effect of varying PCM's thermal conductivity on melt time

#### 4.4.3 Case Study 3: Varying PCM Latent Heat of Fusion

The enthalpy of fusion is a parameter that determines the amount of latent heat that can be stored in a LH-TES system. High latent heat of fusion is attractive as it allows the storage of more energy per unit volume. This case study varies the latent heat of the PCM over the range that is described in [31]. The effect of varying the PCM's latent heat on the final melt time is shown in Fig. 4.9.

#### 4.4.4 Case Study 4: Varying Initial Temperature of PCM

The initial PCM temperature will determine how much sensible heat is required to bring it up to its melt point. This parameter is of interest while comparing the analytical models to the numerical ones as the analytical model has only been setup to account for the thermal mass of the PCM and not the tube and/or fins. This leads to slight discrepancies in the final melt time, but based on the results for this study, the difference is deemed to be acceptable. The effect of initial temperature on final melt time is plotted

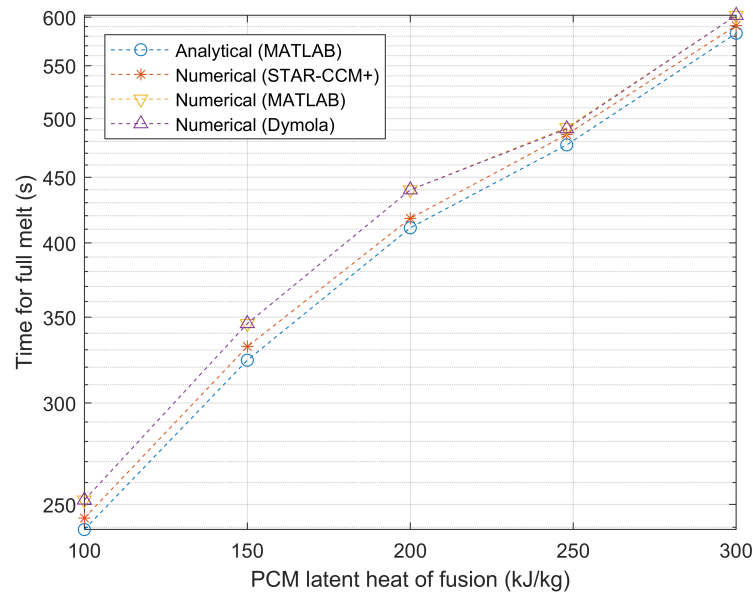


Figure 4.9: Effect of varying PCM's latent heat of fusion on melt time

in Fig. 4.10 below. The temperatures were varied from  $0^{\circ}\text{C}$ , up to  $1^{\circ}\text{C}$  below the melting point.

Based on the case studies presented herein, the following conclusions can be drawn.

- As expected, the analytical model under-predicts the total melt time of the PCM as it doesn't account for sensible heating in HTF or the tube wall.
- The developed models over-predict the total melt times in most cases, with the Dymola-based model being closer to the CFD results in comparison to the MATLAB-based model.
- All four models are in good agreement with each other, with the maximum percent difference being less than 10%.

It is clear that the analytical model is very robust in characterizing the thermal performance of a LH-TES system where the only mode of heat transfer in the PCM is conduction. Similarly, the developed models agree well with a robust commercial CFD

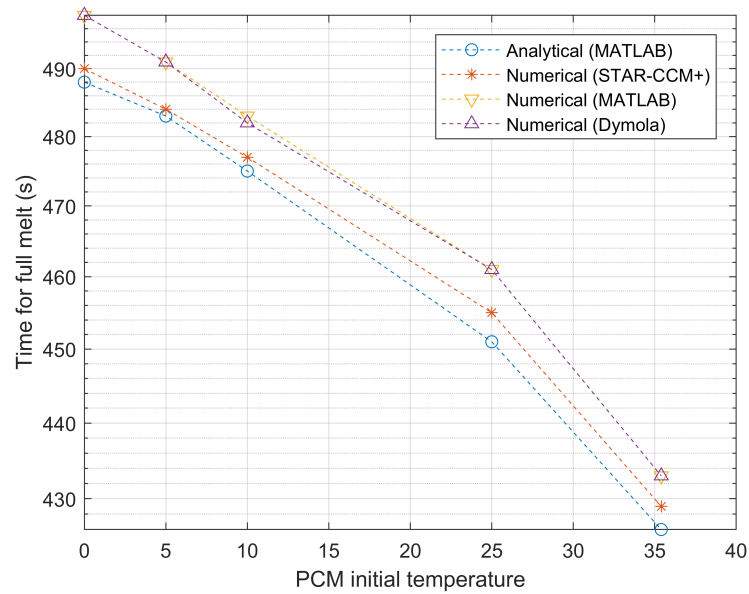


Figure 4.10: Effect of varying PCM's initial temperature on melt time

tool for the cases presented herein. This of course is an idealized case wherein only conduction is assumed. To account for effects of natural convection, experiments are run on the bench scale setup and the coefficients for the Rayleigh expression are acquired. The experimental methodology is described as follows.

## CHAPTER 5

### Design and Analysis of Experimental Facility

#### 5.1 Experimental Apparatus

The experimental apparatus for the finned and unfinned designs is exactly the same except for the main test section, which the thermal battery that stores the heat. The test apparatus was designed to measure temperature of the PCM, and the temperature and flow rate of the HTF adequately, based on which, the heat transfer rates were calculated and compared with the developed models and CFD simulations. A schematic of the experimental setup is in Fig. 5.1.

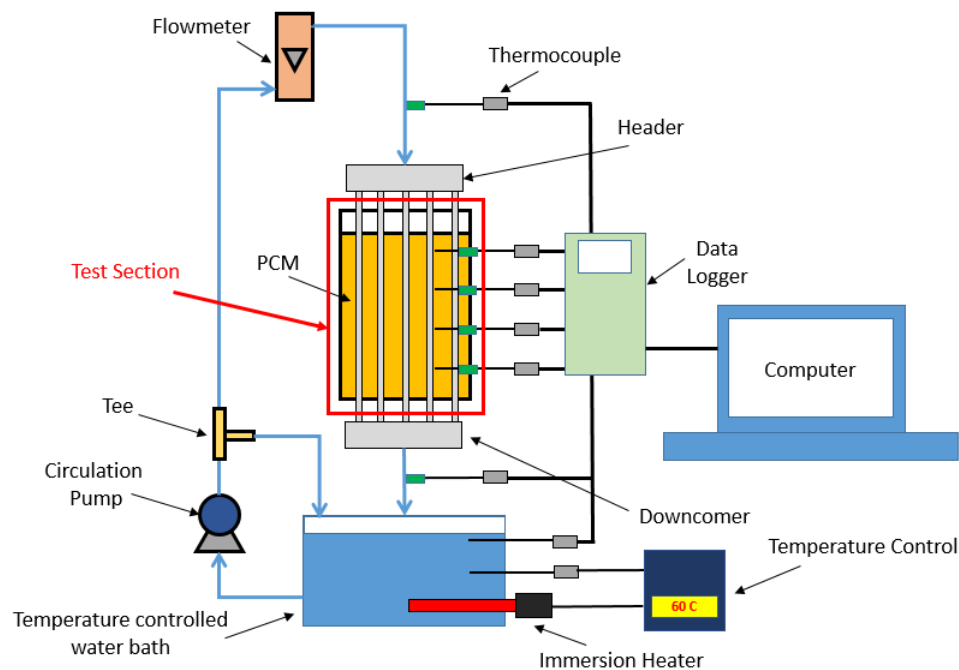


Figure 5.1: Schematic of the experimental apparatus

During the charging cycle, hot water from the temperature controlled bath is circulated through the loop using a centrifugal pump, which then passes through the tubes of the test section and melts the PCM. Conversely, during the discharge cycle, cold water from

another bath is circulated through the same loop, which absorbs the heat from the PCM and solidifies it. In order to ensure that the cold water does not heat up during the discharge cycle, fresh cold water is drawn from a water inlet and placed into the cold water bath, and the outlet from the downcomer is drained down a sink. The experimental apparatus can be subdivided into various sections. These are described as follows.

### 5.1.1 Thermal Battery Test Section

The LH-TES battery that stores the PCM is mounted on a test stand with the help of a base-plate. The main components of the LH-TES battery include the test section, the downcomer, and the end cap. A CAD representation of the exploded view of the test section, along with the downcomer, the base-plate and the end cap is shown in Fig. 5.2.

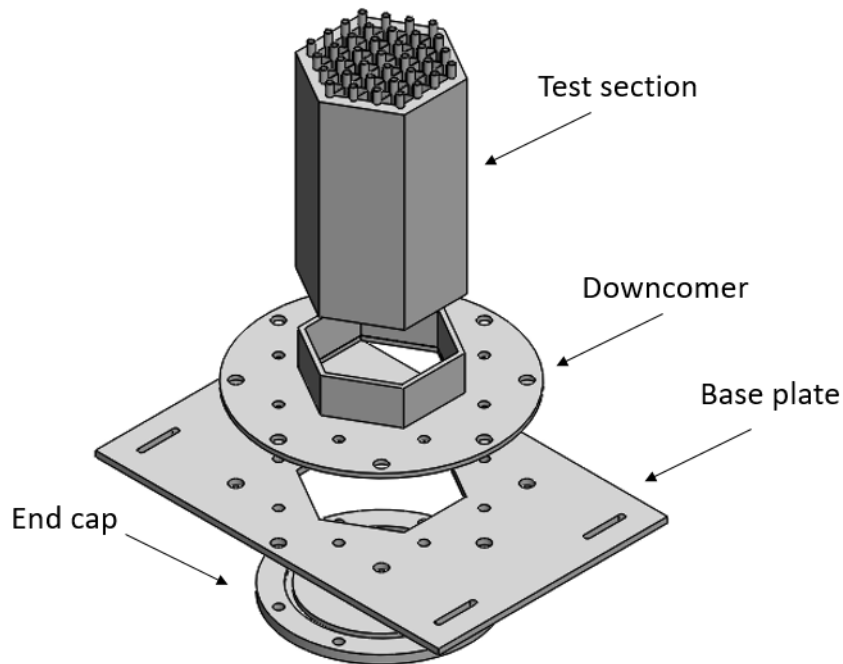


Figure 5.2: CAD representation exploded view of test section, with the base plate and bottom end cap

As described earlier, two test sections, namely, a finned and an unfinned design were

manufactured - one by welding individual machined parts, the other by metal 3D printing. Figure 5.3 shows a top-view of the actual bench-scale test sections. As the goal of this work is primarily to develop a validated model, the experimental setup was kept small, without too much focus on scaling the design, though this would be crucial for the lab-scale experimental setup that will be constructed based on the experience acquired from this study.

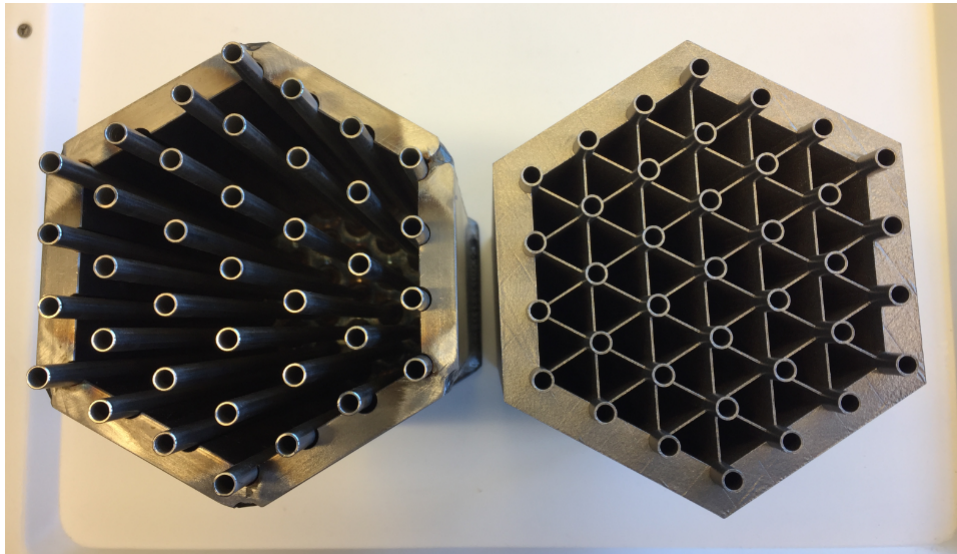


Figure 5.3: Top view of finned and unfinned thermal battery test sections

The body of the test sections is 20.32 cm (8 inches) tall and 11.43 cm (4.5 inches) wide. The tubes at the top extend another 1.27 cm (0.5 inches), and the end cap at the bottom is 0.953 cm (0.375 inches) thick, bringing the total height of the manufacture test sections to 8.875 inches. The wall thickness is 1.02 cm (0.4 inches) for both the designs to maintain similarity, but it was mainly to provide adequate structural integrity for the 3D printed design. Another reason the wall is of a certain thickness is to provide enough thread length for Swagelok fittings to be screwed into them. These bore-through Swagelok fittings allow thermocouples to pass through them and into the PCM domain, while providing a tight seal to prevent leakage. There are a total of 10 Swagelok fittings - 5 along the vertical wall and 5 on the bottom surface. Section 5.1.2 provides more

information regarding the thermocouples and the Swagelok fittings used.

Although the designs are currently being tested for PCMs with a low melting point temperature, it is envisioned that high melting point temperature PCMs, such as molten salts, will also be tested in near future. The design was also built with the intent to operate with steam as the heat transfer fluid. Taking these requirements into consideration, a decision was made to weld the downcomer to the bottom of the TES battery, thereby creating a tight seal and allowing for a pool of condensate to form.

A base-plate holds the downcomer and attaches it to the test stand. The opening at the bottom of the downcomer is then closed with an end cap containing a groove for an O-ring to provide a tight seal. This end cap has a set of 5 Swagelok fittings that align perfectly with those on the bottom of the test section. This ensures that the thermocouples that slide in and out the test section are held upright and parallel to the tubes. Figure 5.4 shows the end cap along with an O-ring that is used to provide a tight seal between the end cap and the downcomer. The smaller holes are for the Swagelok fittings whereas the the larger hole is connected to the outlet which removes the HTF from the test section. The base-plate that connects the test section to the stand is shown in Fig. 5.5.

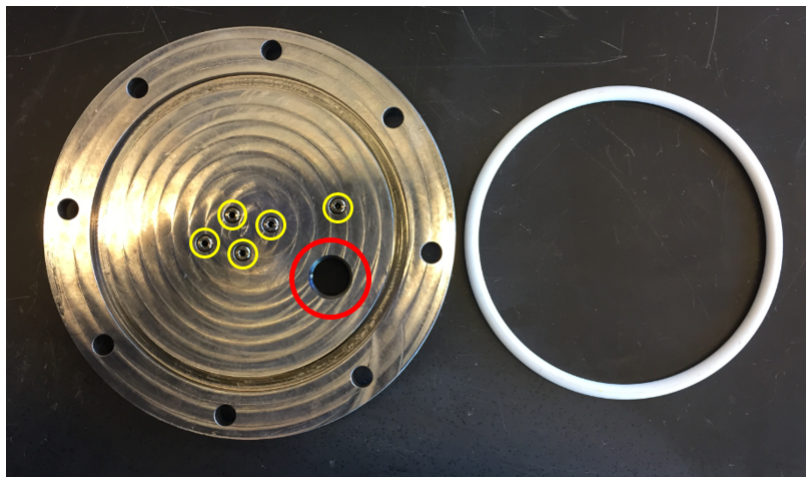


Figure 5.4: Top view of end cap with Swagelok fittings & HTF return highlighted in yellow and red, respectively, alongside the PTFE O-ring

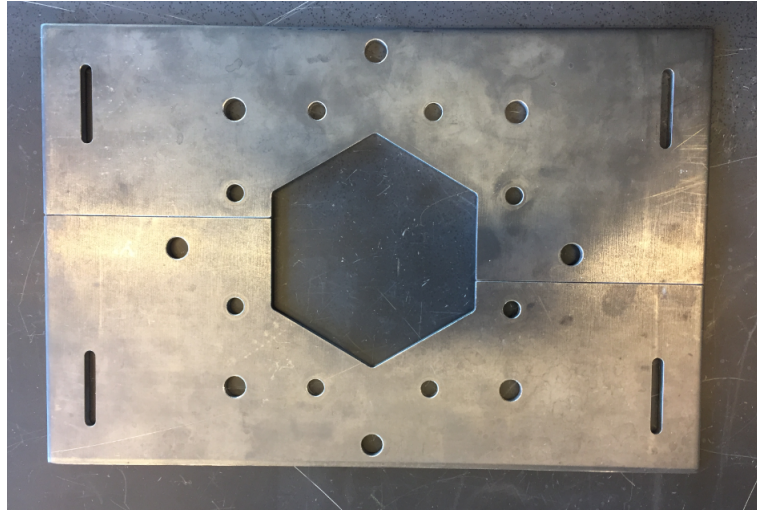


Figure 5.5: Top view of base-plate that holds the test section on the stand

### 5.1.2 Temperature sensors

The temperature data was acquired using multiple K-type thermocouples embedded in the PCM at different locations. These locations correspond to the probe points set up in the CFD models. In order to acquire temperature data within the PCM domain, thermocouples are inserted using bore-through Swagelok fittings. Holes were drilled and tapped on the vertical wall of the test section to allow the insertion of thermocouples near the inner side of the wall. Similarly, to acquire temperatures near the inner tubes, holes were drilled and tapped on the bottom surface of the thermal batteries (see Fig. 5.6 and Fig. 5.7). In order to avoid significant interference of the presence of data acquisition instruments on heat transfer phenomenon, the thermocouples inserted around the tubes were  $1/16^{th}$  inch in diameter, whereas those near the wall, which would not affect the flow phenomenon significantly were  $1/8^{th}$  inch in diameter.

As mentioned earlier, at a given moment, only 10 thermocouples can be inserted in the test section, namely, 5 through the side wall and the rest through the bottom. To account for the remaining 4 points of data acquisition, the thermocouples around

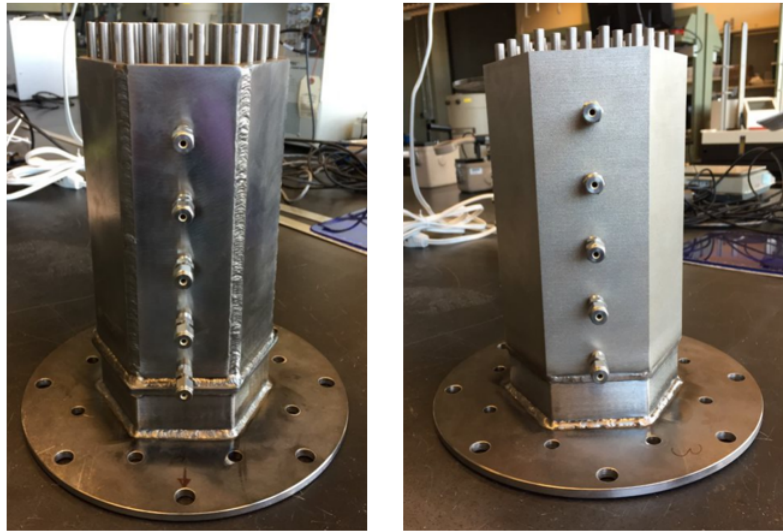


Figure 5.6: Side-wall Swagelok fittings to hold thermocouples for measuring PCM temperatures near the outer wall

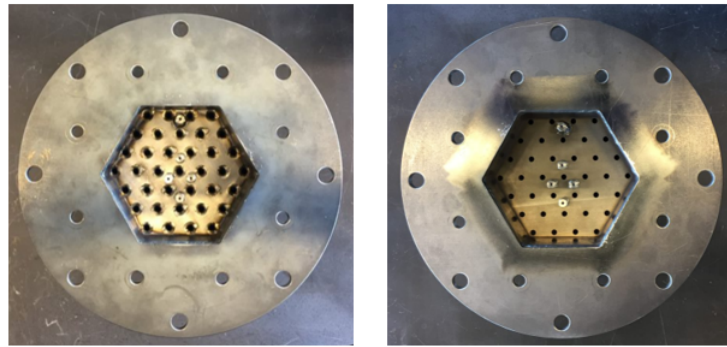
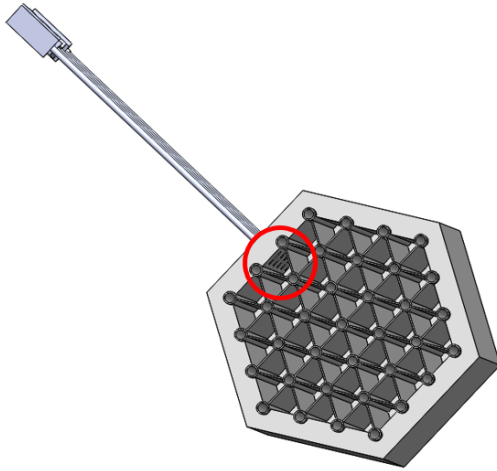


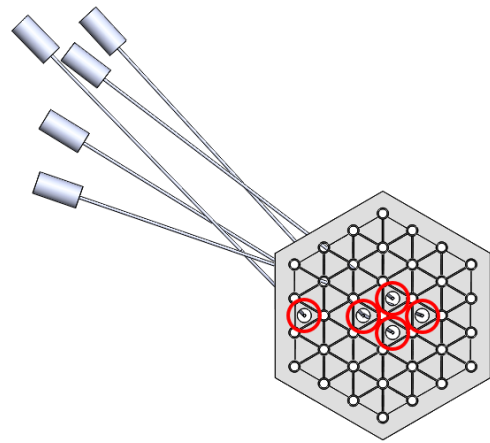
Figure 5.7: Bottom-wall Swagelok fittings to hold thermocouples for measuring PCM temperatures near the inner tubes

the tube are lowered once the PCM has solidified. This is carefully done to ensure the thermocouples don't bend within the test section, thereby potentially resulting in a mismatch between the locations of the thermocouple tip in the experiments and that of the point probes in the simulations. If this were to occur, there would be an error in temperature data being recorded and compared. The thermocouple locations are highlighted in the CAD representation shown in Fig. 5.8 and also in the unfinned test

section show in Fig. 5.9.



(a)  $1/8^{th}$  inch wall thermocouples

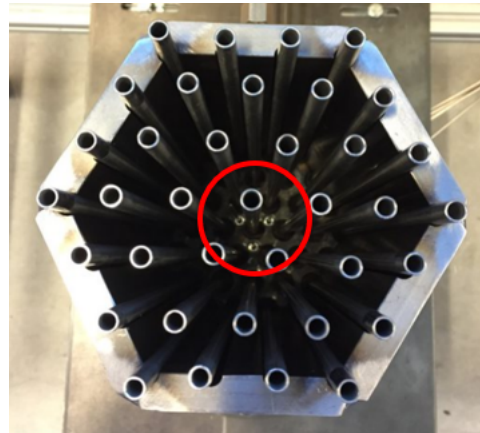


(b)  $1/16^{th}$  inch internal thermocouples

Figure 5.8: CAD view of thermocouple locations in the test section



(a)  $1/8^{th}$  inch wall thermocouples



(b)  $1/16^{th}$  inch internal thermocouples

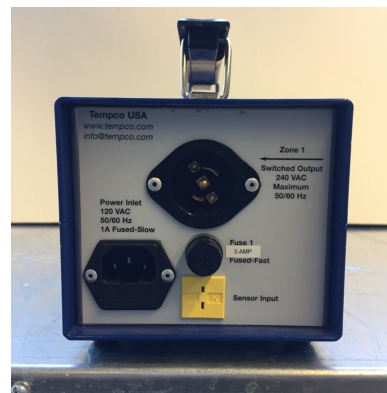
Figure 5.9: Thermocouple locations in the unfinned test section

### 5.1.3 Heat Transfer Fluid Loop

A water bath heated using a 1500W immersion heater, is maintained at a set-point temperature using a Tempco TPC-1000 temperature control console. The console also has a port for a K-type thermocouple which communicates the temperature of the water, thereby allowing the controller to maintain a steady temperature throughout the experimental run (see Fig. 5.10).



(a) Front panel of Tempco controller



(b) Connection ports on Tempco controller

Figure 5.10: Tempco temperature controller used for maintaining hot water bath temperature

During the charging cycle, hot water from the bath is circulated through the loop using a centrifugal pump. The flow rate is measured by a variable area flow meter, capable of measuring high temperature water flow with an accuracy of  $\pm 2\%$ . This particular model was chosen due to its temperature rating, its inline operating capability, and its independence on mounting orientation (see Fig. 5.11).

The water then flows through a header that distributes the water to the 37 tubes of the test section. The header has a baffle that breaks the incoming jet of water from the tube and distributes the flow more evenly. After flowing through the tubes, the water is then collected in a downcomer, which then returns the fluid back to the heated water bath for re-circulation. All of the components – the pump, flow meter, header,



Figure 5.11: Variable area flowmeter for water

and downcomer – are connected with a neoprene tubing, rated up to 260°F. The header design was crucial to this experiment as equal flow through the tubes is needed to allow the model simplification presented in Chapter 3. Therefore, the header was designed carefully using CFD analysis. This is explained in the following section.

### 5.1.3.1 Header-Baffle Design

As it is obvious that the HTF flowing through the tube and entering the header would cause most of the fluid to flow through the central tubes, it was necessary to design a baffle that would diffuse the fluid channel, and distribute the flow evenly through the tubes of the test section. The header is composed of three parts, the upper connector which connects the inlet to the header, the baffle that diffuses the flow of the HTF, and the bottom connector which connects the header to the tubes of the test section. These three parts are shown in Fig. 5.12.

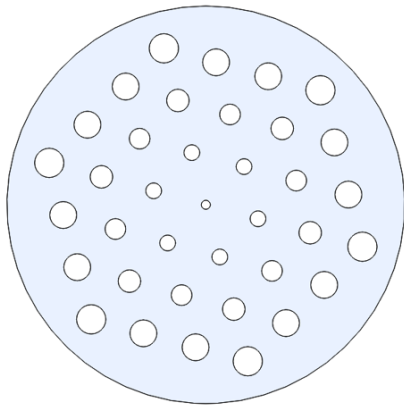
To guide the tubes into the header, the bottom connector of it was made out of SS316 with chamfered holes. This was necessary mainly for the unfinned design as welding the tubes to its bottom surface warped it, causing the the tubes to misalign. The top connector was also made out of SS316, whereas the baffle was 3D printed out of ABS plastic to allow the testing of various designs. This material is suitable for this experiment as its maximum operating temperature is 105°C, above which it begins to soften. Some



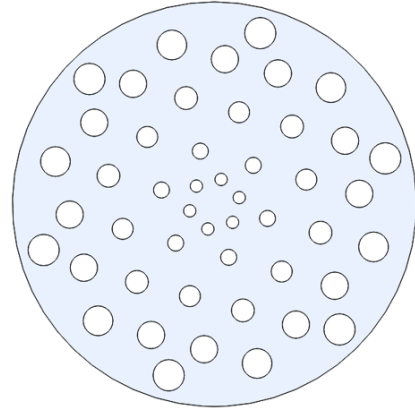
Figure 5.12: Header components - top connector, baffle, and bottom connector

of the preliminary baffle designs led to no flow in the outer tubes, as observed during preliminary runs, so the designs has to be modified. It should be noted that in the current experimental set up, there is no way to accurately measure the flow rate in each of the tubes, therefore, the results from a few CFD studies were assumed to be satisfactory. To ensure that the flow through each of the tubes is equal, surface average velocities were acquired at the exit of each of the header bottom's holes using CFD models, and the baffle design was optimized to provide a more even flow-field. Some of the baffle designs during this evolutionary optimization process are shown in Fig. 5.13.

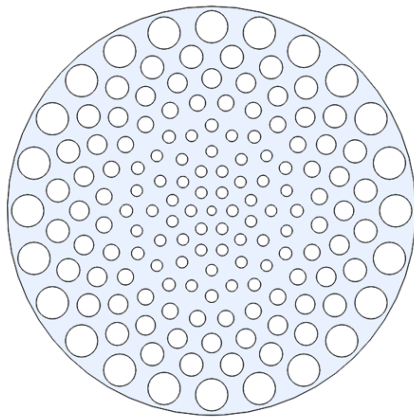
It is important that the water entering the header flows through the tubes only, and doesn't leak around them into the PCM. This was prevented by using silicone gasket caulk and ring gaskets to seal the small gaps between the tubes and the bottom connector, resulting from the machining tolerances. The silicone material was applied using a tube with a nozzle and was allowed to dry overnight. The gasket rings placed on top of the silicone were punched with an inner diameter of  $1/16^{th}$  inches and an outer diameter of  $1/2$  inch (see Fig. 5.14). This allowed them to be placed adjacent to each other without



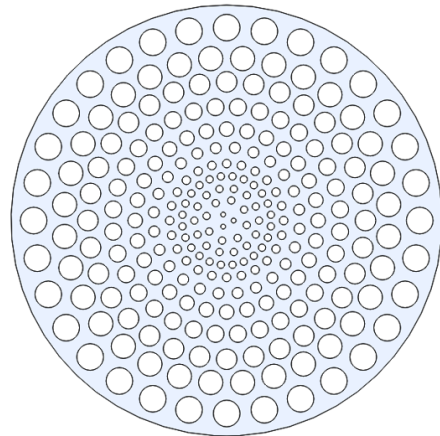
(a) Design 1



(b) Design 2



(c) Design 3



(d) Final Design

Figure 5.13: Evolution of baffle design to diffuse HTF flow

overlap. Once the bottom connector is slid on to the test section, the ring gaskets are placed around the tube as shown in Fig. 5.15



Figure 5.14: Ring gaskets used to create a tight seal around the test section tubes

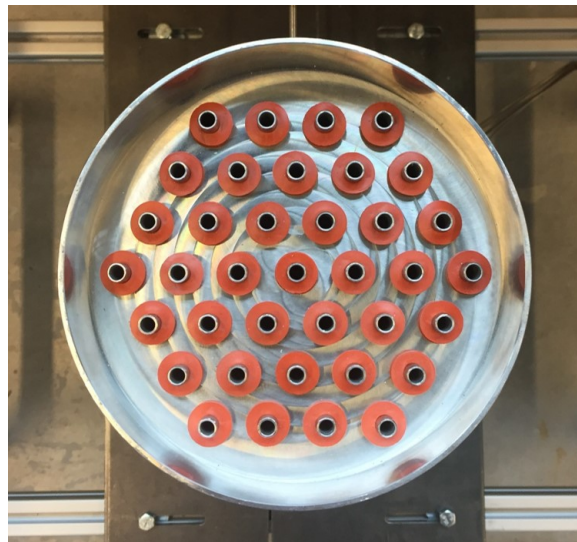


Figure 5.15: Ring gasket arrangement in the bottom connector of the header

#### 5.1.4 Data Acquisition

A 16-channel National Instruments NI-9213 temperature input module and a NI cDAQ-9178 chassis are used for temperature data acquisition (see Fig. 5.16). The cDAQ is then connected to a laptop that reads the temperature data of 14 thermocouples, using a data acquisition software called LabView. Ten thermocouples correspond to the test section, two measure the HTF inlet and outlet temperatures, one measures the temperature of

the water bath and one measures the ambient temperature. The LabView model collects temperature data from all of the thermocouples, and writes it continuously to an excel sheet.



(a) NI-9213 Module



(b) cDAQ-9178

Figure 5.16: National Instruments Data Acquisition equipment

## 5.2 Experimental Procedure

As multiple experimental runs with different test sections are to be made over the course of this study, a predefined experimental procedure was followed. This ensured the similarity in the data collected over various experimental runs, and allowed for a better quantitative comparison. For both the test sections, the experimental procedure is as follows:

### 5.2.1 Preparing Test Section

- Connect the Swagelok fittings to the test section, and insert the thermocouples through their bore through holes to ensure the tips lie at appropriate locations for data collection. Tighten the Swagelok fittings adequately to prevent PCM leakage.

This step is crucial and needs to be done before the PCM is poured into the test section.

- Melt the PCM in a beaker using a hot plate and then pour it using a funnel, the narrow end of which is connected to a tube. This allows easy, streamlined pouring of the PCM into the test section resulting in very little to no air cavities. Use a thin dipstick as a level indicator to measure the depth of the PCM. Do this step in stages to ensure that the PCM is tightly packed when solidified, and that the final solidified depth is equal to the value used in the simulations.
- Connect the header to the test section and place the gasket rings around each tube to provide a tight seal. Place the baffle and the top header connector piece, and clamp the three components using C-clamps.
- Connect the header inlet and the downcomer outlet to the circulatory loop.

### 5.2.2 Preparing HTF Loop

- Ensuring that both the flow valves are open and that the water is at room temperature, run the pump to circulate the water and remove any air bubbles from the loop. Adjust the valves to get the set flowrate for the experimental run. Do this by keeping the primary loop valve 100% open and controlling the opening on the circulatory valve. Once the required flowrate is acquired, turn off the pump and then close the primary valve only. This will prevent any adjustments to flowrates in the test loop once the experiment has begun.
- Heat the water bath to the set-point temperature of 60C using the Tempco temperature control. Turn on the pump to circulate the water within the circulatory loop and bring the water bath to the set-point temperature. Let the bath stay at the

set-point temperature for about 10 minutes to ensure thermal equilibrium. Start collecting data using LabView.

- It should be noted that as the primary loop valve is closed, there is still a section of the primary loop that has cold water, which will affect the water bath temperature once the charging cycle is commenced. To overcome this, the water bath temperature is kept at 12°C higher than the final set-point temperature for the experimental run. Although this leads to an initial spike in the inlet water temperature, the system equilibrates thermally in under 2 minutes and the set-point temperature is then brought to its value of interest.

### 5.2.3 Charging the LH-TES

- Turn off the pump, open the valve to the primary test loop and then turn on the pump again. This will cause the water to flow through the primary loop at the set flowrate. The temperature of the bath will drop slightly as the cooler water is pushed out of the primary loop into the bath, however, the temperature controller will sense this change, thereby turning on the heating element and heating the water bath until the temperature reaches the set-point.
- Ensure there are no leaks, either in the test section or the HTF circulatory loop.
- Collect temperature data for 45 minutes. This completes the charging cycle.

### 5.2.4 Discharging the LH-TES

- Turn off the circulatory pump, and close the ends of the tubes with the end caps.
- Transfer the primary tube connecting the water bath to the pump, and the secondary tube of the circulatory loop into the cold water bath. Place the tertiary tube from the downcomer in the sink.

- Insert the cold water bath refill tube into the bucket, remove all of the tube end caps and turn on the circulatory pump. This will cause the cold water to flow from the cold water bath, through the test section, and out into the sink.
- Run the discharging cycle until the PCM reaches about 25°C. Below this point, the PCM is completely solidified and the temperature difference between the PCM and the HTF is very low to cause any significant heat transfer.
- Turn off the circulatory pump, and let the system come to room temperature overnight. This completes the discharging cycle.

The test sections filled with PCM are shown in Fig. 5.17, and the experimental apparatus mounted on the test stand is shown in Fig. 5.18.

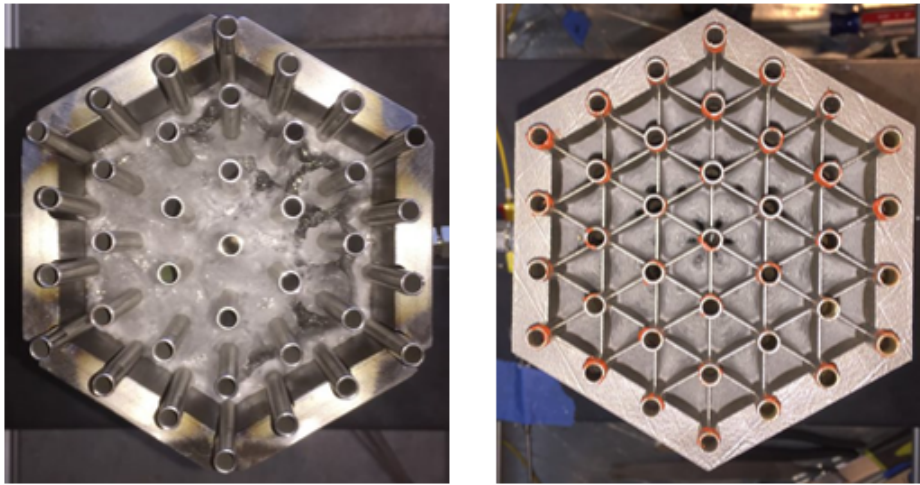


Figure 5.17: Top-view of test sections filled with PCM

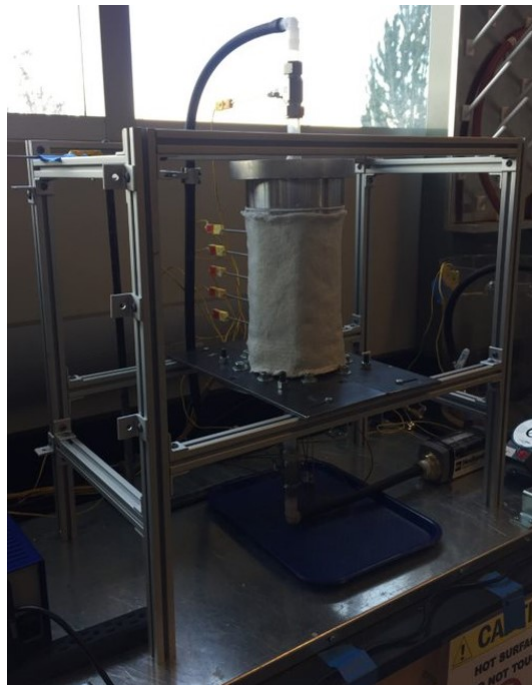


Figure 5.18: Experimental setup with insulated test section

## CHAPTER 6

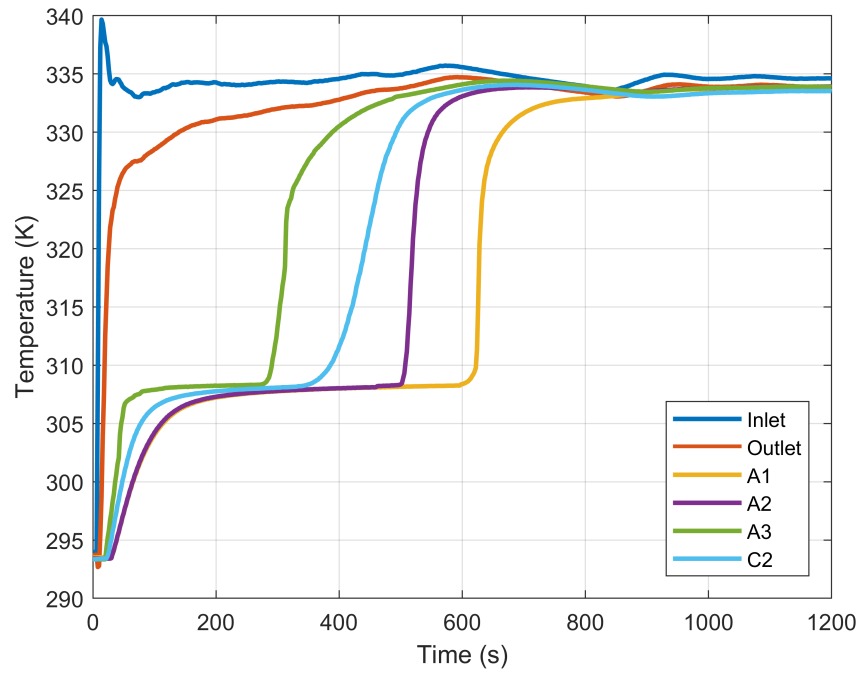
### Experimental Results, Discussion, and Comparison

This chapter primarily focuses on the results from the experiments that were carried out using the finned bench-scale LH-TES systems. The acquired data is used to estimate the coefficients  $C$  and  $n$  from equation 3.11, thereby allowing the calculation for an apparent thermal conductivity. This apparent thermal conductivity is used within the liquid domain to capture the effects of natural convection during the melting cycle. Once this apparent thermal conductivity is implemented in the models, their performance is quantified again to perform model validation. This is conducted for the numerical models as well as the CFD simulations. This chapter covers the charging and the discharging cycle behavior, the acquisition of the apparent thermal conductivity coefficients, performs validation of the models used in this study, and analyzes the effects of natural convection on heat transfer enhancement.

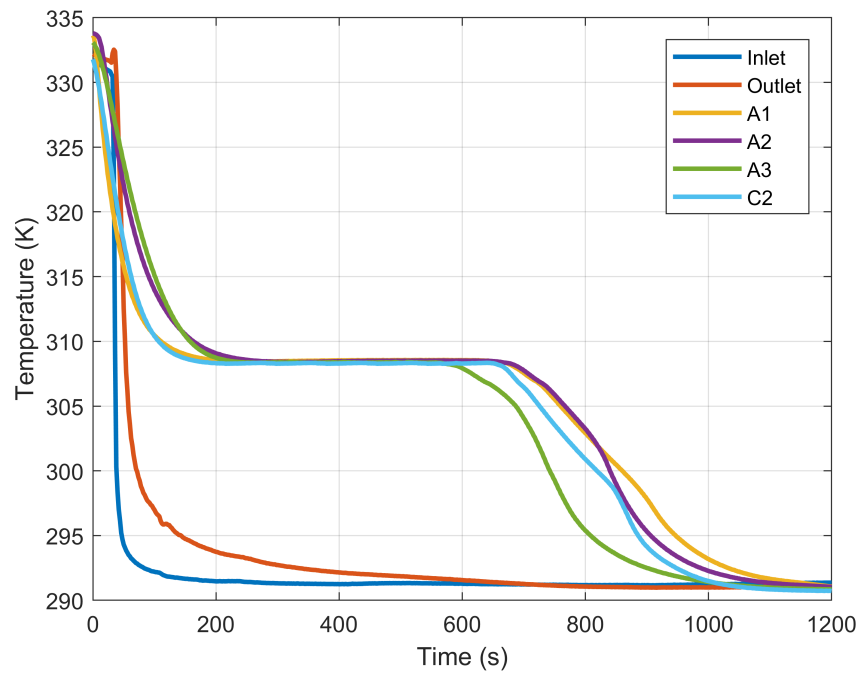
#### 6.1 Thermal Hydraulic Performance of Finned Design

Experiments run with and without insulating the test section showed no observable differences for the operating conditions that were tested. Therefore, only the results for the un-insulated test section are presented hereon. Also, the temperature data acquired from TCs near the inner PCM domain is focused on for the most part. This is primarily to allow better comparison between the 2D numerical models and the experimental results, as well as for visualization purposes. The raw experimental temperature data acquired during the melting and solidification cycle, with HTF inlet conditions as provided in Table 4.3 is shown in Fig. 6.1.

There is an initial spike in the inlet temperature during the melting cycle, which eventually equilibrates to the set-point temperature. This equilibrium point is reached at about 30 seconds, after which, the temperature remains within  $\pm 1.5^\circ\text{C}$  of the set-point



(a) PCM inner domain temperatures during melting



(b) PCM inner domain temperatures during solidification

Figure 6.1: Temperature profiles during melting and solidification cycles for finned tube design

value of 60°C. As expected, the difference between the inlet and the outlet temperatures decreases as time passes on. This is due to the drop in driving temperature difference between the HTF and the PCM, as well as the increase in thermal resistance due to the molten PCM.

Upon comparing the temperature profiles for probes A2 and C2, it can be seen that during melting, C2 reaches full melt faster than A2, even when they are positioned at the same distance from the bottom surface of the test section. This can be attributed to the fact that the tubes in contact with the wall, also close to the probe C2, have a larger contact surface area when compared to the fins surrounding probe A2. Larger contact surface area would increase the heat transfer rate, and when further enhanced by natural convection, would lead to faster melt times. In comparison, the solidification plots for A2 and C2 line up quite well. This suggests that the solidification front travels much like a vertical wall instead of the curved melt front that is observed during melting. This hypothesis is also supported by the fact that the probes A1 and A3 have the same solidification temperature profiles, even when they are separated vertically by a distance of 12.7 cm (5 inches).

The wall temperature profiles for melting and solidification are shown in Fig. 6.2. It can be seen from the temperature profiles in Fig. 6.2a and Fig. 6.2b that melting and solidification occurs very rapidly near the wall. This is expected as the wall is the surface the deposits and absorbs the heat from the PCM. The most crucial thing that is observed from Fig. 6.1a and Fig. 6.1b is that the phase change temperatures are slightly lower than what is presented in literature (also tabulated in Table 2.2). The observed melting temperature based on multiple experimental runs is estimated to be 34.9°C, whereas the solidification temperature is 35.3°C. This might be due to several reasons, such as the purity of the PCM used or the existence of a mushy zone. Although pure, organic substances have a single phase change temperature, the rate of heating and cooling could

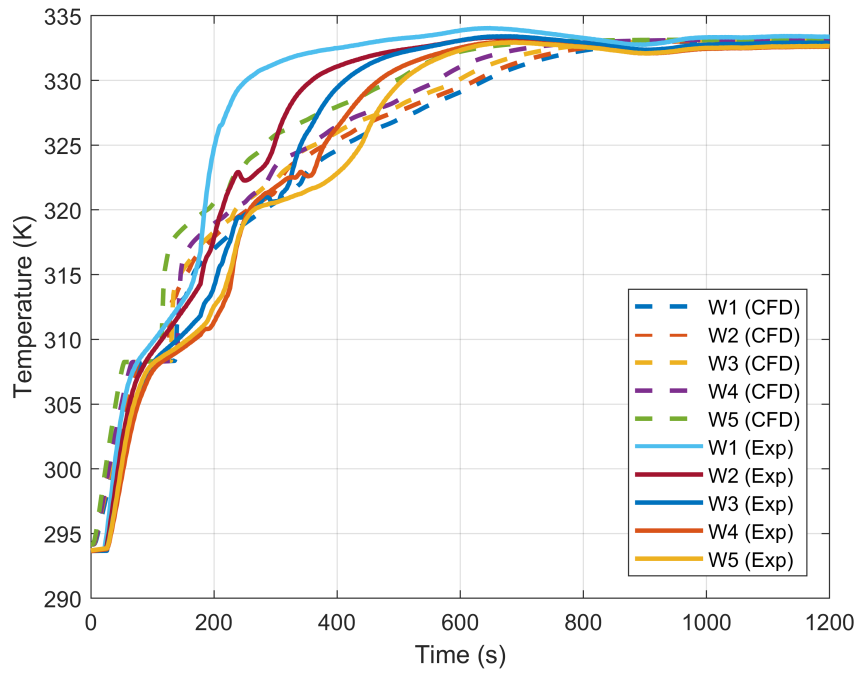
also affect the temperature at which phase change occurs [78]. Therefore, for the models to be more relevant, they are rerun with the phase change temperature being the average of the above mentioned temperatures. The updated results are presented hereafter.

### **6.1.1 Data Analysis for Finned Test Section**

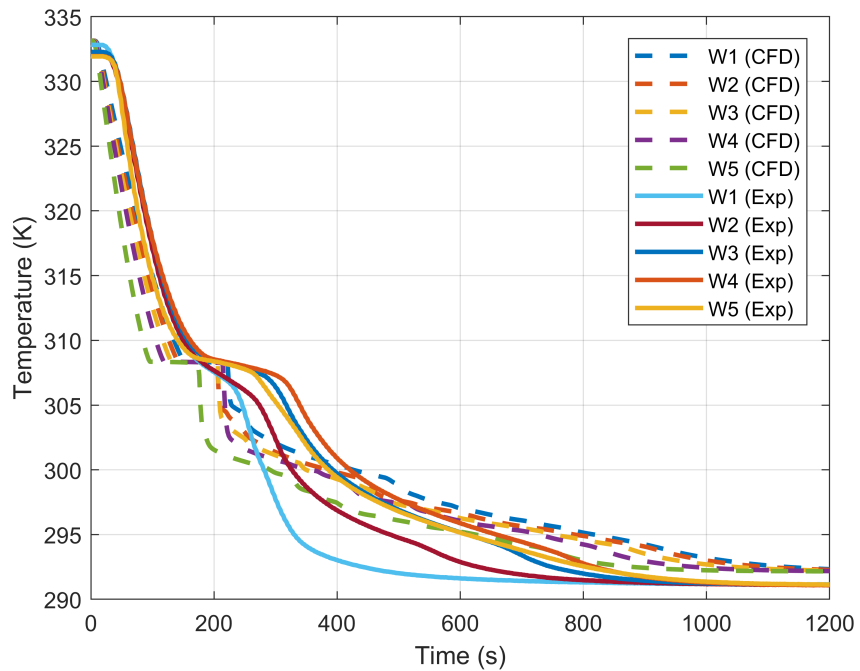
In order to compare the performance of the developed models and the CFD simulation, the experimental temperature data from probes C2 was compared to data at probe G2 from the MATLAB, Dymola and CFD models. Figure 6.3 shows the averaged experimental temperature profiles with its error bars, along with the results from the CFD and numerical models. It can be seen from Fig 6.3a that the initial sensible heat addition has decent agreement but the deviation in the temperature profiles begins once complete melt has been achieved. The sudden rise in temperature of the experimental probe can be attributed to the enhanced heat transfer that it would experience in the existence of a combined, conductive and convective heat transfer. Similar behavior is observed during solidification where the time to solidify is lower in the experiment when compared to the numerical and CFD models, indicating possible natural convection effects. In order to improve the accuracy of the models, natural convection needs to be accounted for in the liquid phase of the PCM. The following section describes how this requirement was met.

## **6.2 Analysis to Quantify Effects of Natural Convection**

The preliminary models were developed based on pure conduction, however, it has been well established that natural convection does play an important role in phase change. This is also evident from the temperature profiles during the melting cycles shown in Fig. 6.3. There are many ways to account for natural convection in the liquid phase, one of the prominent method being the Boussinesq approximation, wherein buoyancy-driven

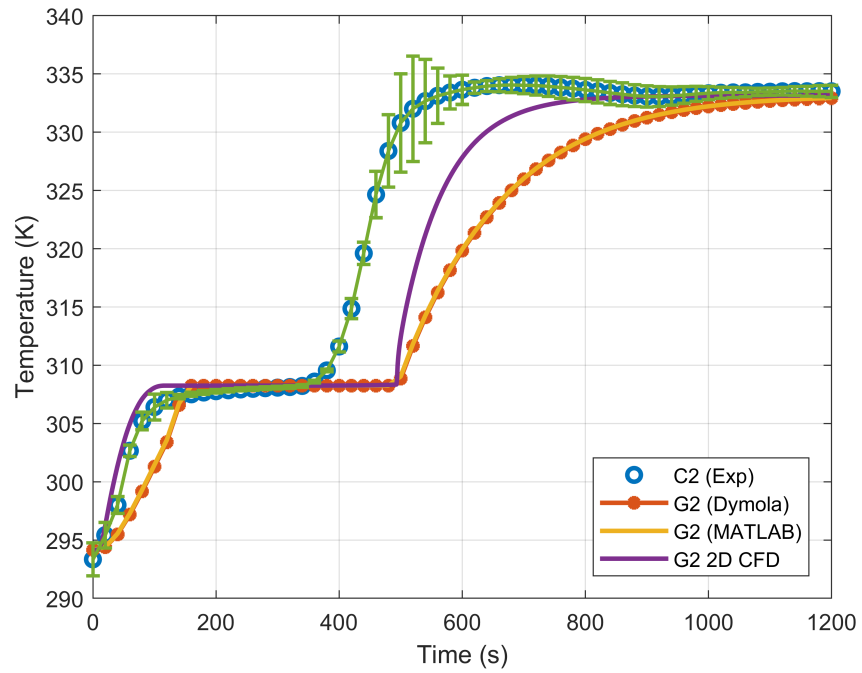


(a) Wall probe temperatures during melting

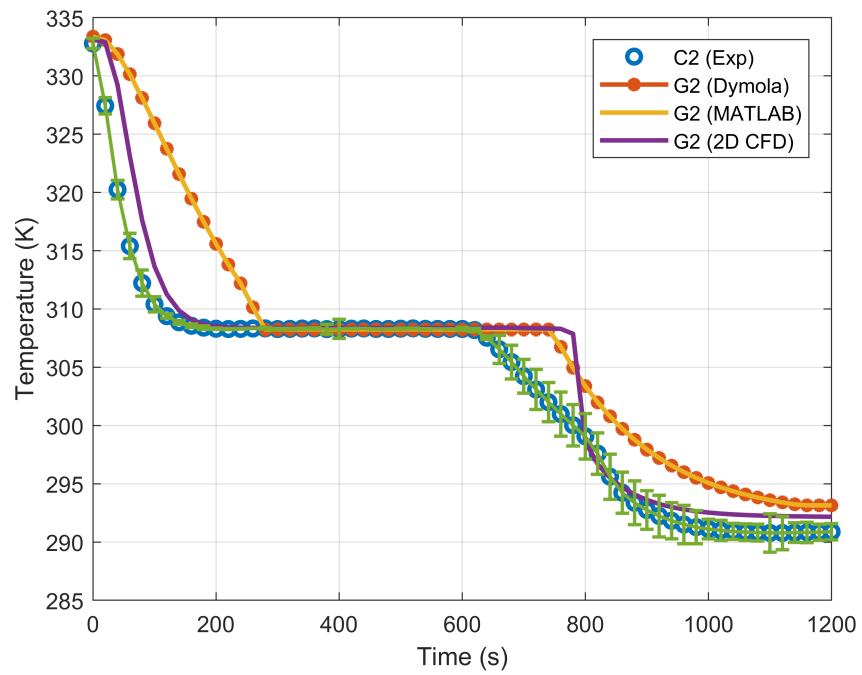


(b) Wall probe temperatures during solidification

Figure 6.2: Wall probe temperature profiles from CFD models and finned tube experiment



(a) Temperature profiles during melting



(b) Temperature profiles during solidification

Figure 6.3: Comparison of temperature profiles from numerical models, CFD simulation and finned tube experiment

flow is solved for using the momentum equation, by ignoring the changes in density of the fluid except in the body force term. This approach could have been taken for this study, however, it would have added another governing equation to the models. This additional governing equation would have slowed the simulation runtime, and therefore was ignored. Instead, empirical data is used to acquire an apparent thermal conductivity in the liquid domain to account for the effects of natural convection. The correlation expressed in equation 3.11 uses the Rayleigh number, calculated as a function of the width of the liquefied PCM. Although natural convection occurs only within the liquid domain of the PCM, and therefore the Rayleigh number would change with an increase in liquid fraction during melting, the modeling is simplified by assuming a maximum Rayleigh number based on the total width of the PCM domain. To acquire the constants  $C$  and  $n$  as shown in equation 3.11, a trial and error methodology was followed. With the help of CFD simulations, the values of the constants were varied to provide the best fit between the experimental data at probe C2 and CFD temperature profile at probe G2. Table 6.1 provides the information on the variations in values of  $C$  and  $n$ , its resulting apparent thermal conductivity using equation 3.11, and the corresponding enhanced thermal conductivity in the liquid domain of the PCM. The temperature profiles for these various case studies are also shown in Fig. 6.4. Case 7, with  $C$  and  $n$  values of 0.228 and 0.25 respectively, provide the best fit when compared to the experimental data.

It should be noted that the enhanced thermal conductivity already accounts for the presence of fins, as it is calculated by substituting the apparent thermal conductivity from equation 3.11 into the effective thermal conductivity. This results in an enhanced thermal conductivity of 2.49 W/mK, which is the value substituted for the liquid domains in the 2D numerical and CFD models. The resulting temperature profiles for melting and solidification are shown in Fig 6.5. Table 6.2 shows the maximum absolute errors between experimental and modeling temperature data for the effective and apparent

Table 6.1: Rayleigh correlation coefficient analysis fro apparent thermal conductivity

Case	C	n	Apparent Conductivity (W/mK)	Enhanced Conductivity (W/mK)	Maximum Absolute Error ( $^{\circ}$ K)
1	0.5	0.3	2.51	5.56	17.14
2	0.5	0.25	1.45	3.98	10.48
3	0.3	0.4	2.01	4.87	10.44
4	0.3	0.3	1.51	4.09	6.52
5	0.2	0.2	0.31	1.36	9.93
6	0.225	0.225	0.47	1.87	6.53
7	0.228	0.25	0.63	2.49	3.74
8	0.25	0.225	0.52	2.02	4.01

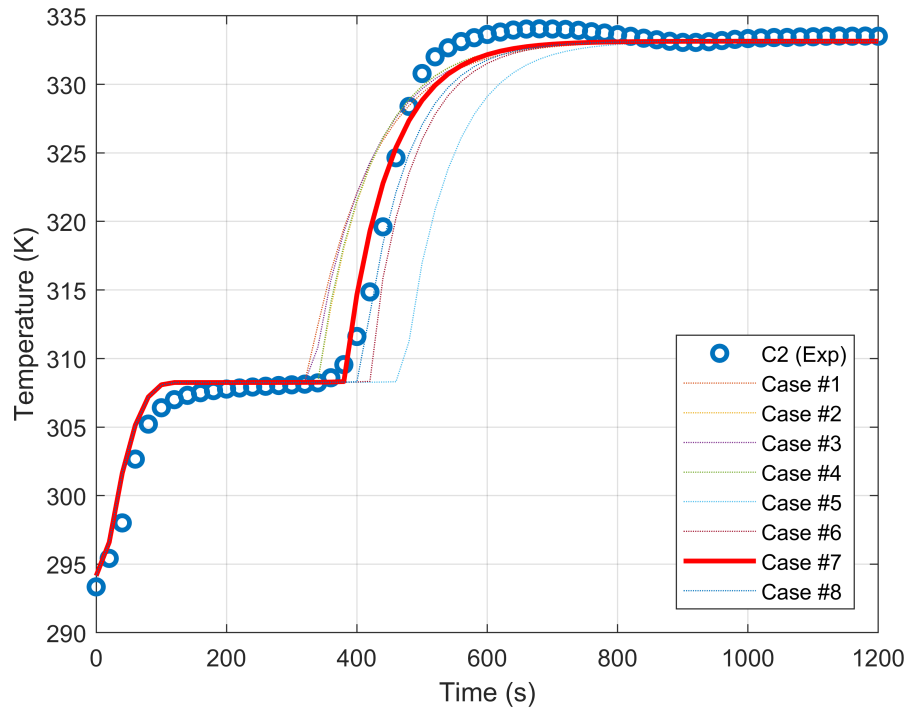
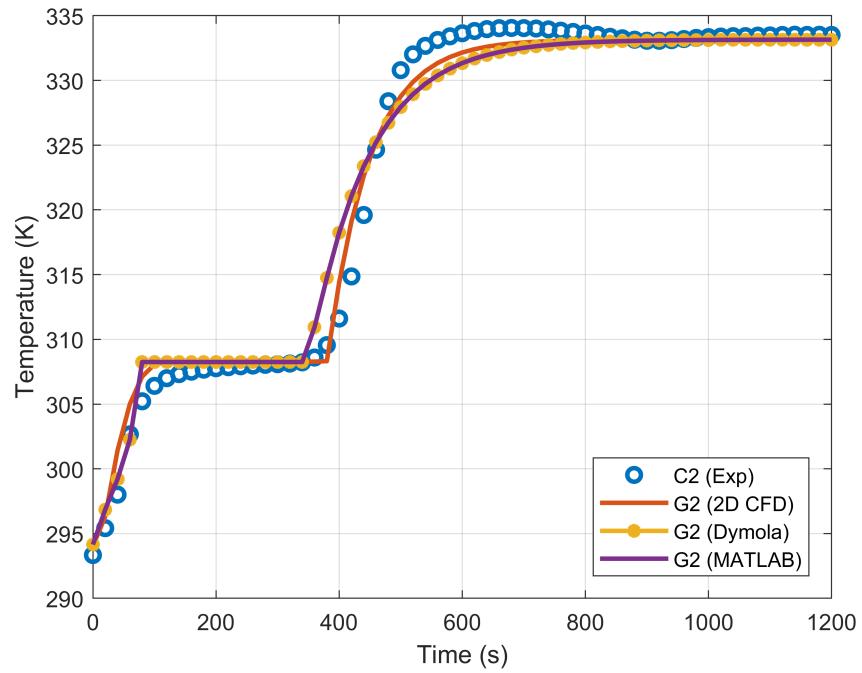


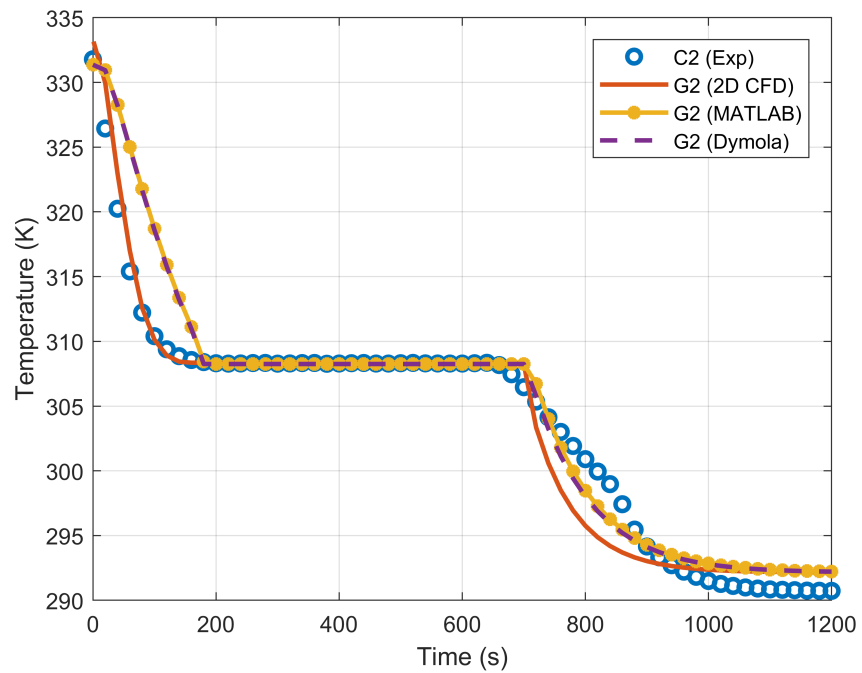
Figure 6.4: Temperature profiles for various coefficients in Rayleigh correlation

conductivity cases.

To test the validity of the empirically derived constants, they are used to predict the temperature profiles for two additional experimental case studies, where the HTF's inlet temperature is varied. The HTF inlet temperature during the melting cycle for the first



(a) Melting temperature profiles for HTF inlet at 60°C



(b) Solidification temperature profiles for HTF inlet at 19°C

Figure 6.5: Temperature profile comparison with enhanced thermal conductivity for base case

Table 6.2: Maximum absolute errors between modeling and experimental data for base case

Model	CFD	MATLAB	Dymola
Effective thermal conductivity - melting ( $^{\circ}\text{K}$ )	20.1	22.5	22.5
Enhanced thermal conductivity - melting ( $^{\circ}\text{K}$ )	3.74	5.63	5.63
Effective thermal conductivity - solidification ( $^{\circ}\text{K}$ )	10.3	15.9	15.9
Enhanced thermal conductivity - solidification ( $^{\circ}\text{K}$ )	1.71	3.11	3.11

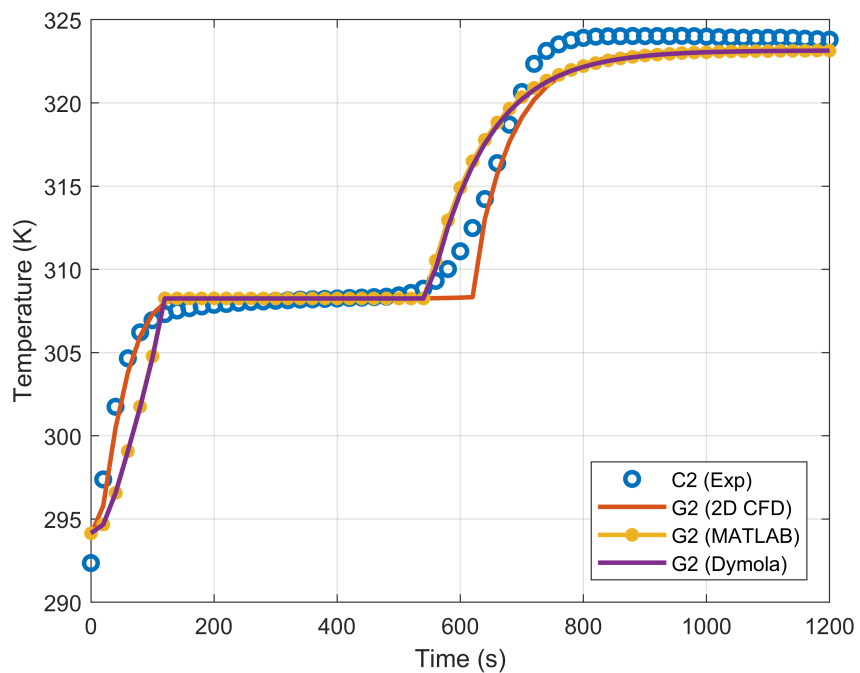
analysis is  $50^{\circ}\text{C}$ , whereas for the second it is  $70^{\circ}\text{C}$ . The solidification cycles have the same inlet temperature of  $19^{\circ}\text{C}$  in all the cases. The temperature profiles acquired from the experiments, along with those from the developed models and CFD simulations are shown in Fig. 6.6 and Fig 6.7.

The maximum absolute errors for the additional case studies with HTF inlet at  $50^{\circ}\text{C}$  and  $70^{\circ}\text{C}$  during the melt cycle is provided in Table 6.3.

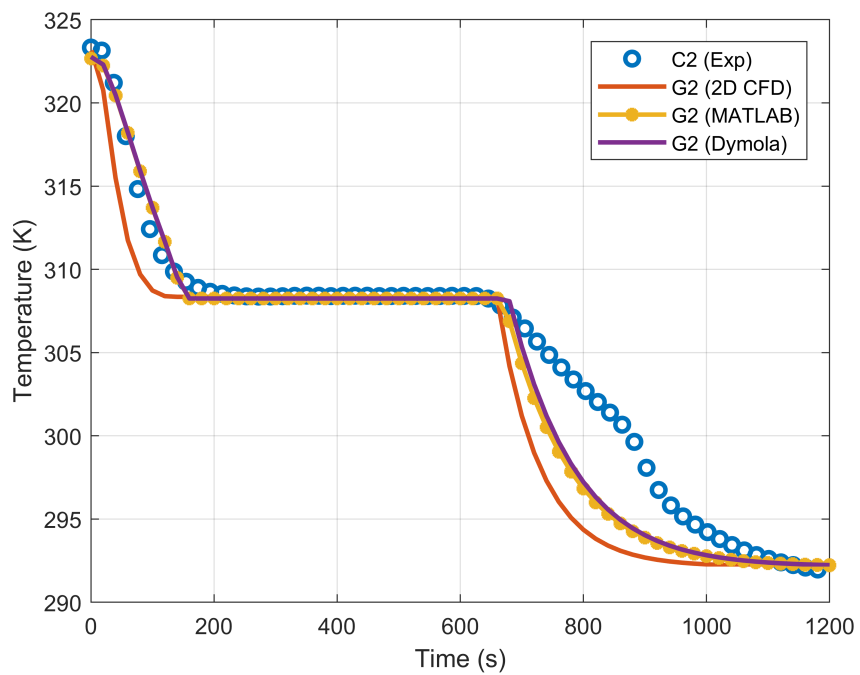
Table 6.3: Maximum absolute errors between modeling and experimental data for validation test cases

Model	CFD	MATLAB	Dymola
Maximum absolute error, $50^{\circ}\text{C}$ - melting ( $^{\circ}\text{K}$ )	4.46	5.78	5.78
Maximum absolute error, $50^{\circ}\text{C}$ - solidification ( $^{\circ}\text{K}$ )	9.98	7.73	7.73
Maximum absolute error, $70^{\circ}\text{C}$ - melting ( $^{\circ}\text{K}$ )	5.11	9.62	9.62
Maximum absolute error, $70^{\circ}\text{C}$ - solidification ( $^{\circ}\text{K}$ )	6.78	7.74	7.74

From the temperature profiles for all the three test cases, it can be seen that the maximum deviation in the temperature profiles occurs right after complete melt has been achieved. This would be the moment when the TC probes experiences the maximum effect of natural convection. Although, visually, the profiles of the enhanced thermal conductivity models show good agreement with empirical data, especially when compared to pure conduction cases, there is a need to quantify how well the models represent the real world physics. For this purpose, verification and validation of the models is carried out. This is described in the following section.

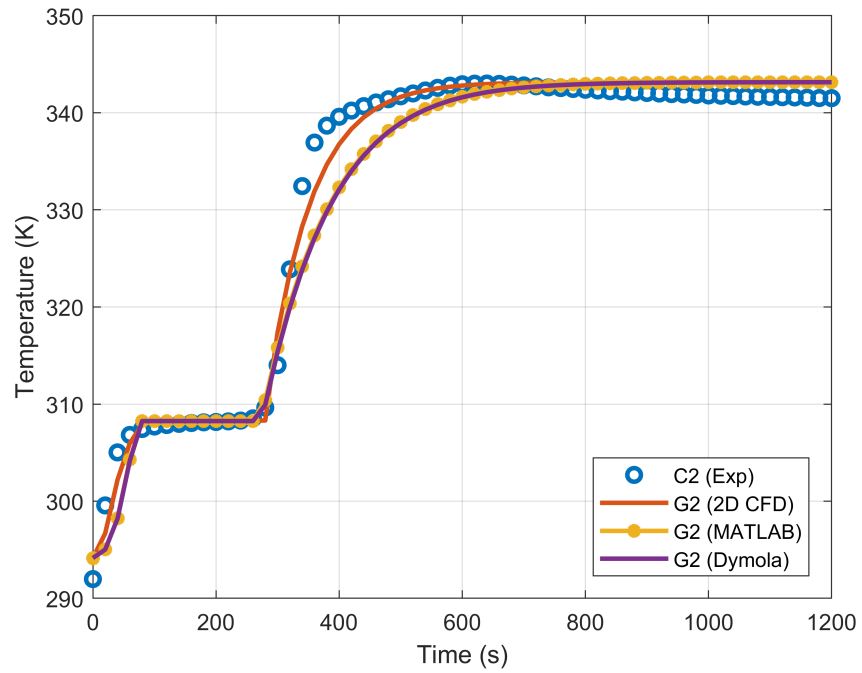


(a) Temperature profiles for HTF at 50°C

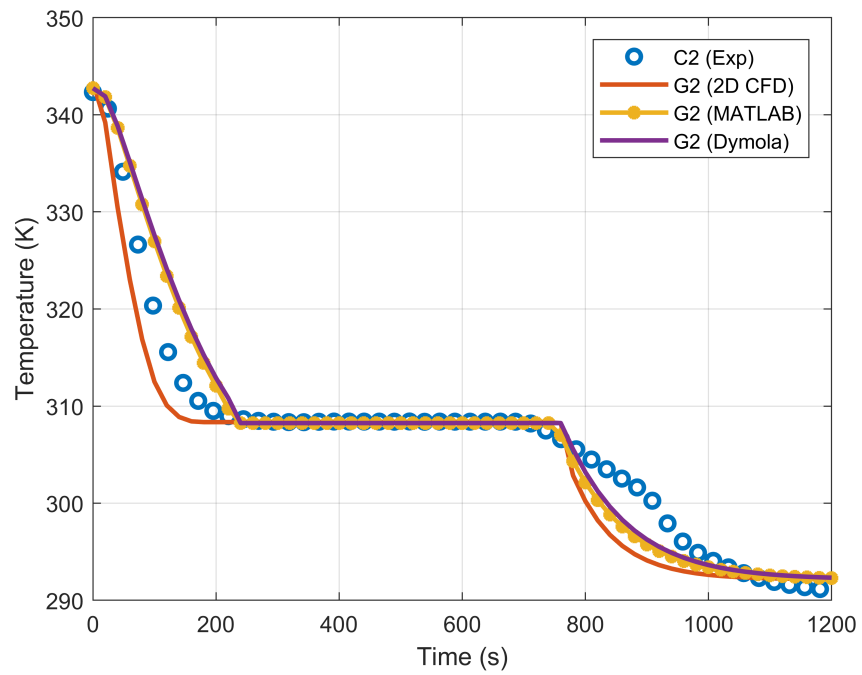


(b) Temperature profiles for HTF at 50°C

Figure 6.6: Verification of apparent thermal conductivity with additional experimental runs. HTF at 50°C



(a) Temperature profiles for HTF at 70°C



(b) Temperature profiles for HTF at 70°C

Figure 6.7: Verification of apparent thermal conductivity with additional experimental runs. HTF at 70°C

## 6.3 Verification

### 6.3.1 Solution Verification

Verification is defined as a process for assessing numerical uncertainty ( $U_{SN}$ ) and, when conditions permit, estimating the sign and magnitude of the numerical error ( $\delta_{SN}$ ) itself and the uncertainty in that error estimate [79]. This process focuses on determining whether the CFD simulation accurately represents the objective of setting up the model. The numerical error is comprised of contributions from iteration number ( $\delta_I$ ), grid size ( $\delta_G$ ), time-step ( $\delta_T$ ) and other parameters ( $\delta_P$ ), which results in the following expressions for the simulation numerical error and uncertainty

$$\delta_{SN} = \delta_I + \delta_G + \delta_T + \delta_P \quad (6.1)$$

$$U_{SN}^2 = U_I^2 + U_G^2 + U_T^2 + U_P^2 \quad (6.2)$$

Although analysis of errors resulting from spatial and temporal discretization, as well as iterative errors is within the realm of CFD, the focus herein is on the effects of grid resolution on the convergence of the solution. Therefore, the mesh sizes were varied and its effect on the dependent parameter, which is the temperature at probe G2, was studied. This probe point was chosen for the convenience with which experimental data at this location is acquired.

Currently, solution verification formulas exist only for structured grids. This is because grid sensitivity studies require accurate knowledge of the cell distribution within the domain. With structured grids, controlled grid point distribution is possible, whereas with unstructured grids, the user has little to no control over it. Although parameters exist that allow some level of control over the grid sizes, such as minimum and maximum

surface size, as well as surface growth factor, the cell volumes generated in an unstructured grid still have a varied range, and are therefore not representative of the entire domain. An example of the meshing comparison for both grid types is shown in Fig. 6.8.

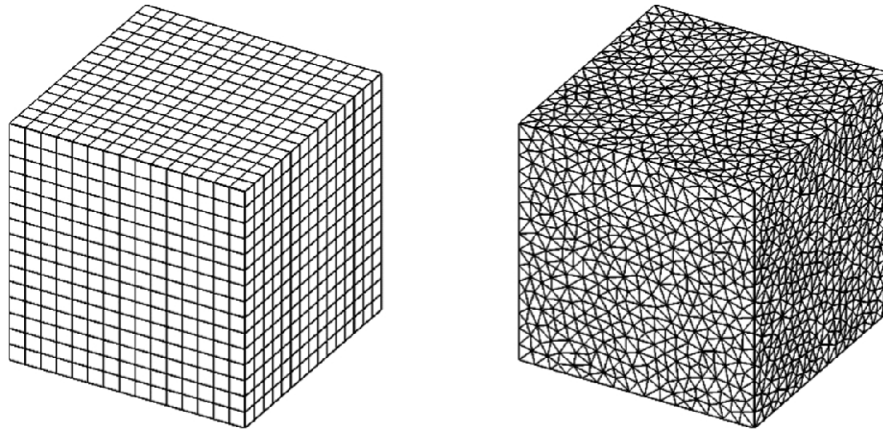


Figure 6.8: Structured vs. Unstructured Mesh [80]

As the geometry of the 3D model is complex, generating a structured grid for it would be a tedious task. Therefore, only the 2D model is considered for the solution verification process. To perform solution verification, the Generalized Richardson Extrapolation (GRE) method, as described in [79], is followed.

### 6.3.1.1 Generalized Richardson Extrapolation (GRE)

The GRE method requires a minimum of three solutions on different grid resolutions to estimate the observed order of accuracy for the simulation,  $p_{RE}$ , and the numerical error estimate,  $\delta_{RE}$ . The solution verification process followed for this study, uses three grid triplets, thereby analyzing the results over a total of five grid sizes. These grid triplets have their grid spacings as a function of a constant grid refinement ratio,  $r$ , given by

$$r = \frac{\Delta x_2}{\Delta x_1} = \frac{\Delta x_3}{\Delta x_2} \quad (6.3)$$

Here,  $\Delta x_1$ ,  $\Delta x_2$ , and  $\Delta x_3$  represent the fine, medium and coarse grid spacings respectively. Choosing an appropriate grid refinement ratio is crucial to the solution verification process. A value really close to 1 would be undesirable as the solution changes would be small and sensitivity to the grid refinement would be difficult to identify. Similarly, large values would lead to either a very coarse mesh or an extremely fine mesh – both of which are not ideal. A coarse mesh would not resolve the governing equations sufficiently to acquire accurate solutions, whereas an extremely fine mesh would result in high computational costs as well as difficulties in identifying the effects changes in grid resolution. A good alternative that is adopted commonly in industrial CFD simulations is  $r = \sqrt{2}$ , as it provides fairly large parameter refinement ratio and at least enables prolongation of the coarse-parameter solution as an initial guess for the fine-parameter solution [79]. In this study, the ratio is rounded off to 1.4.

As this is a transient analysis, the time-step size was also varied by the same factor as that for the grid refinement. This would prevent the spatial and the temporal discretization errors from dominating and compromising the verification process. Using a refinement factor of 1.4 in both, the spatial as well as a time domain, a set of five mesh refinements and their corresponding time steps are used for solution verification. The grid triplets from the five mesh sizes are (5, 4, 3), (4, 3, 2), and (3, 2, 1), which are referred to as Coarse Triplet, Medium Triplet and Fine Triplet hereon. The parameter of choice for this analysis is the temperature from probe G2, as it can be compared to the probe C2 from the experiment. Table 6.4 provides information regarding the mesh and time step sizes.

Table 6.4: Grid and time-step refinement used for grid sensitivity analysis

Mesh number	5	4	3	2	1
Grid Points (Axial x Radial)	125 x 12	175 x 17	245 x 24	345 x 34	480 x 48
Time-step size (s)	0.04	0.028	0.02	0.014	0.01

To quantify the degree by which the solution changes with grid refinement, a solution ratio,  $R$ , can be derived as follows

$$R = \frac{\epsilon_{21}}{\epsilon_{32}} \quad (6.4)$$

Here  $\epsilon_{32}$  and  $\epsilon_{21}$  refer to the solution differences between the coarse and medium grids, and the medium and fine grids respectively. The value of solution ratio,  $R$ , determines how the solution behaves upon refining the mesh. This behavior is presented as follows

- $0 < R < 1$ ,  $\rightarrow$  Monotonic Convergence
- $-1 < R < 0$ ,  $\rightarrow$  Oscillatory Convergence
- $R < -1$ ,  $\rightarrow$  Oscillatory Divergence
- $R > 1$ ,  $\rightarrow$  Monotonic Divergence

Out of the four conditions that  $R$  could behave in, monotonic convergence is the optimal outcome as it indicates that upon refining the mesh, the solution change is minimal. Therefore, there ideally exists a grid resolution at which the computed solution matches the exact solution.

The observed order of accuracy is calculated using the following expression:

$$p_{RE} = \frac{\ln(\epsilon_{32}/\epsilon_{21})}{\ln(r)} \quad (6.5)$$

and the numerical error estimate is calculated using the following:

$$\delta_{RE} = \frac{\epsilon_{21}}{r^{p_{RE}} - 1} \quad (6.6)$$

This error is then used to acquire the uncertainty error bands. It should be noted that the GRE is only applicable for monotonic convergence and therefore, in the event

that grid refinement leads to oscillatory convergence or either of the divergence behaviors, further refinement might be required. Traditionally, the Grid Convergence Index method presented by [81] has been used to estimate the error bands, however, for this study, the Factor of Safety Method as presented by [82] is used. Herein, the uncertainty is estimated using the following equation

$$U_{FS} = F_S(P) |\delta_{RE}| = \begin{cases} [FS_1 P + FS_0(1 - P)] |\delta_{RE}| & 0 < P \leq 1 \\ [FS_1 P + FS_2(P - 1)] |\delta_{RE}| & P > 1 \end{cases} \quad (6.7)$$

where  $FS_0 = 2.45$ ,  $FS_1 = 1.6$ , and  $FS_2 = 14.8$  are coefficient factors of safety derived via statistical analysis.

However, for this analysis, the temperature at the probe changes with time, which would result in varying values for the solution differences ( $\epsilon_{32}$  and  $\epsilon_{21}$ ). This would also result in varying solution ratio,  $R$ , and a varying observed order of accuracy,  $p_{RE}$ . To account for this, a profile averaged solution ratio and order of accuracy is calculated using an Euclidean norm. This is given by the following set of expressions:

$$\langle R \rangle = \frac{\|\epsilon_{21}\|_2}{\|\epsilon_{32}\|_2} \quad (6.8)$$

and

$$\langle p_{RE} \rangle = \frac{\ln[(\|\epsilon_{32}\|_2)/(\|\epsilon_{21}\|_2)]}{\ln(r)} \quad (6.9)$$

These profile averaged parameters are then used to acquire the numerical uncertainty based on the Factor of Safety method. Another source of uncertainty is the temperature data measured by the thermocouples, which also needs to be accounted to perform data validation. Based on the ASME standard for K-type thermocouples, the data uncertainty

was chosen from 0.75% of the measure value, or +/- 2.2°C, whichever is greater. The data uncertainty along with the numerical uncertainty is then used to calculate the validation uncertainty. This is given as follows:

$$U_V = \sqrt{U_D^2 + U_{FS}^2} \quad (6.10)$$

To achieve validation, the following statement has to be true:

$$|E| < U_V \quad (6.11)$$

where,  $E$  represents the error between the solution of the finest grid of a given grid triplet and the experimental data. It should be noted that the numerical uncertainty, the validation uncertainty and the error are all calculated with the experimental data as the base value i.e.  $U_{FS}(\%D)$ ,  $U_V(\%D)$ , and  $|E|(\%D)$ .

## 6.4 Model Validation

Validation refers to the process of assessing whether a given model or simulation accurately represents the real world. This process is carried out by quantifying the uncertainties in the modeling efforts using experimental data, and estimating the error. For this study, models based on pure conduction as well as those with enhanced conductivity are analyzed for validation. As natural convection is primarily a driving force during the melting, only the charging cycles are validated. The solidification cycles will be validated as a part of future work.

As observed earlier in Fig. 6.3, there is a discrepancy between the experimental and CFD data for the pure conduction case, with the difference being maximum right after complete melt has been achieved. A similar behavior is observed even when the CFD model is run for all mesh refinements. Very little differences are observed in the modeling

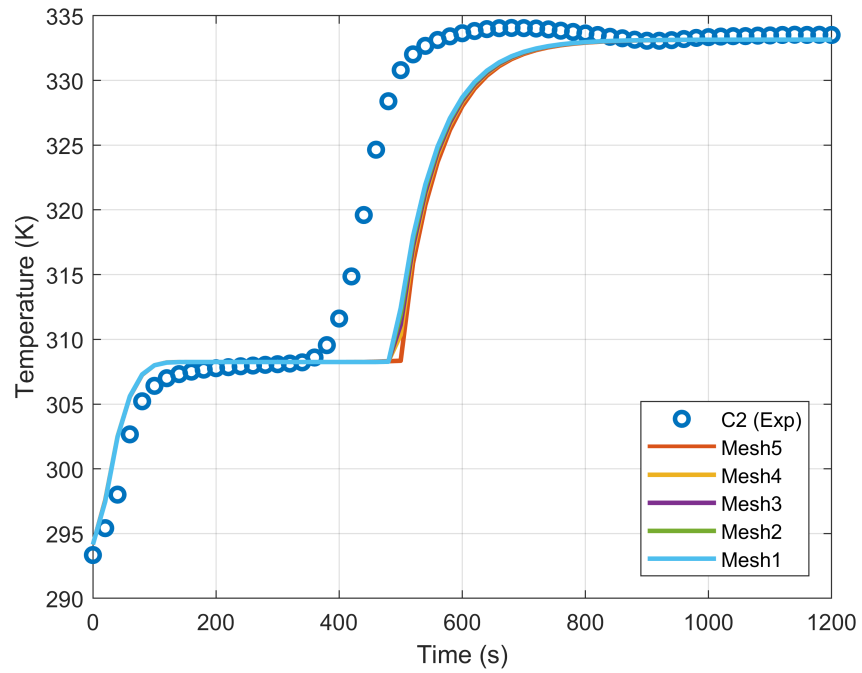
results while comparing the finest and the coarsest of meshes. This is a good indicator that the refinement that is chosen is sufficient for this analysis. Although additional refinements are possible, they come at high computational costs.

In comparison, when the enhanced thermal conductivity is applied, the agreement between the temperature profiles of the experimental data and the CFD simulations improves. This builds confidence in the enhanced thermal conductivity approach that is taken to account for natural convection, without having to employ additional governing equations. The profiles for the pure conduction and enhanced conduction cases are shown in Fig. 6.9.

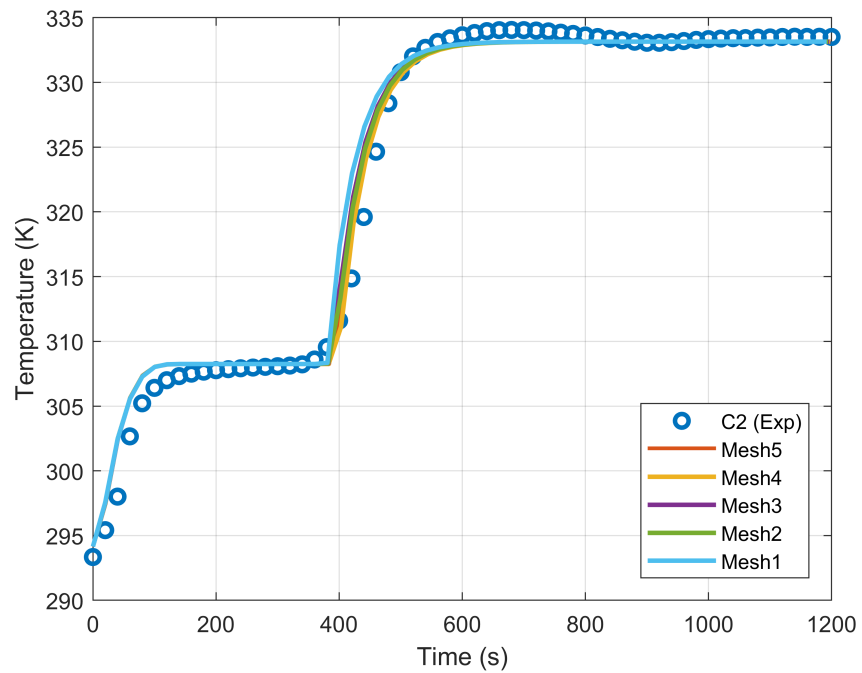
The time duration in which most of the data discrepancy is observed lies in between 400-800 seconds. This is because the rate of heat transfer is enhanced due to the combination of pure conduction and natural convection in the experimental setup, whereas the model only assumes pure conduction. This is more obvious when the errors are plotted along with the validation uncertainty bands. The pure conduction-based error plots for the three grid triplets Coarse, Medium and Fine are shown in Fig. 6.10. Similarly, the enhanced conductivity-based error plots for the three grid triplets are shown in Fig. 6.11.

It is evident from the error and uncertainty band plots that the pure conduction models are not validated over the entire melting cycle, with the maximum error occurring in the time zone right after full melt is achieved. This can be attributed to the fact that the time for full melt in the natural convection model is lower than that of the pure conduction model due to a higher heat transfer rate. In comparison, the enhanced thermal conductivity model is validated over the entire melting cycle. The maximum absolute errors for the pure conduction and enhanced conductivity cases, from the CFD simulations are provided in Table 6.5

Similar validation analysis was carried out for the developed numerical models. Only

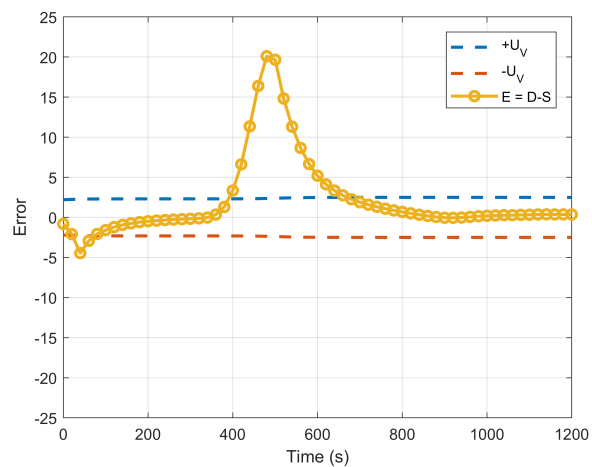


(a) Melting temperature profiles for base case with pure conduction

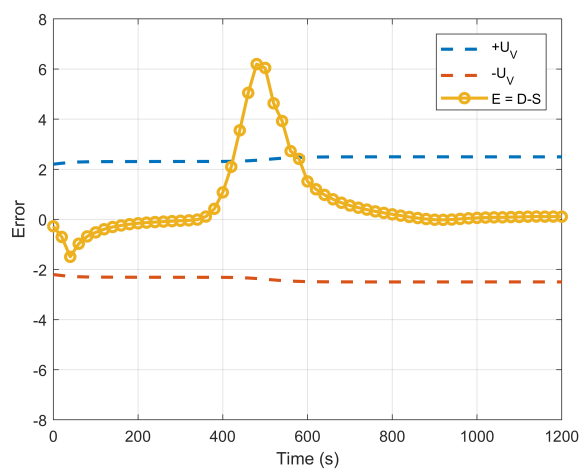


(b) Melting temperature profiles for base case with enhanced conduction

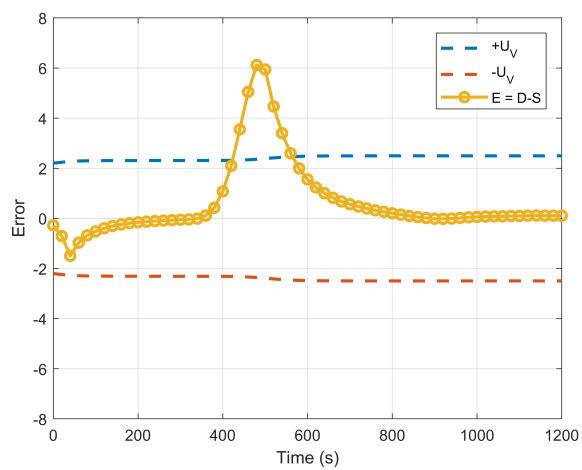
Figure 6.9: Temperature profile comparison between experiment and CFD simulations with pure conduction and enhanced thermal conductivity



(a) Error in Coarse Grid Triplet

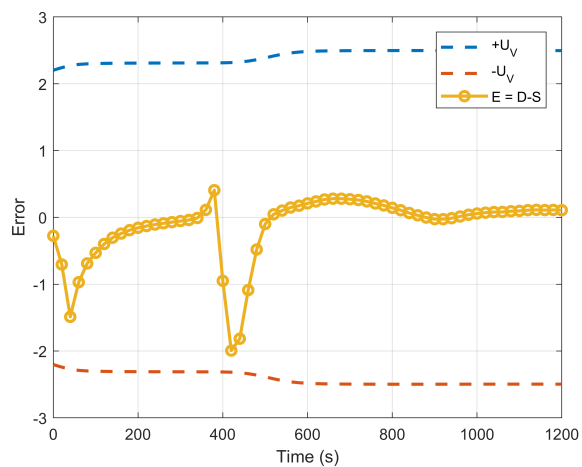


(b) Error in Medium Grid Triplet

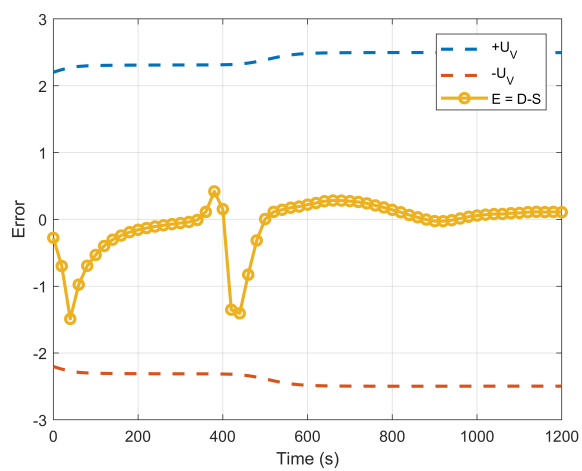


(c) Error in Fine Grid Triplet

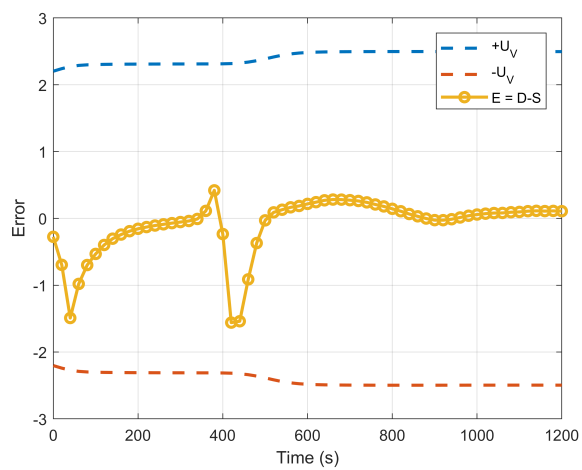
Figure 6.10: Error and uncertainty bands for base case pure conduction models in CFD



(a) Error in Coarse Grid Triplet



(b) Error in Medium Grid Triplet



(c) Error in Fine Grid Triplet

Figure 6.11: Error and uncertainty bands for base case enhanced conductivity models in CFD

Table 6.5: Maximum absolute errors in CFD models for base case validation

Model	Coarse Triplet	Medium Triplet	Fine Triplet
Pure Conduction	20.1	6.19	6.12
Enhanced Conductivity	1.99	1.55	1.48

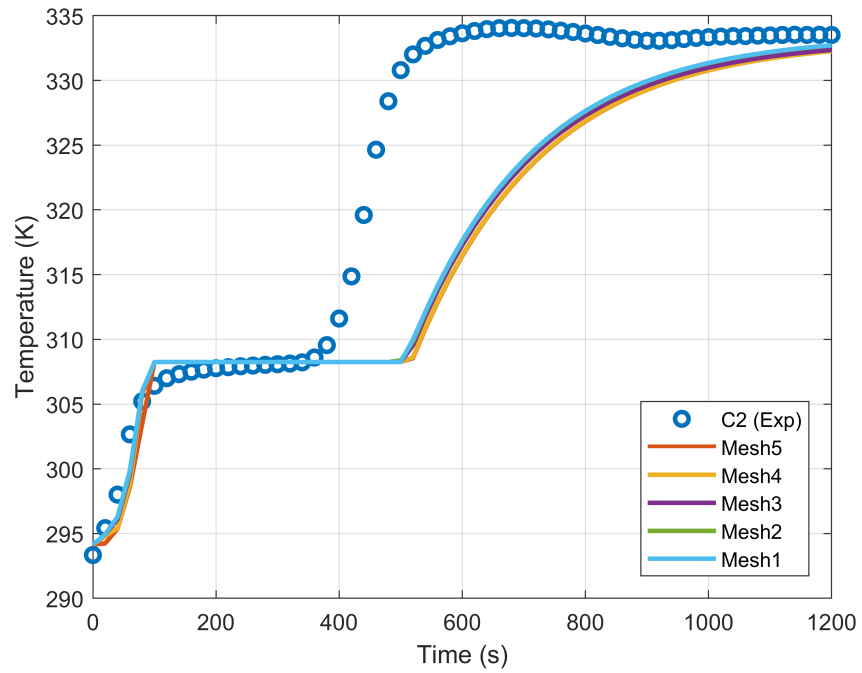
the MATLAB models are analyzed because both, the Dymola and MATLAB models have the same governing equations, resulting in the same answers. However, the MATLAB models have a lower simulation runtime and are therefore the preferred option. Figure 6.12 shows the pure conduction-based model and the enhanced conductivity-based model temperature profiles for all the grid refinements, plotted along with the experimental data. Similar trends are observed in these plots as well, wherein the time to melt is better captured with the enhanced thermal conductivity-based models.

As for the error plots in the pure conduction modeling case, only the Fine Triplet plot is generated and shown in Fig. 6.13. This is because the Medium and Coarse Triplets have diverging solutions, with their solution ratio values of 1.46 and 8.91, respectively. Although further grid refinements could have been made to check for convergence, it would have been computationally expensive and all the other simulations would also need to be re-run.

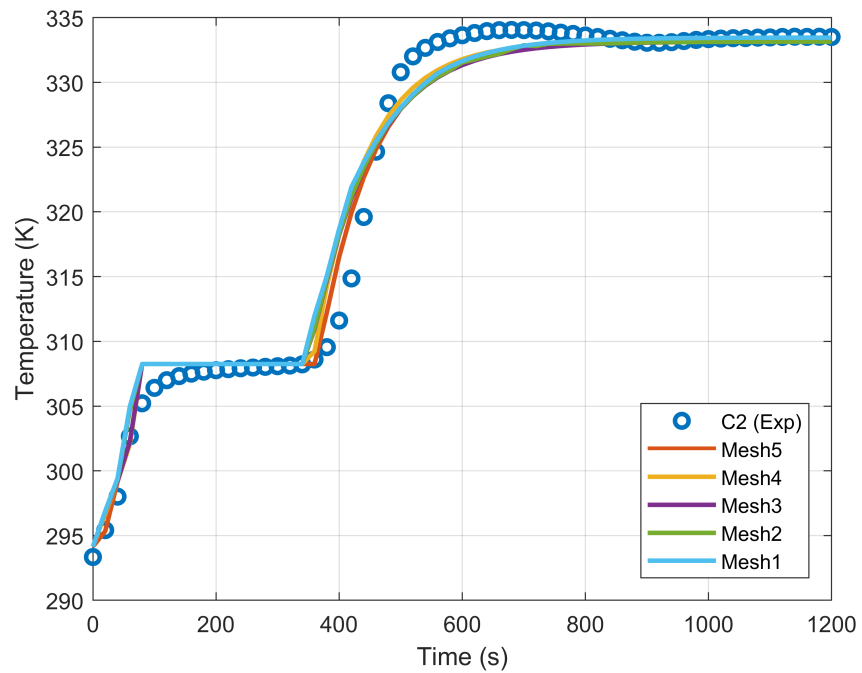
In comparison to the pure conduction models, the enhanced conductivity produces results in the MATLAB, similar to those acquired from the CFD models. The error plots for the pure conduction case are shown in Fig. 6.14, and the maximum absolute errors for the MATLAB models are provided in Table 6.6.

Table 6.6: Maximum absolute errors in numerical models for base case validation

Model	Coarse Triplet	Medium Triplet	Fine Triplet
Pure Conduction	N/A	N/A	7.64
Enhanced Conductivity	2.13	1.93	1.67



(a) Melting temperature profiles for base case with pure conduction



(b) Melting temperature profiles for base case with enhanced conduction

Figure 6.12: Temperature profile comparison between experiment and MATLAB model with pure conduction and enhanced thermal conductivity

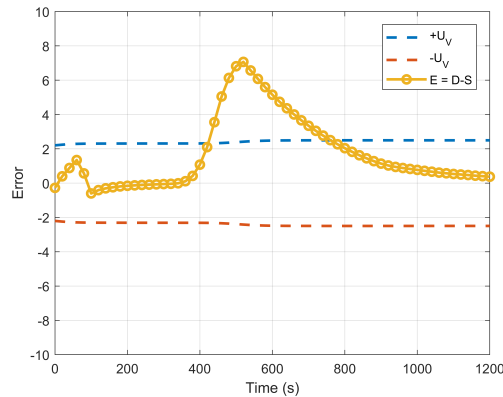
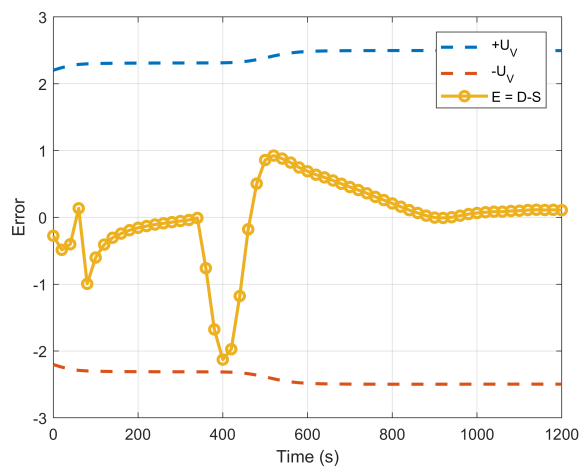


Figure 6.13: Error and uncertainty bands for base case pure conduction models in MATLAB

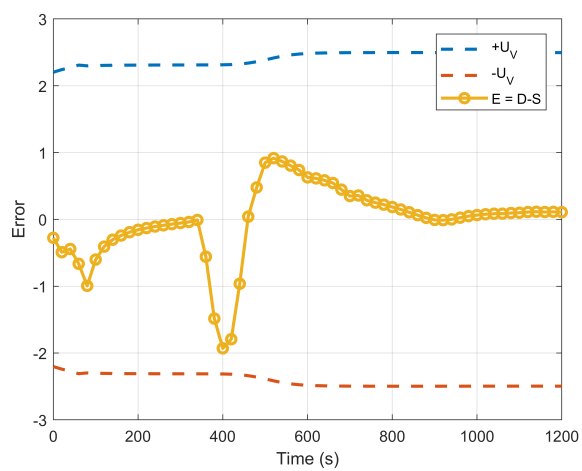
## 6.5 Preliminary Analysis - Unfinned Test Section

Experimental runs are carried out on the unfinned test section, while maintaining the same operating conditions as those for the finned design. Temperature profiles for melting and solidification, similar to those from the finned test section are acquired for the unfinned design, and are shown in Fig. 6.15. It is evident from the temperature plots during the melting and solidification cycles that heat transfer enhancement due to natural convection needs to be accounted for, if an accurate model is to be developed. It can also be seen that the duration for melt and solidification is higher for the unfinned design, when compared to the finned design. This is more visible from the plots in Fig. 6.16.

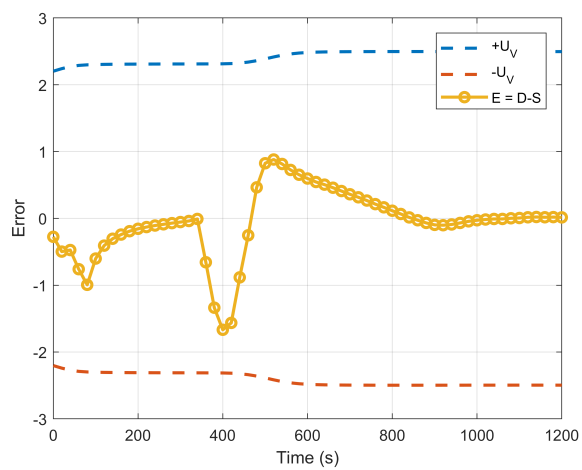
It is evident that the finned design has better heat transfer characteristics when compared to the unfinned design. The melt time is about 2.5 times faster, whereas the solidification time is about 1.7 times faster. Additional data analysis of the unfinned design needs to be carried out, and the models need to be validated.



(a) Error in Coarse Grid Triplet

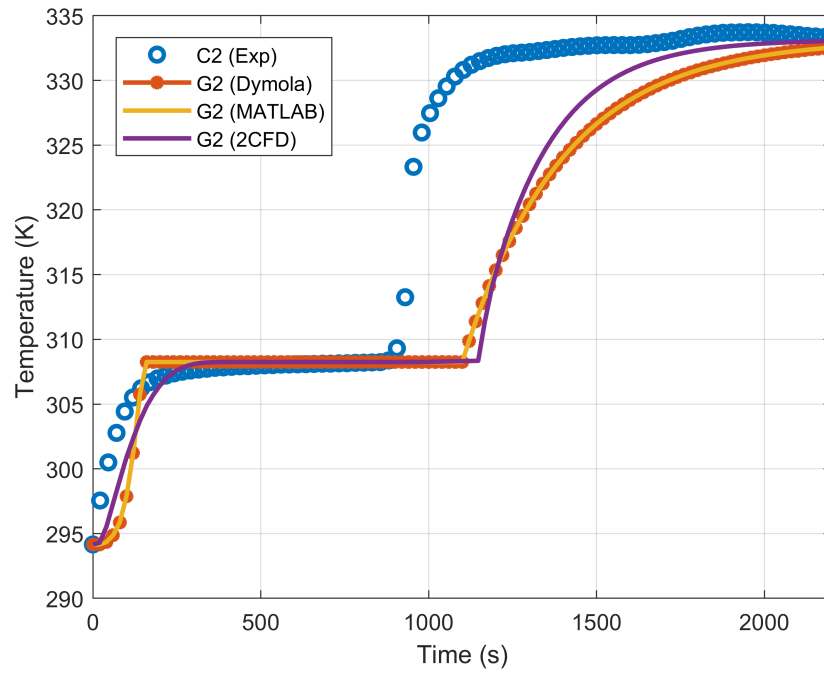


(b) Error in Medium Grid Triplet

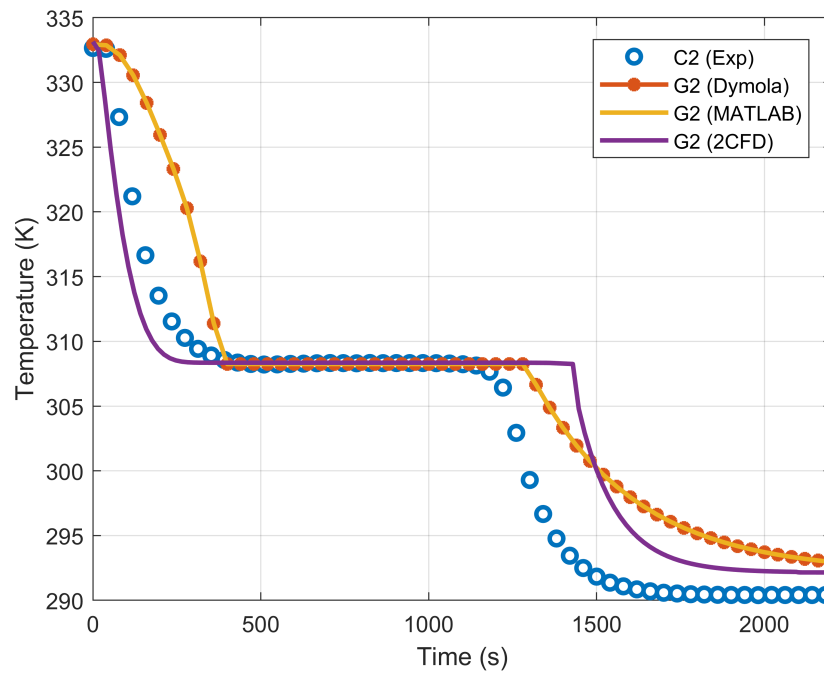


(c) Error in Fine Grid Triplet

Figure 6.14: Error and uncertainty bands for base case enhanced conductivity models in MATLAB

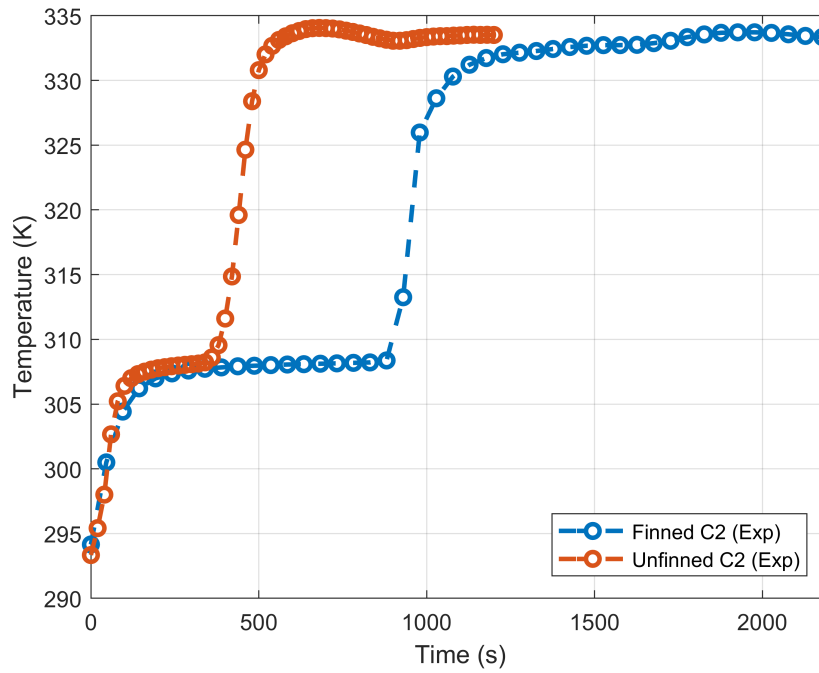


(a) Temperature profiles during melting

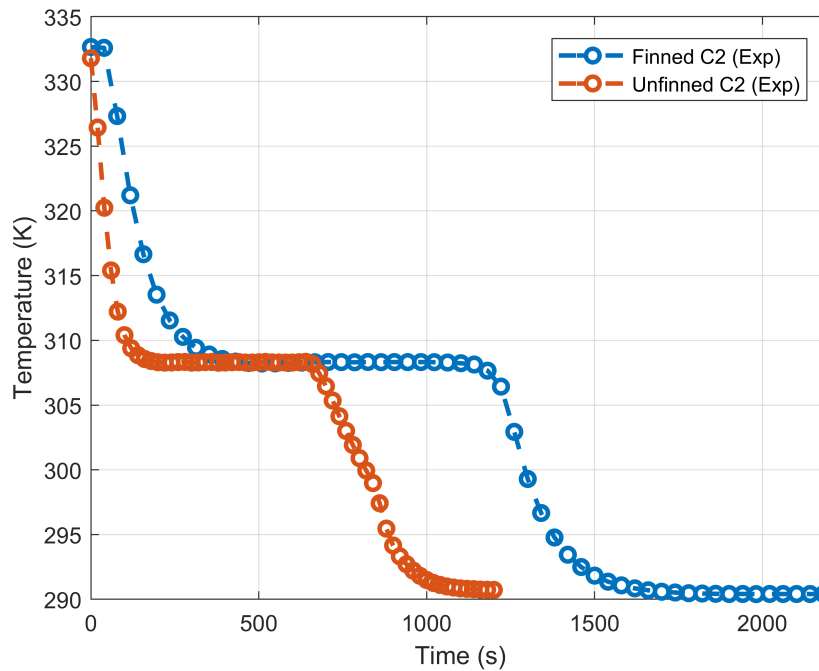


(b) Temperature profiles during solidification

Figure 6.15: Comparison of temperature profiles from numerical models, CFD simulation and unfinned tube experiment



(a) Temperature profile comparison during melting



(b) Temperature profile comparison during solidification

Figure 6.16: Temperature profile comparison for finned and unfinned test sections

## CHAPTER 7

### Conclusions and Future Work

#### 7.1 Conclusions

The goal of this dissertation was to develop a simplified, semi-empirical model for an LH-TES system. In the process of doing so, two numerical models, several CFD simulations and several experimental runs were carried out to analyze the thermal hydraulic performance of the developed models, and to quantify their accuracy in predicting the thermal behavior of the system. The summary of the major conclusions is listed as follows:

(1) The effective thermal conductivity for the finned tube design derived from the thermal resistance network accurately predicts the enhanced heat transfer to and from the PCM. This overcomes the need to numerically model the fin and PCM domains separately, and is a better predictor of effective thermal conductivity than the volume fraction-based derivations provided in literature.

(2) Pure conduction-based models do not accurately represent the thermal hydraulic behavior of a phase change system considered for this study, primarily during the melting cycle. Only the sensible heat addition, which takes place during the initial heating of the PCM, from room temperature up to its melting point is modeled with decent accuracy. As the pure conduction models neglect the enhancement in heat transfer brought about by natural convection, they over-predict the time to melt.

(3) The derivation of the two thermal conductivities, namely, the effective conductivity due to the presence of fins, and the apparent conductivity in the liquid domain to account for natural convection, simplifies the modeling of phase change analysis in a structurally enhanced LH-TES. The combination of the two leads to the development of an enhanced thermal conductivity, which is the novel contribution to the scientific community that

was developed as a part of this work. The models with the application of enhanced thermal conductivity predict the phase change behavior with good accuracy. All the models - numerical as well as CFD - are validated over the ranges that were considered for this study.

(4) Several models were developed over the course of this study. These include 2D analytical, 2D numerical in MATLAB and Dymola, and 2D models in STAR-CCM+. The first approximation analytical model is accurate enough for a preliminary feasibility analysis, sizing calculation and charge/discharge rates. The numerical models with the application of enhanced thermal conductivity provide accurate information about the thermal hydraulic performance of the LH-TES system considered for this study. The CFD simulations agree well with the numerical models, as well as with the experimental results. The end result of this model development stage has produced three models which can be tested for a combination of PCMs and LH-TES geometries.

(5) Out of all the models considered for this analysis, the MATLAB models have the lowest simulation runtime, whereas the Dymola models have the highest. MATLAB being a sequential solver solves the equations one after the other. In comparison, Dymola runs an initialization process to minimize the matrix sizes, generated as a result of differential equations, in order to run the system of equations more efficiently. Depending on how large the matrices get, the initialization process can delay to overall simulation runtime. Table 7.1 provides the simulation runtime data.

The goals that were set out for this work have been met. A simplified, validated model for phase change analysis has been developed in MATLAB and Dymola, and CFD simulations for the same have been run using STAR-CCM+. Although the Dymola model is slow when compared to its MATLAB counterpart, this is the first phase-change analysis model in the Modelica-based library. The developed numerical models, along with the CFD simulations agree well experimental data, when the empirically acquired

enhanced thermal conductivity is applied.

Table 7.1: Simulation runtime for models at different mesh refinements (time in seconds)

Mesh number	CFD	MATLAB	Dymola
5 (125 x 12)	2460	146	1098
4 (175 x 17)	4920	333	8520
3 (245 x 24)	8940	418	20940
2 (345 x 34)	15840	654	71107
1 (480 x 48)	23280	989	193616

## 7.2 Future Work

The simplified models developed herein are accurate within reason, however, more work is needed before they can be used to design LH-TES systems for large-scale deployment. Some of the tasks that need to be carried out in the future are listed as follows:

(1) The data acquisition and analysis is only complete for the finned test section. Although preliminary analysis has been carried out for the unfinned design, detailed analysis needs to be conducted to ensure that the semi-empirical model is valid even in the unfinned design.

(2) Simulations on a 3D CFD model, representing  $1/6^{th}$  of the hexagonal geometry were also run to draw a better comparison between the experimental data and the CFD simulations. This data analysis also needs to be completed.

(3) The test section in the experiments was charged and discharged from the top. In a generic LH-TES, an ideal way would be to charge by flowing the HTF from the top, while discharging by flow the fluid through the bottom. The current experimental setup will have to be modified to allow for such experimental runs.

(3) Currently, only one PCM was analyzed for this study. To ensure that the

parameters derived herein can represent other materials as well, additional experiments will have to be carried out.

(4) The current models only work with a single phase HTF. To account for phase change within the HTF, along with pressure drops, the continuity and momentum equations will have to be resolved in the HTF domain. This would allow modeling condensation and boiling of steam/water, which is an attractive modeling effort for the current energy storage industry.

(5) As mentioned earlier, the effect of natural convection was found to be low in this particular test section. This might be due to the low Rayleigh number as a result of selecting the PCM thickness as the critical length. To understand this phenomenon in detail, test sections with different designs need to be studied. This can now be done computationally, as it is cheaper than experimental work, and the models used in this study provide a good representation of the real world. Such an analysis would allow one to see how well the apparent thermal conductivity parameters hold for different designs.

(6) Design optimization can also be carried out based on a set of objective functions, to maximize the storage capacity, with high charge and discharge rates and minimal storage material. This can be carried out computationally, and once an optimized design is acquired, the model can be built and tested experimentally.

The three pronged approach of mathematical modeling, CFD simulations, and experimental analysis, undertaken to accomplish the tasks of this study have produced satisfactory results. Although, many more case studies can be run on the test section at hand, the primary goal of developing a simplified model for a phase change system has been met. The numerical and CFD models developed herein will act as stepping stones towards development and analysis of better, more accurate LH-TES system models.

## Bibliography

- [1] “Mitigation of climate change,” *Contribution of Working Group III to the Fifth Assessment Report of the Intergovernmental Panel on Climate Change*, vol. 1454, 2014.
- [2] “Goddard institute for space studies,” <https://data.giss.nasa.gov/gistemp/>, accessed: 2019-05-01.
- [3] “Global climate change - vital signs of the planet,” <https://climate.nasa.gov/effects/>, accessed: 2019-05-01.
- [4] R. Pachauri and A. Reisinger, “Ar4 climate change 2007: Synthesis report,” Intergovernmental Panel on Climate Change (IPCC), Tech. Rep., 2016.
- [5] M. Ruth, D. Cutler, F. Flores-Espino, G. Stark, T. Jenkin, T. Simpkins, and J. Macknick, “The economic potential of two nuclear-renewable hybrid energy systems,” National Renewable Energy Laboratory, Tech. Rep., 2016.
- [6] O. Edenhofer, R. Pichs-Madruga, Y. Sokona, K. Seyboth, S. Kadner, T. Zwickel, P. Eickemeier, G. Hansen, S. Schlömer, C. von Stechow *et al.*, *Renewable energy sources and climate change mitigation: Special report of the intergovernmental panel on climate change*. Cambridge University Press, 2011.
- [7] CAISO, “What the duck curve tells us about managing a green grid,” *Calif. ISO, Shap. a Renewed Futur*, pp. 1–4, 2012.
- [8] S. M. Bragg-Sitton, R. Boardman, C. Rabiti, J. Suk Kim, M. McKellar, P. Sabharwall, J. Chen, M. S. Cetiner, T. J. Harrison, and A. L. Qualls, “Nuclear-renewable hybrid energy systems: 2016 technology development program plan,” Idaho National Lab.(INL), Idaho Falls, ID (United States); Oak Ridge . . . , Tech. Rep., 2016.

- [9] “Levelized cost and levelized avoided cost of new generation resources in the annual energy outlook 2020,” U.S. Energy Information Administration, Tech. Rep., 2020.
- [10] C. K. Ho, “A review of high-temperature particle receivers for concentrating solar power,” *Applied Thermal Engineering*, vol. 109, pp. 958–969, 2016.
- [11] G. J. Kolb, C. K. Ho, T. R. Mancini, and J. A. Gary, “Power tower technology roadmap and cost reduction plan,” *SAND2011-2419, Sandia National Laboratories, Albuquerque, NM*, vol. 7, 2011.
- [12] J. Coleman, S. Bragg-Sitton, and E. Dufek, “An evaluation of energy storage options for nuclear power,” Idaho National Lab.(INL), Idaho Falls, ID (United States), Tech. Rep., 2017.
- [13] J. E. Rea, C. J. Oshman, M. L. Olsen, C. L. Hardin, G. C. Glatzmaier, N. P. Siegel, P. A. Parilla, D. S. Ginley, and E. S. Toberer, “Performance modeling and techno-economic analysis of a modular concentrated solar power tower with latent heat storage,” *Applied energy*, vol. 217, pp. 143–152, 2018.
- [14] J. P. da Cunha and P. Eames, “Compact latent heat storage decarbonisation potential for domestic hot water and space heating applications in the uk,” *Applied Thermal Engineering*, vol. 134, pp. 396–406, 2018.
- [15] T. Nomura, N. Okinaka, and T. Akiyama, “Technology of latent heat storage for high temperature application: a review,” *ISIJ international*, vol. 50, no. 9, pp. 1229–1239, 2010.
- [16] K. Frick, A. Duenas, P. Sabharwall, J. Yoo, S.-J. Yoon, C. Stoots, J. O’Brien, and T. O’Brien, “Operation and control of the inl thermal energy delivery system (teds),” Idaho National Lab.(INL), Idaho Falls, ID (United States), Tech. Rep., 2019.

- [17] N. V. Khartchenko and V. M. Kharchenko, *Advanced energy systems*. CRC Press, 2013.
- [18] “The parabolic trough power plants andasol 1 to 3,” Solar Millenium, Tech. Rep., 2016.
- [19] The National Renewable Energy Laboratory, “Concentrating solar power projects.” [Online]. Available: <https://solarpaces.nrel.gov/>
- [20] “Drake landing solar community,” <https://www.dlsc.ca/>, accessed: 2019-02-12.
- [21] X. Luo, J. Wang, M. Dooner, and J. Clarke, “Overview of current development in electrical energy storage technologies and the application potential in power system operation,” *Applied energy*, vol. 137, pp. 511–536, 2015.
- [22] G. Brett and M. Barnett, “The application of liquid air energy storage for large scale long duration solutions to grid balancing,” in *EPJ Web of Conferences*, vol. 79. EDP Sciences, 2014, p. 03002.
- [23] Y. Ding, L. Tong, P. Zhang, Y. Li, J. Radcliffe, and L. Wang, “Liquid air energy storage,” in *Storing Energy*. Elsevier, 2016, pp. 167–181.
- [24] W.-D. Steinmann and M. Eck, “Buffer storage for direct steam generation,” *Solar Energy*, vol. 80, no. 10, pp. 1277–1282, 2006.
- [25] R. Osuna, R. Olavarria, R. Morillo, M. Sánchez, F. Cantero, V. Fernández-Quero, P. Robles, T. López, A. Esteban, F. Céron *et al.*, “Ps10, construction of a 11mw solar thermal tower plant in seville, spain,” in *Proc. SolarPACES conference, Seville, Spain*, 2006.

- [26] C. Castellón, A. Castell, M. Medrano, I. Martorell, and L. Cabeza, “Experimental study of pcm inclusion in different building envelopes,” *Journal of Solar Energy Engineering*, vol. 131, no. 4, 2009.
- [27] “Miracradle<sup>®</sup> neonate cooler,” <http://www.miracradle.com/product.html>, accessed: 2018-10-14.
- [28] “Sonoco thermosafe greenbox,” <https://www.thermosafe.com/subcategory/greenbox>, accessed: 2020-01-29.
- [29] D. Kearney, U. Herrmann, P. Nava, B. Kelly, R. Mahoney, J. Pacheco, R. Cable, N. Potrovitza, D. Blake, and H. Price, “Assessment of a molten salt heat transfer fluid in a parabolic trough solar field,” *J. Sol. Energy Eng.*, vol. 125, no. 2, pp. 170–176, 2003.
- [30] T. L. Knighton, A. Shigrekar, D. S. Wendt, R. D. Boardman, B. Murphy, and B. D. James, “Markets and economics for thermal power extraction from nuclear power plants aiding the decarbonization of industrial processes,” U.S. Department of Energy, Tech. Rep., 2020.
- [31] B. Zalba, J. M. Marin, L. F. Cabeza, and H. Mehling, “Review on thermal energy storage with phase change: materials, heat transfer analysis and applications,” *Applied thermal engineering*, vol. 23, no. 3, pp. 251–283, 2003.
- [32] A. Abhat, “Low temperature latent heat thermal energy storage: heat storage materials,” *Solar energy*, vol. 30, no. 4, pp. 313–332, 1983.
- [33] A. Siahpush, J. O’Brien, and J. Crepeau, “Phase change heat transfer enhancement using copper porous foam,” *Journal of Heat Transfer*, vol. 130, no. 8, 2008.

- [34] B. J. Jones, D. Sun, S. Krishnan, and S. V. Garimella, "Experimental and numerical study of melting in a cylinder," *International Journal of Heat and Mass Transfer*, vol. 49, no. 15-16, pp. 2724–2738, 2006.
- [35] C. Vélez, M. Khayet, and J. O. De Zárata, "Temperature-dependent thermal properties of solid/liquid phase change even-numbered n-alkanes: n-hexadecane, n-octadecane and n-eicosane," *Applied Energy*, vol. 143, pp. 383–394, 2015.
- [36] C. Li, B. Zhang, and Q. Liu, "N-eicosane/expanded graphite as composite phase change materials for electro-driven thermal energy storage," *Journal of Energy Storage*, vol. 29, p. 101339, 2020.
- [37] B. Durakovic and M. Torlak, "Experimental and numerical study of a pcm window model as a thermal energy storage unit," *International Journal of Low-Carbon Technologies*, vol. 12, no. 3, pp. 272–280, 2017.
- [38] A. M. Borreguero, M. Carmona, M. L. Sanchez, J. L. Valverde, and J. F. Rodriguez, "Improvement of the thermal behaviour of gypsum blocks by the incorporation of microcapsules containing pcms obtained by suspension polymerization with an optimal core/coating mass ratio," *Applied Thermal Engineering*, vol. 30, no. 10, pp. 1164–1169, 2010.
- [39] E. Assis, L. Katsman, G. Ziskind, and R. Letan, "Numerical and experimental study of melting in a spherical shell," *International Journal of Heat and Mass Transfer*, vol. 50, no. 9-10, pp. 1790–1804, 2007.
- [40] H. Liu, S. Li, Y. Chen, and Z. Sun, "The melting of phase change material in a cylinder shell with hierarchical heat sink array," *Applied thermal engineering*, vol. 73, no. 1, pp. 975–983, 2014.

- [41] G. Lamé and B. Clapeyron, “Mémoire sur la solidification par refroidissement d’un globe liquide,” in *Annales Chimie Physique*, vol. 47, 1831, pp. 250–256.
- [42] H. Carslaw and J. Jaeger, “Conduction of heat in solids,” *Clarendon, Oxford*, 1959.
- [43] J. Gammon and J. Howarth, “The two-dimensional stefan problem with slightly varying heat flux,” *International communications in heat and mass transfer*, vol. 22, no. 5, pp. 629–638, 1995.
- [44] X. Quan-Sheng and Z. You-Lan, “Solution of the two-dimensional stefan problem by the singularity-separating method,” *Journal of Computational Mathematics*, pp. 8–18, 1985.
- [45] F. Yigit, “Approximate analytical and numerical solutions for a two-dimensional stefan problem,” *Applied mathematics and computation*, vol. 202, no. 2, pp. 857–869, 2008.
- [46] J. Blazek, *Computational fluid dynamics: principles and applications*. Butterworth-Heinemann, 2015.
- [47] P. McDonald, *The computation of transonic flow through two-dimensional gas turbine cascades*. American Society of Mechanical Engineers, 1971, vol. 79825.
- [48] R. MacCormack and A. Paullay, “Computational efficiency achieved by time splitting of finite difference operators,” in *10th Aerospace Sciences Meeting*, 1972, p. 154.
- [49] R. Abdel-Wahed, J. Ramsey, and E. M. Sparrow, “Photographic study of melting about an embedded horizontal heating cylinder,” *International Journal of Heat and Mass Transfer*, vol. 22, no. 1, pp. 171–173, 1979.
- [50] K. Ermis, A. Erek, and I. Dincer, “Heat transfer analysis of phase change process in a finned-tube thermal energy storage system using artificial neural network,”

*International Journal of Heat and Mass Transfer*, vol. 50, no. 15-16, pp. 3163–3175, 2007.

- [51] K. Ismail, C. Alves, and M. Modesto, “Numerical and experimental study on the solidification of pcm around a vertical axially finned isothermal cylinder,” *Applied Thermal Engineering*, vol. 21, no. 1, pp. 53–77, 2001.
- [52] J. C. Choi and S. D. Kim, “Heat-transfer characteristics of a latent heat storage system using  $\text{mgcl}_2 \cdot 6\text{h}_2\text{o}$ ,” *Energy*, vol. 17, no. 12, pp. 1153–1164, 1992.
- [53] B. Horbaniuc, G. Dumitrascu, and A. Popescu, “Mathematical models for the study of solidification within a longitudinally finned heat pipe latent heat thermal storage system,” *Energy Conversion and Management*, vol. 40, no. 15-16, pp. 1765–1774, 1999.
- [54] E. M. Sparrow, E. Larson, and J. Ramsey, “Freezing on a finned tube for either conduction-controlled or natural-convection-controlled heat transfer,” *International Journal of Heat and Mass Transfer*, vol. 24, no. 2, pp. 273–284, 1981.
- [55] R. Velraj, R. Seeniraj, B. Hafner, C. Faber, and K. Schwarzer, “Experimental analysis and numerical modelling of inward solidification on a finned vertical tube for a latent heat storage unit,” *Solar Energy*, vol. 60, no. 5, pp. 281–290, 1997.
- [56] K. SASAGUCHI, H. IMURA, and H. FURUSHO, “Heat transfer characteristics of a latent heat storage unit with a finned tube: 1st report experimental studies on solidification and melting processes,” *Bulletin of JSME*, vol. 29, no. 255, pp. 2978–2985, 1986.
- [57] P. Padmanabhan and M. K. Murthy, “Outward phase change in a cylindrical annulus with axial fins on the inner tube,” *International Journal of Heat and Mass Transfer*, vol. 29, no. 12, pp. 1855–1868, 1986.

- [58] J. P. Trelles and J. J. Duflly, "Numerical simulation of porous latent heat thermal energy storage for thermoelectric cooling," *Applied Thermal Engineering*, vol. 23, no. 13, pp. 1647–1664, 2003.
- [59] C. Hoogendoorn and G. Bart, "Performance and modelling of latent heat stores," *Solar energy*, vol. 48, no. 1, pp. 53–58, 1992.
- [60] E.-B. S. Mettawee and G. M. Assassa, "Thermal conductivity enhancement in a latent heat storage system," *Solar Energy*, vol. 81, no. 7, pp. 839–845, 2007.
- [61] P. Griffiths and P. Eames, "Performance of chilled ceiling panels using phase change material slurries as the heat transport medium," *Applied Thermal Engineering*, vol. 27, no. 10, pp. 1756–1760, 2007.
- [62] M. Hawlader, M. Uddin, and M. M. Khin, "Microencapsulated pcm thermal-energy storage system," *Applied energy*, vol. 74, no. 1-2, pp. 195–202, 2003.
- [63] E. Hahne, "Thermal energy storage some views on some problems," in *International Heat Transfer Conference Digital Library*. Begel House Inc., 1986.
- [64] N. Hale Jr, "Heat transfer during melting and freezing of phase change thermal energy storage materials," *MSME Thesis, Purdue University*, 1978.
- [65] N. Hale Jr and R. Viskanta, "Solid-liquid phase-change heat transfer and interface motion in materials cooled or heated from above or below," *International Journal of Heat and Mass Transfer*, vol. 23, no. 3, pp. 283–292, 1980.
- [66] W. R. Humphries and E. I. Griggs, "A design handbook for phase change thermal control and energy storage devices," *STIN*, vol. 78, p. 15434, 1977.

- [67] W. Wagner and A. Pruß, “The iapws formulation 1995 for the thermodynamic properties of ordinary water substance for general and scientific use,” *Journal of physical and chemical reference data*, vol. 31, no. 2, pp. 387–535, 2002.
- [68] Wikipedia contributors, “Divergence theorem — Wikipedia, the free encyclopedia,” 2020. [Online]. Available: [https://en.wikipedia.org/wiki/Divergence\\_theorem](https://en.wikipedia.org/wiki/Divergence_theorem)
- [69] S. Mazumder, *Numerical methods for partial differential equations: finite difference and finite volume methods*. Academic Press, 2015.
- [70] The Modelica Association, “Modelica language.” [Online]. Available: <https://www.modelica.org/modelicalanguage>
- [71] L. R. Petzold, “Description of dassl: a differential/algebraic system solver,” Sandia National Labs., Livermore, CA (USA), Tech. Rep., 1982.
- [72] Wikipedia contributors, “Computational fluid dynamics — Wikipedia, the free encyclopedia,” 2014. [Online]. Available: [https://en.wikipedia.org/wiki/Computational\\_fluid\\_dynamics](https://en.wikipedia.org/wiki/Computational_fluid_dynamics)
- [73] Resolved Analytics, “Comparing cfd software - part 4: Comprehensive cfd software packages,” 2020. [Online]. Available: <https://www.resolvedanalytics.com/theflux/comparing-cfd-software-part-4-comprehensive-cfd-software-packages>
- [74] Symscape, “Polyhedral, tetrahedral, and hexahedral mesh comparison,” 2013. [Online]. Available: <https://www.symscape.com/polyhedral-tetrahedral-hexahedral-mesh-comparison>
- [75] M. Sosnowski, J. Krzywanski, and R. Gnatowska, “Polyhedral meshing as an innovative approach to computational domain discretization of a cyclone in a fluidized bed cdc unit,” in *E3S Web of Conferences*, vol. 14. EDP Sciences, 2017, p. 01027.

- [76] M. Spiegel, T. Redel, Y. J. Zhang, T. Struffert, J. Hornegger, R. G. Grossman, A. Doerfler, and C. Karmonik, "Tetrahedral vs. polyhedral mesh size evaluation on flow velocity and wall shear stress for cerebral hemodynamic simulation," *Computer methods in biomechanics and biomedical engineering*, vol. 14, no. 01, pp. 9–22, 2011.
- [77] *ANSYS FLUENT User's Guide*, ANSYS Inc.
- [78] H. W. Starkweather Jr, "The effect of heating rate on the melting of polytetrafluoroethylene," *Journal of Polymer Science: Polymer Physics Edition*, vol. 23, no. 6, pp. 1177–1185, 1985.
- [79] F. Stern, R. V. Wilson, H. W. Coleman, and E. G. Paterson, "Verification and validation of cfd simulations," IOWA INST OF HYDRAULIC RESEARCH IOWA CITY, Tech. Rep., 1999.
- [80] P. Cui, B. Li, J. Tang, X. Gong, and M. Ma, "An improved tri-linear interpolation method for hybrid overset grids and its application," in *Asia-Pacific International Symposium on Aerospace Technology*. Springer, 2018, pp. 601–613.
- [81] P. J. Roache, *Verification and validation in computational science and engineering*. Hermosa Albuquerque, NM, 1998, vol. 895.
- [82] T. Xing and F. Stern, "Factors of safety for richardson extrapolation," *Journal of Fluids Engineering*, vol. 132, no. 6, 2010.